Advances in Membrane-Based Oil/Water Separation

by

Leonardo David Banchik

M.S., Mechanical Engineering
Massachusetts Institute of Technology, Cambridge, 2013
B.S., Mechanical Engineering
University of Nevada, Las Vegas, 2010
Submitted to the Department of Mechanical Engineering
in partial fulfillment of the requirements for the degree of

Doctor of Philosophy in Mechanical Engineering

at the

MASSACHUSETTS INSTITUTE OF TECHNOLOGY

February 2017

Signature redacted

Author . . . .
Department of Mechanical Engineering
October 20, 2016

Signature redacted

Certified by . . . .
John H. Lienhard V
Abdul Latif Jameel Professor, Department of Mechanical Engineering
Thesis Supervisor

Signature redacted

Accepted by . . . .
Rohan Abeyaratne
Chairman, Committee on Graduate Students
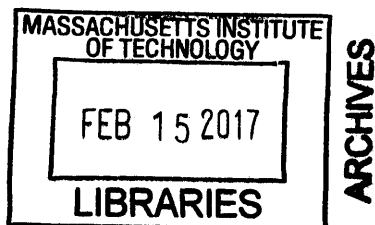
MITLibraries

DISCLAIMER NOTICE

Advances in Membrane-Based Oil/Water Separation
by
Leonardo David Banchik

Submitted to the Department of Mechanical Engineering
on October 20, 2016, in partial fulfillment of the
requirements for the degree of
Doctor of Philosophy in Mechanical Engineering

Abstract

Oil is a widespread pollutant from oil spills to industrial oily wastewater in the oil and gas, metalworking, textile and paper, food processing, cosmetics, and pharmaceutical industries. A wastewater of particular concern is produced water, an oily waste stream from hydrocarbon extraction activities. Worldwide, over 2.4 billion US gallons of produced water is generated every day. Membrane technologies have emerged as the preferred method for treating these wastewaters; this has allowed operators to reclaim and reuse fresh water for potable, industrial, and agricultural use and to meet waste discharge regulations. Yet, despite their technological predominance, membranes can become severely fouled and irreversibly damaged when bulk and small stabilized oil droplets, emulsions, are present in intake streams. In this thesis, we seek to mitigate these deleterious effects through several means.

First we seek to better understand fouling by oil-in-water emulsions on conventional polymeric ultrafiltration membranes. We investigate the decrease in water production over time using model and actual produced water samples with varying solution zeta potentials and make meaningful recommendations to operators based on our observations. Next, we develop a robust multifunctional membrane which can in one step degrade organic pollutants and separate bulk and surfactant-stabilized oil/water mixtures while achieving high fluxes, high oil rejection, and high degradation efficiencies.

Finally, we investigate the potential of novel in-air hydrophilic/oleophobic microfiltration and reverse osmosis membranes for their anti-oil fouling performance relative to conventional hydrophilic/oleophilic membranes. Contrary to claims in literature of superior performance, we find that in-air oleophobicity does not aid in underwater anti-fouling due to surface reconstruction of mobile perfluoroalkyl chains in the presence of water. Based on these observations, we discuss opportunities for future research on oil anti-fouling membranes using fluorinated moieties.

Thesis Supervisor: John H. Lienhard V
Title: Abdul Latif Jameel Professor, Department of Mechanical Engineering

Acknowledgments

This Institute has a slogan, *Mens et Manus*, Latin for Mind and Hand, which I tried to pursue in earnest during my academic journey. Because my Master's work had been mostly computational, *Mens*-style work, I decided to pursue work more associated with the *Manus* side of science for my doctorate. This work would involve much more hands-on experimentation and would hopefully yield readily applicable results. During my time at MIT, I have been fortunate to experience both styles of work, but I have *many* people to thank for supporting me through the steep learning curve associated with the transition from one work style to the other.

I wish to first thank my adviser, Prof. John H. Lienhard V, for his support in letting me pursue the topics which interested me most – regardless of the slope of the learning curve. Additionally, it has been a pleasure to learn from Prof. Lienhard about asking the right research questions and communicating clearly through academic publications and presentations. I would also like to thank Prof. Lienhard for his guidance and financial support of the MIT Water Club, a club whose future I was fortunate enough to help shape during my 2013 Co-Presidency. Prof. Lienhard has been a strong ally of the club and has a genuine desire to support clubs on campus which operate at the intersection of the Energy-Water-Food nexus.

Along with Prof. Lienhard, I am very thankful for the other members of my doctoral committee: Prof. Alan T. Hatton, for his guidance associated with his deep knowledge of colloidal systems, and Prof. Gareth H. McKinley, for his critical eye which has considerably improved the work herein.

This work would not have been possible without funding from my sponsors, the King Fahd University of Petroleum and Minerals and the National Science Foundation Graduate Research Fellowship, and I am sincerely grateful for their financial support.

Early during this *Manus*-styled journey, I remember realizing that the resources necessary to perform much of the work in this thesis were scattered around the Institute in the form of specialized laboratory equipment and very knowledgeable researchers. I am deeply grateful for these researchers, many of whom would become future friends, for teaching me how to use the lab equipment and spending hours of their time to help guide me through new research territories. In particular I'd like to thank Gibum Kwon, Divya Panchanathan, and Talal Qahtan. Gibum was a great ally in the lab, helping me to spray coat my first hydrophilic-oleophobic membranes based on formulations in the literature which served as an important basis for the work in Ch. 3. Divya has been a close partner while working on Chs. 3-5; in addition to helping me perform some of the experiments, it's been fantastic to strategize future research steps with her. Talal Qahtan was a wonderful partner to work with on Ch. 3; he delivers quality experimental results, works hard to deliver results in a timely fashion, and has demonstrated creativity in his work.

I'd also like to thank Priya Moni, Minghui Wang, Rong Yang, and Hossein Sojoudi in Prof. Karen Gleason's lab; Seyed Mahmoudi, Arindam Das, Paris Cox, Srinivas Subramanyam, and Brian Solomon in Prof. Kripa Varnasi's lab; Andrew Jones and Youngsoo Joong in Prof. Cullen Buie's lab; Simon Choong and Yi-Min Lin in Prof. Gregory Rutledge's lab; and Dayong Chen in Prof. Robert Cohen's lab. Special thanks also to Leslie Regan, Joan Kravit, and Una Sheehan in the MechE Department for always being available to chat about graduate school challenges and next steps.

I sincerely hope that every future team of which I am a part is as colorful, dynamic, helpful, and sincere as the Lienhard Lab. In no particular order, thanks are due to: Emily Tow, my fellow foul pal (our theses involved membrane fouling), for helpful discussions on experiments and invaluable critical feedback; David Warsinger for great feedback; Kishor Nayar for spiritual guidance & entrepreneurial chats; Hyung Won Chung for discussions and collaboration on pressure retarded osmosis; Jaichu Swaminathan for helpful discussions; Gregory Thiel and Adam Weiner for useful discussions and fruitful collaborations; Ronan McGovern for good feedback on a few works; Karim Chehayeb, Karan Mistry, Ed Summers, Urmi Roy, Omar Labban, Yvana Ahdab, and Quantum Wei for making life in the lab a lot more fun. Thanks are also due to my two UROPs, Joshua Emig and Hind Saleh who did some of the great work in Chs. 2 and 4, respectively. Christine Gervais was instrumental in ordering parts for my experiment and helping with many other administrative tasks, and Theresa Werth and Kate Anderson were reliable and fun to work with as well.

I was also very fortunate to work on another phenomenal team: the MIT Water Club. Working

with the club has taught me invaluable lessons on leadership, taking risks, and working with others to shape grand visions into realities. I believe that through our work on the MIT Water Summit, the Water Innovation Prize, the Water Night, the Lecture Series, and the Lunch-and-Learns, we have educated and galvanized the water community within MIT and even in the greater Boston area. I am proud of our work and I am grateful for our time together. Working on the leadership board of the Graduate Association of Mechanical Engineers (GAME) for a year with Lee 'Dubs' Weinstein prepared me for my time at the Water Club and I am grateful to both Lee and MIT GAME for those positive experiences.

I have listed the next three groups last as they have served as a strong foundation throughout my time at this Institute. They've consoled me as I've vented about research obstacles (membranes not working!) and celebrated with me during the successes.

Community. Since our first boat ride on the Boston Harbor, to the many shindigs at Tang, 89 Plymouth, and 9 Smith, you folks have been with me through the trenches of quals, PSETs, and research rollercoasters. In no particular order, there's Charlie 'Chuckles' and his boats, boatshoes, bots, and bass chops; Alice and Rob and their DIY skills, brie bakes, and '80s parties/movies with plenty of TayTay on the side; Izzy and Leah and their empanadas/alfajores, Jewish holidays celebrating trees, and New Mexico Chile madness; the oily-man himself Anton and his inspirational and limit destroying worldwide adventures; Thomas 'the Tank Engine' and his extraordinary Poly Sci skills; Lindy and her wry humor and fab movie recs; Geoff and his slick design chops and great laugh; Aditya and Steve for their brilliant wordplay, love for H.P. Lovecraft, and music recs; Francisco and Ana Maria for allowing me to feel more Latino with occasional excursions to Casa Portugal; Mike and Molly for the delicious home brews, ribs, and cocktails you provide in addition to the warmth your company provides; David and Jess for always making me feel welcome to your home full of food, music, and philosophical musings; Tim, Erin, Frankie, and the Field of Dreams; RoRoMcGo, GPT, and AMW for Border Nights, playing a bunch of wrong notes jazz shtyle, crazy accents, shports, and having the craic. My friends at home have also lent their hands in many ways: Max Kutner, Jared Ardine, John Menist, Micah van Lelyveld, and Jon Realmuto. I must also thank the MIT Festival Jazz Ensemble, The Root House Band, Macademia, and Scubaphone (Krista Speroni and Otto Briner in particular) for letting me funk out and experience restorative musical flow on some strings.

Family. Mom, Dad, Anna, and Marcos. The most solid nuclear family one could ever ask for - you are a bedrock of love and positivity in my life. I also have the extended Banchiks and Gonorazkys to thank - Noam Segal and Jason Wood make this list. Thanks to Jason also for helpful discussions on chemistry.

Fiancée. Shu Dar Yao - I love you! What a whirlwind of a time we've had since our fateful meeting at Tommy Doyles so long ago, no? From jumping the tall bridges in Wien and wandering around the rainy streets of Prague, to exploring the ancient ghats of Varanasi and blue sun-drenched villas of Chefchaouen - may we continue to travel and fall more in love with eachother. Thank you for being a rad, go-getting, feedback factory from the start. Here's to many more joyous years of adventure and prosperity together, improving ourselves and striving to lift our communities.

Contents

List of Figures

11

List of Tables

13

Nomenclature

Roman symbols		Units
A_s	wetted surface area of membrane	m^2
A_m	membrane area	m^2
AAPD	average absolute percentage deviation	%
C	concentration	mol/L, mg/L, or mg/mL
d	droplet diameter	μm
D	fiber diameter	μm
D_h	hydraulic diameter	m
h	pore height	μm
I	UV light irradiance	mW/cm^2
J or J_w	permeate flux	L/m^2-hr or m/s
k_{ads}	adsorption constant for organic pollutant	L/mg
k_{app}	applied rate constant	s^{-1}
k_p	photocatalytic rate constant	mg/L-s
M	molecular weight	g/mol
P	hydraulic pressure	kPa or bar
t	time	s
V_r	reactor volume	m^3
w	pore width	μm
X	collapsed variable for analytical degradation model	mW$^{1/2}$-s/cm

Greek symbols		Units
α	degradation efficiency	%
β	figure of merit for flow through photocatalytic system	cm/mW$^{1/2}$-s
γ	surface tension or surface energy	mN/m or mJ/m^2
ε	model error	%
Θ	dimensionless scaled flux	
Π	osmotic pressure	bar
ρ	density	kg/L
σ	standard deviation	

Subscripts

0	initial state or cake filtration
1	partial blocking
1.5	internal blocking
2	complete blocking
A	advancing
a	air
ad	adhesion
h	hydrophilic
o	oil
R	receding
s	substrate
t	function of time
w	water

Superscripts

*	steady state or apparent contact angle

Abbreviations

CA	contact angle
HB	hydrophobic
HL	hydrophilic
MF	microfiltration
OB	oleophobic
OL	oleophilic
PFA	perfluoroalkyl
RO	reverse osmosis
SHL	superhydrophilic
SOB	superoleophobic
SSF	SiO_2/SF-100/FS-50
SSFT	SiO_2/SF-100/FS-50/TiO_2
UF	ultrafiltration
UV	ultraviolet

Chapter 1

Introduction

The separation of oil from water is a crucial wastewater treatment step in many industries including oil and gas, metalworking, textile and paper, food processing streams, cosmetics, and pharmaceuticals [2]. Oil/water separation is also required for treating oil spills which can cause significant environmental damage if not treated effectively and quickly [3]. An oily wastewater of emerging concern is produced water, a waste stream from hydraulic fracturing processes.

1.1   Produced water

Oil and gas companies produce between seven and fifty barrels of produced water for every barrel of oil. This amounts to upwards of 2.4 billion US gallons of wastewater produced per day worldwide which much be treated or properly disposed [4]. Among the many contaminants in produced water [5], these wastewaters contain small, hard-to-separate (emulsified) oil droplets which must be removed by well operators when recycling or disposing of these waters. To do so, companies usually rely on chemical coagulation, a costly and often ineffective method of emulsion removal that requires expensive and hazardous chemicals which produce a useless sludge. The sludge must be disposed, typically by trucking to an off-site dumping reservoir or an open pit where natural water resources can become contaminated [4]. Due to the high cost of water treatment, wastewater is often injected into disposal wells rather than treated, resulting in contamination, high water consumption, and even seismic activity [6, 7]. As such, the industry has come under increasing political and economic pressure to more efficiently manage the billions of gallons of produced water from their oil and gas extraction activities.

1.2   Oil/water separation technologies

There are many technologies available for treatment of oily wastewaters. The concentration and size of dispersed oil in these waters typically dictates which treatment technology is used. Oil/water mixtures can be classified into three categories based on oil droplet diameter d: free mixtures $d > 150$ μm, dispersions $20 < d < 150$ μm, and emulsions $d < 20$ μm [2]. Emulsions can be either oil-in-water (oil as the dispersed phase, water as the continuous phase) or water-in-oil (water as the dispersed phase, oil as the continuous phase) depending on surfactant type, volumes of both phases, temperature, pH, and other factors [8, 9]. In

this thesis, we focus on water-in-oil emulsions due to their prevalence in produced water and other industrial oily wastewaters [2, 5, 10, 11].

Gravity-based separation technologies, such as lamella clarifiers, are often used as primary treatment for oily wastewaters because they are effective for free and dispersed oil/water mixtures. This is because droplets with a diameter of $\gtrsim$ 25 μm have faster settling velocities, as predicted by Stokes' law, than droplets $\lesssim$ 10 μm [12]. The retentate streams from these treatment systems, therefore, typically contain oil in an emulsified form. Emulsified oil can be stabilized by surfactants, polymers, asphaltenes, or other solids which accumulate at the oil-water interface [8, 13].

Several technologies exist for treatment of the remaining emulsified oil. These technologies include chemical coagulation, dissolved air filtration, hydrocyclones, media filtration, and polymeric or ceramic membranes. Operators must balance four criteria when choosing a technology to use: power requirements, footprint and weight, oil and particulate rejection, and cost.

1.2.1 Chemical coagulation

Chemical coagulation is the addition of highly charged metal cations and polymers to reduce the repulsive double layer which surrounds each droplet, reducing the electrostatic repulsive energy barrier consequently reducing coalescence times. This process, however, is highly susceptible to variable influent quality, requires time consuming jar testing for careful chemical selection, is ineffective for small droplets, has a large footprint, and produces large volumes of sludge [2]. Although more responsive to variable influent quality and operable at smaller system footprints, electrocoagulation/flocculation, like chemical coagulation, is ineffective for small droplets and also creates large volumes of sludge [4, 14].

1.2.2 Dissolved air flotation

Dissolved air flotation (DAF) uses gas bubbles to remove suspended particles that are difficult to separate through sedimentation. DAF suffers from high system complexity as well as high operation and maintenance costs [4, 5]. DAF systems are also ineffective at removing particles and oil droplets smaller than 10 μm [5].

1.2.3 Hydrocyclones

Hydrocyclones separate solids and oils from water based on density differences between phases. They are robust, mobile, and are operable with small system footprints relative to chemical coagulation and DAF, but suffer from high capital and energy costs [4, 5]. Furthermore, hydrocyclones are ineffective at removing particles and oil droplets smaller than 10 μm [5].

1.2.4 Media filtration

Media filtration uses various types of media such as walnut shell, gravel, or anthracite to separate particles by adsorption and steric exclusion. While media filtration is an efficient way to remove free and dispersed oil and grease, it is ineffective at removal of sub-micron oil droplets and particulates and suffers from high maintenance costs [5].

1.2.5 Membrane filtration

Polymeric/ceramic microfiltration (MF) and ultrafiltration (UF) are applicable to challenging wastewaters and are able to consistently separate small emulsified oil droplets in addition to other suspended solids. Relative to other technologies, they use less energy and are highly modular and mobile [4]. As a result of these advantages, MF and UF treatment systems have emerged as the preferred method for oily wastewater treatment and desalination pretreatment [2, 5, 10, 11, 15].

1.3 Membrane technologies

In addition to separation of emulsified oil from water, many produced water streams also require desalination for reclamation or reuse. For these very salty feedwaters, thermal technologies are frequently used although reverse osmosis (RO) membrane technologies are predicted to energetically outperform them [16] and may eventually be used for these highly saline feed waters as well. To summarize, membrane technologies are supplanting other established technologies not only for oil/water separation but for salt separation (desalination) as well.

One of the main impediments to using RO for the desalination of oily wastewaters is that RO membranes have an extremely low tolerance for oil in the feed stream [17]. Organic fouling by oil and grease can cause irreversible and severe decreases in permeability along with possible degradation of the membrane. Organic emulsions, in particular, can form a film on the membrane surface and must be removed in pretreatment. For their RO membranes, DOW recommends an extraordinarily low maximum contaminant level of 0.1 mg/L of oil in the feed stream [18]. DOW reports that oil fouling is especially difficult to remove from a membrane surface once it has occurred.

In addition to RO, MF and UF membranes are also severely affected by free, dispersed, and emulsified oil fouling [2, 19–22]. Because membrane systems are so effective at treatment and desalination, however, improving their fouling resistance to organic foulants such as oil has been an area of great academic focus. For decades, researchers have made efforts to develop anti-fouling membranes by increasing the hydrophilicity of membrane surfaces [23–25]. While these investigations have yielded significant gains in membrane resistance to fouling, researchers continue to find new ways to push the limits of anti-fouling performance.

Recently, exciting new surfaces which are simultaneously hydrophilic and oleophobic in-air have been reported in the literature [26–31]. The properties which endow these surfaces with their unique in-air wettability have been applied to porous materials and membranes for free and emulsified oil/water separation with reported high rejection and anti-fouling performance [26, 27, 29, 30, 32–34].

For instance, Kota et al. used a hybrid coating comprised of hydrophilic and hydrophobic/oleophobic (omniphobic) fluorocarbon moieties to create a membrane which allows for water passage during filtration of oil-in-water and water-in-oil emulsions and even bulk oil-water mixtures [26]. This filter, which was hydrophilic and oleophobic in an air environment, demonstrated high oil rejection and high fluxes with little fouling in steady state. Another research group added an omniphobic fluorocarbon moiety during the production of a polymeric membrane to create a filter which was also hydrophilic and oleophobic in an air environment. Dead-end and crossflow experiments were used to show that the novel membranes which contained the fluorocarbon compounds fouled less during oil-water emulsion filtration than benchmark membranes without the compound [31]. These are exciting

developments which are investigated in the latter chapters of this thesis.

1.4 Thesis aims

In this thesis, we contribute to the field of oil/water separation through several studies:

In Ch. 2, we seek to better understand fouling by oil-in-water emulsions on conventional polymeric ultrafiltration membranes. We investigate the decrease in water production over time using model and actual produced water samples with varying solution zeta potentials and make meaningful recommendations to operators based on our observations.

In Ch. 3, we develop a robust multifunctional membrane which can in one step degrade organic pollutants and separate bulk and surfactant-stabilized oil/water mixtures with high fluxes, oil rejection, and degradation efficiencies.

Finally in Ch. 4 and Ch. 5, we investigate the potential of novel in-air hydrophilic and oleophobic MF and RO membranes for their anti-oil fouling performance relative to conventional hydrophilic and oleophilic membranes. Contrary to claims in literature of superior filtration performance, we find that in-air oleophobicity does not aid in underwater anti-fouling due to surface reconstruction of mobile perfluoroalkyl chains in the presence of water. Based on these observations, we discuss opportunities for future research on oil anti-fouling membranes using fluorinated moieties.

Overall, this thesis contributes to the field of oil/water separation by better understanding fouling mechanisms on conventional membranes, by making advances in filtration and purification technology via novel multifunctional membranes, and by investigating the potential of membranes with unique in-air wettability for enhanced underwater oil filtration.

Chapter 2

Effect of oil-in-water emulsion surfactant charge on ultrafiltration membrane fouling in dead-end and crossflow filtration

Chapter abstract

In this chapter, we assess the role that surfactant head charge plays during surfactant-stabilized oil-in-water emulsion fouling of polymer ultrafiltration membranes. The extent of fouling was determined by steady state flux in constant pressure dead-end batch and crossflow filtration. Emulsions are prepared with anionic (SDS), nonionic (Tween 80), and cationic (CTAB) surfactants which have droplet size distributions and concentrations representative of oily wastewater obtained from hydraulic fracturing operations. In dead-end batch filtration, cationic and anionic emulsions result in similar fouling while nonionic emulsions are observed to destabilize easily. In crossflow filtration, cationic emulsions are observed to result in the lowest steady state flux followed by nonionic and finally anionic emulsions. These results suggest that droplet-droplet electrostatic repulsion dominates fouling in dead-end batch filtration while droplet-membrane electrostatic interactions are more relevant in crossflow operations. We also filter two produced water samples with nearly neutral zeta potentials in dead-end batch mode and observe that fouling was most similar to anionic and cationic (not nonionic) emulsions, implying that oily wastewaters in the produced water space may be stabilized by steric rather than electrostatic repulsion. Applying fouling blocking models, we may infer that nonionic emulsions form cakes while anionic and cationic surfactants completely and partially block membrane pores indicative of a thin coating of oil on the membrane surface. On the basis of steady state flux results, we recommend that anionic surfactants be used to stabilize emulsions treated by crossflow filtration and nonionic surfactants be used to stabilize emulsions treated by dead-end batch filtration.

2.1 Introduction

Oil-water separation is a crucial step in the remediation of wastewater from many industries including oil & gas, metalworking, textile and paper, cosmetics, and food [2]. Oil-in-water mixtures can be classified into three categories based on oil droplet diameter d: free mixtures $d > 150$ μm, dispersions $20 < d < 150$ μm, and emulsions $d < 20$ μm. Efficient separators for emulsions, in particular, are of interest because conventional technologies such as gravity-based separation, heating/cooling, and chemical coagulation are more effective for free mixtures and dispersions and are too complex, costly, or simply unable to effectively treat emulsions [2, 5]. Streams containing oil-water emulsions must also be nearly oil free if they are to be desalinated using a membrane-based process. The DOW Chemical Company, for instance, recommends less than 0.1 part per million of oil and grease for their FILMTEC line of reverse osmosis membranes [18]. For emulsion treatment, ultrafiltration (UF) and microfiltration (MF) are finding increasingly widespread use due to their low cost and energy efficiency [10, 35].

While membrane systems are considered to be the benchmark in emulsion treatment, an outstanding issue is the deleterious effect of oil fouling on the membranes over time. During constant pressure filtration, fouling causes a decline in flux over time resulting in reduced permeate production. This leads to system oversizing to compensate for the permeate lost by fouling. During constant flux filtration, fouling causes an increase in applied trans-membrane pressure over time resulting in increased energy costs. The rise in pressure leads to increased energy consumption. In both constant pressure and flux filtration, mechanical cleaning, backwashing, or chemically enhanced cleaning methods are used to restore membrane permeability. The extent of permeability restoration also declines over time due to irreversible fouling [36, 37]. In sum, fouling is important to understand and minimize as it increases plant capital and operating expenditures.

An oily wastewater of emerging concern is the effluent from hydraulic fracturing operations known as produced water [5]. Produced waters can contain up to 1500 mg/L of total organic carbon and up to 60 mg/L of oil/grease [5], much of which is in an emulsified form. We use these wastewaters as the model foulant in this chapter.

Emulsions are kept stable for long periods of time by an emulsifier or surfactant. These agents keep oil droplets from coalescing by electrostatic or steric repulsion and by reducing the liquid-liquid interfacial surface tension. These agents are sometimes added intentionally to aid in hydrocarbon extraction but may also enter the feeds naturally during the extraction process. Typical emulsifiers found in produced water include paraffins, metallic salts, organic acids, resins, colloidal silts and clay, asphaltenes, and polymers [13]. These emulsifiers are able to stabilize oil droplets by predominantly steric rather than electrostatic repulsion. Other types of stabilizers are surfactants, which can be categorized according to the charge of their hydrophilic head: anionic (-), cationic (+), nonionic (0), and amphoteric (±) [8]. The nature of membrane fouling by anionic, nonionic, and cationic surfactants has been investigated in the literature and the shape and charge of the surfactant head play an important role in fouling [38, 39].

MF and UF fouling by oil-water emulsions is a complex process affected by oil and surfactant concentration, oil droplet size, emulsion stability, and operating conditions [19, 20, 40–44]. Although explored to a lesser extent, surfactant and membrane zeta potentials also play a significant role during fouling and irreversible permeability loss. In an aqueous environment of neutral pH, polymer and ceramic membranes have a negative zeta potential (a proxy for surface potential) while surfactant potentials are primarily determined by the valence of the head charge. During filtration, surfactant and membrane potentials result in droplet-droplet and droplet-membrane electrostatic interactions which we find to be of crucial importance in fouling severity. Lu et al. [43] found that diesel and crude-oil emulsions stabilized by a nonionic surfactant (polyoxyethylenesorbitan monooleate, Tween 80) resulted in the least irreversible fouling for cycles of dead-end batch filtration and water rinsing using ceramic ultrafiltration membranes. The extent of irreversible fouling increased for the cationic (cetyltrimethylammonium bromide, CTAB) surfactant and was greatest for the anionic surfactant (sodium dodecyl benzenesulfonate, SDBS).

In this chapter we determined the effect of surfactant charge on the fouling severity in the filtration of oil-water emulsions using a polymer (polyacrylonitrile) ultrafiltration membrane in both dead-end batch and crossflow filtration modes. We studied two filtration modes to compare fouling in the different applications where each mode is used. There are

two main differences between both modes of filtration. Firstly, in dead-end batch, feedwater flows perpendicular to the membrane surface while it flows parallel to the membrane surface in crossflow. More importantly, the emulsion concentration rises in the cell over time in dead-end batch filtration while it stays relatively constant in crossflow filtration. While dead-end batch filtration tests are easier to perform in the laboratory and, thus, are often used by researchers to characterize membrane performance or assess the fouling potential of certain feedwaters, these tests are also representative of dead-end hollow fiber filtration, which are often used to achieve high permeate recoveries during treatment [22]. Therefore, our results for dead-end batch tests may be relevant to these hollow fiber systems. Crossflow filtration systems are also widely used and experience less fouling compared to dead-end systems [36].

We characterized six samples of produced water, our model foulant, to assess oil concentration, suspended droplet size distribution, pH, and zeta potential. We prepared three model oil-in-water emulsions using anionic (sodium dodecyl sulfate, SDS), nonionic (Tween 80), and cationic (CTAB) surfactants which were representative of produced water samples based on oil concentration and volume-based droplet size distribution. We investigated the extent of flux decline in constant pressure dead-end batch and crossflow filtration using these model emulsions. We found that the extent of fouling differs greatly as a function of surfactant charge and filtration mode (dead-end batch vs. crossflow). We also filtered two produced water samples in dead-end batch mode and results are compared to model emulsions. To infer which fouling mechanisms may have prevailed during fouling, we applied classic blocking filtration laws considering both fouling deposition and removal to the flux decline curves.

2.2   Blocking law theory for constant pressure filtration

Fouling refers to the decrease in water production due to the increase of hydraulic resistance in membrane systems over time. It is a complex, kinetic process determined by the rates of particle deposition and removal from the membrane surface and pores. Regarding particle deposition, four mechanisms exist for fouling of porous membranes by suspended solids

during filtration: complete pore blocking, internal pore blocking, partial pore blocking, and cake filtration. These physical mechanisms were first described by Hermans and Bredée [45] and compiled and expanded by Hermia for dead-end flow applications [46]. The models can be expressed in terms of permeate flux J as a function of time t, a proportionality constant K_n, and an exponent n which denotes the mode of fouling:

$$-\frac{dJ}{dt} = K_n J^{3-n} \tag{2.1}$$

The constant K_n is often found by curve fitting and the fouling modes are given by $n = 2$ for complete pore blocking, $n = 1.5$ for internal pore blocking, $n = 1$ for partial pore blocking, and $n = 0$ for cake filtration. Complete pore blocking occurs when large particles in solution block the entirety of a pore mouth preventing permeate from flowing through the pore. Internal pore blocking refers to the decrease of the effective radius of membrane pores as smaller particles enter the mouths and adsorb onto pore walls. Partial pore blocking occurs when a single or multiple particles partially cover each pore. Cake filtration occurs when a porous layer, or cake, of particles forms and increases in thickness on the membrane surface acting as an in-series hydraulic resistance.

While useful and widely used, the models given by Eq. 2.1 only consider the deposition portion of the fouling process. Without a removal term, the final flux during filtration would mathematically be zero for long times ($t \rightarrow \infty$) as foulant continues to deposit onto the membrane surface. In order to study these models, many researchers use pressurized dead-end flow filtration cells without stirring in an effort to minimize particle removal.

To infer which fouling mechanism may have been most prevalent during flux decline experiments, we use equations developed by Field et al. [40, 47]. These equations include a final flux term that effectively allows for the consideration of foulant removal during filtration. There are two sets of equations, the time-flux and time-flux-volume, which we summarize in Table 2.1. To use the equations, we assume that the particles contributing to flux decline do not coalesce (where two or more suspended oil drops join to form a single droplet) at the membrane surface or within a cake and that their removal rate is constant with respect to time. We assume that foulant removal from the membrane surface occurs

Table 2.1: Time-flux and time-flux-volume set of equations for fouling mechanism analysis where J^* is steady state flux, $\Theta = \frac{J-J^*}{J_0-J^*}$, and $J = J(t)$.

Fouling mechanism	n	Time-flux set		Time-flux-volume set		Description	
Complete blocking	2	$\ln|\Theta| = K_2 t$	(2.3)	$J_0 - J = K_2(v - J^*t)$	(2.4)	Particles reaching the membrane entirely seal a pore.	
Internal blocking	1.5	$J^{-0.5} - J_0^{-0.5} = K_{1.5}t$	(2.5)	$J^{0.5} - J_0^{0.5} = K_{1.5}(v - J^*t)$	(2.6)	Pore volume decreases proportionally to permeate volume. Pores are constant diameter and length.	
Partial blocking	1	$\frac{1}{J^*}\ln\left|\frac{J}{J_0 \cdot \Theta}\right| = K_1 t$	(2.7)	$\ln\left|\frac{J_0}{J}\right| = K_1(v - J^*t)$	(2.8)	Incremental blocked surface area is proportional to unblocked surface area.	
Cake filtration	0	$\frac{1}{J^{*2}}\left[\ln\left|\frac{J \cdot \Theta}{J_0}\right| - J^*\left(\frac{1}{J} - \frac{1}{J_0}\right)\right] = K_0 t$	(2.9)	$\frac{1}{J} - \frac{1}{J_0} = K_0(v - J^*t)$	(2.10)	Flux decreases with an in-series hydraulic resistance proportional to permeate mass.	

either through emulsion flocculation and creaming [8] and/or by inertial lift (in crossflow filtration). Note that the complete, partial, and cake blocking laws allow for individual particle deformation [46].

We use both sets of equations in Table 2.1 as follows: the time t, specific permeate volume v, flux J, initial flux J_0, and steady state flux J^* from each fouling test are used with the time-flux-volume set of equations (Eqs. 2.4, 2.6, 2.8, 2.10 from Table 2.1) to find K_n and the coefficient of determination R^2 through a linear fit. We then use each obtained blocking coefficient K_n to model the flux decline as a function of t, J_0, and J^* using the time-flux set of equations (Eqs. 2.3, 2.5, 2.7, 2.9 from Table 2.1). Because many of the R^2 values are near unity, we use the average absolute percentage deviation between flux data and predicted flux from each model to determine goodness of fit and assess which mechanism may have predominated during fouling. Average absolute percentage deviation, AAPD, is determined by:

$$\text{AAPD} = \frac{1}{m}\sum_{i=1}^{m}\left(1 - \frac{J_{i,model}}{J_{i,data}}\right)100 \tag{2.2}$$

where m is the number of data points in the time series and i refers to the ith element in the series.

We use the time-flux-volume set of equations for linear regression analysis because we found that use of these equations rather than the time-flux set significantly reduced noise in the later stages of filtration as J approached J^* during curve fitting. The reduction of noise allowed for more accurate curve fitting, providing K_n values which were used to calculate AAPD.

26

2.3 Experimental procedures

2.3.1 Preparation of oil-in-water emulsions
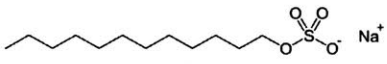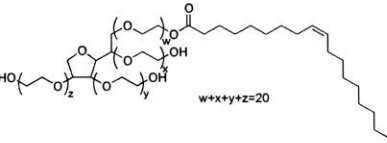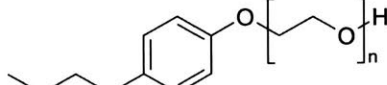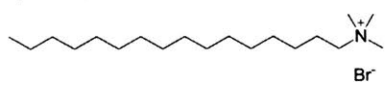
Three oil-in-water emulsions were prepared for each fouling test using three separate surfactants (Sigma Aldrich): sodium dodecyl sulfate (SDS, anionic), cetyl trimethylammonium bromide (CTAB, cationic), and polyoxyethylenesorbitan monooleate (Tween 80, nonionic). Triton X-100 (Sigma Aldrich) was also used for a series of dead-end batch tests. Hexadecane (99.9%, Sigma Aldrich) ($\gamma_{LV} = 27.5$ mN/m) was used as the model oil due its low surface tension, consistent chemical composition, and use in other studies [44].

Each surfactant stabilized oil-in-water emulsion was prepared using a 10:1 oil to surfactant ratio by weight with DI water to give 625 mg of oil and surfactant per liter of solution. For dead-end batch tests, 0.227 g of hexadecane and 0.023 g of surfactant was added to 400 mL of deionized water (DI) and sheared in a blender (Waring) for 5 minutes. After the gas-liquid foam resulting from the blending destabilized over roughly 30 minutes, 300 mL of this mixture was added to the dead-end cell. For crossflow tests, 7.737 g of hexadecane (99.9%, Sigma Aldrich) and 0.774 g of surfactant were added to 400 mL of deionized water and sheared in a blender for 5 minutes. Of this mixture, 300 mL was added to the system feed tank after the gas-liquid foam resulting from the blending destabilized over roughly 30 minutes. All prepared emulsions were visibly stable for at least a 20 hour period.

Table 2.2 gives for each surfactant its charge, molecular weight M, critical micelle concentration (CMC), hydrophilic lipophilic balance (HLB), the molecular weight of the hydrophilic portion of the surfactant M_h, and surfactant chemical structure. We calculate $M_h = 0.05 \cdot M \cdot HLB$ assuming Griffin's method [9].

Surfactant concentrations in this study were 57.5 mg/L, meaning that SDS and CTAB concentrations are below their CMC while Tween 80 was above the CMC by a factor of 4.4. In general nonionic surfactants have a much lower CMC than ionic surfactants, making it challenging to prepare a concentrated nonionic surfactant-stabilized oil-in-water emulsion with surfactant concentrations below the CMC. We therefore include an additional nonionic surfactant, Triton X-100, for dead-end batch tests to compare performance against Tween 80.

Table 2.2: Surfactant properties obtained from DOW, and Sigma-Aldrich product literature and Needs [1].

Surfactant	Charge	M (Da)	CMC (mg/L)	HLB	M_h (Da)	Structure
SDS	Anionic	288.4	2010.8 to 2884.0	40.0	576.8	
Tween 80	Nonionic	1310.0	13.0 to 15.0	15.0	982.5	
Triton X-100	Nonionic	625.0	189.0	13.4	418.8	
CTAB	Cationic	364.5	335.3 to 364.5	10.0	182.3	

2.3.2 Produced water and model emulsion characterization

Six produced water samples were obtained from Gradiant Corp. from different hydraulic fracturing sites across the United States. All samples were collected at the outlet of a preliminary gravity-based oil/water separator used to separate free and dispersed oil. The samples were characterized as received.

Droplet size distributions in the prepared model emulsions and produced wastewater samples are shown in Fig. 2-1. They were measured using a dynamic light scattering device (ZetaSizer, Malvern) using the refractive index of hexadecane (RI = 1.434). Log-normal Gaussian curves were fit to the measured data points using Excel Data Solver and the mean and standard deviation for each peak is given. For the Bakersfield and Barnett samples, the three peaks with the greatest amplitude are reported.

Zeta potential of the model emulsions and wastewater samples were calculated from the electrophoretic mobility measured using a zeta potential analyzer (ZetaPALS, Brookhaven Instruments Corporation) and averaged over 3 runs, applying between 2.5 and 5 volts and 2 to 5 hZ for 50 cycles each run. Produced water samples were diluted with DI water until sample conductivity was below 30 mS/cm before zeta potential measurement.

Conductivity for each sample is measured using a conductivity meter (HQ440d, Hach) and pH is measured using a pH meter (sympHony, VWR).

(a) Produced water (b) Model produced water
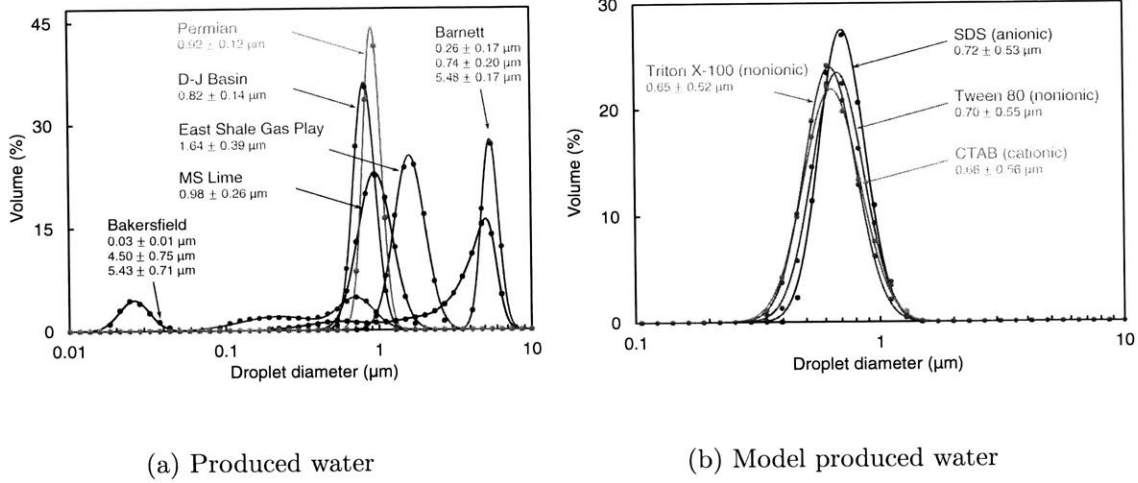
Figure 2-1: Volume-based droplet size distributions for: (a) produced water samples and (b) model produced water. Dots are measured data points and lines are log-normal Gaussian curve fits through the data. Mean and standard deviation for peaks are given.

Zeta potential, pH, conductivity are tabulated for the produced water samples and model oil-in-water emulsions in Table 2.3. Total organic carbon (TOC) measurements were performed for produced water samples using a total organic carbon (TOC) analyzer (TOC-L Series, Shimadzu). Referring to Fig. 2-1, Table 2.3, and the protocol for model emulsion preparation, we show that the droplet size distribution, concentration, and pH for the model emulsions are representative of the produced water samples.

Table 2.3: Produced water and model oil-water emulsion characterization. pH values have a $\pm$ 0.01 accuracy and TOC measurements have a $\pm$ 1.5% accuracy.

Sample	Zeta potential (mV)	TOC (mg/L)	pH	Conductivity (mS/cm)
Produced water samples				
Bakersfield	-2.17 $\pm$ 1.93	65.1	6.71	11.3
Permian	-2.69 $\pm$ 0.60	271.3	6.48	126.3
D-J Basin	-4.11 $\pm$ 2.22	625.0	7.08	38.9
East Shale Gas Play	-3.87 $\pm$ 2.96	256.8	5.26	184.5
MS Lime	-1.81 $\pm$ 0.72	15.2	7.57	28.9
Barnett	-2.42 $\pm$ 1.08	198.3	8.03	35.1
Average	-2.84 $\pm$ 1.75	238.62 $\pm$ 215.56	6.86 $\pm$ 0.96	70.83 $\pm$ 68.70
Model oil-water emulsions				
SDS/Hexadecane	-41.67 $\pm$ 4.75	-	6.77	36.0×10^{-3}
Tween 80/Hexadecane	-10.60 $\pm$ 0.96	-	6.62	6.5×10^{-3}
Triton X-100/Hexadecane	-23.46 $\pm$ 4.48	-	6.82	13.4×10^{-3}
CTAB/Hexadecane	33.72 $\pm$ 6.88	-	6.42	21.5×10^{-3}

2.3.3 Membrane characterization

Polyacrylonitrile (PAN) membranes (PAN50, Nanostone) were used due to their hydrophilicity relative to other polymers such as polyethersulfone, polysulfone, polyvinylidene fluoride, polyethylene, and polypropylene [22]. Hydrophilicity is well correlated with anti-fouling performance [23, 24] and is especially important in oil-water separation applications because in-air hydrophilic surfaces are underwater oleophobic [48]. The membranes had a rated molecular weight cutoff (MWCO) of 75 kDa which translated to an average pore size[1] of approximately 19 nm. Membrane permeability, averaged over seven samples was determined to be 488.3 ± 6.2 L/m^2-hr-bar using a dead-end cell with DI water and a stirrer at 200 rpm. Permeability was calculated by $A = J/\Delta P$ where J was the steady state flux (L/m^2-hr) during the DI filtration run and ΔP was the trans-membrane gauge pressure (bar).

In-air advancing water contact angles were $55 \pm 5°$ and static in-air water contact angles were $34 \pm 9°$ using a goniometer (Model 500-F1, ramé-hart). Surface zeta potential was measured to be -71.7 ± 0.723 mV (SurPASS, Anton-Paar) at a conductivity of 0.17 mS/cm and the neutral pH values used in this study of pH$\sim$ 6.5.

2.3.4 Dead-end batch experiments

A stainless steel stirred cell (HP4750, Sterlitech) was used for dead-end batch experiments. Pressure was measured using a pressure gauge (GH-68930-10, Ashcroft) and was supplied to the cell via a nitrogen tank connected to a two-stage gas regulator (Airgas) and an accurate low pressure gas regulator (R-800-3.5, Airtrol) in series. The cell has an active membrane area of 14.6 cm^2. DI water was first filtered through the as received membranes for at least 2 hours prior to emulsion separation. A stirrer at 200 rpm was used during DI filtration runs to minimize from contaminants in the cell. Liquids in the cell were at room temperature, 23 ± 1 °C, throughout all experiments.

Feed gauge pressure was set to between 8 and 9 kPa during experiments so that membranes gave a flux of 50 L/m^2-hr (LMH) during DI filtration runs. Details on how flux was

---

[1]Pore size can be approximated by $d_{pore} = 0.11 \cdot MWCO^{0.46}$ where d_{pore} is pore diameter (nm) and MWCO is molecular weight cut-off (Da) [49]

measured and analyzed is given in the Appendix A. At low hydraulic pressures we must account for the gravitational head from the ≈16.8 cm high cell, which resulted in a total gauge pressure of between 9.95 and 10.95 kPa at the membrane surface. The maximum head loss during filtration runs occurred during Tween 80 and Triton X-100 experiments at 10 hours which reduced pressure at the membrane surface by 16-18%. However, for all experiments at early times (< 5 hours) pressure did not decrease by more than 10%.

For emulsion filtration experiments, 300 mL of emulsion was added to the cell without a stir-bar and pressure was set to the same value for which a flux of 50 LMH was obtained in the DI water filtration run. The cell was thoroughly cleaned after each experiment with isopropyl alcohol (99.9%, Sigma-Aldrich) and DI water. All experiments with model oil-water emulsions were repeated twice. Due to a lack of sufficient feed volume, each produced water sample was filtered only once. Tests were performed for 10 hours at which point steady state fluxes were attained.

2.3.5 Crossflow experiments
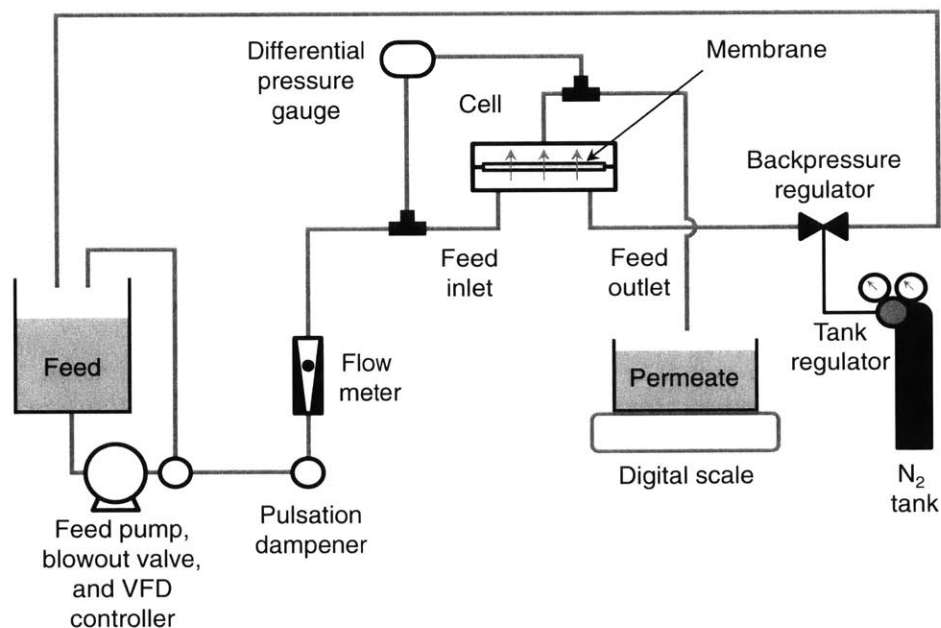
Figure 2-2: Schematic of experimental setup.

Figure 2-2 shows a schematic diagram of the experiment. A feed tank connects to a

positive displacement feed pump (Hydracell F-22 Series, Wanner) controlled by a variable frequency drive (VFD) (GS1-21P0, Automation Direct) which circulates pressurized feed through the system. After passing through an over-pressure bypass valve (C46, Wanner), a pulsation dampener to smooth flow and pressure fluctuations (Blaco), and a flow meter (Ultrapure Flowmeter, McMaster), the feed enters a crossflow cell (Delrin CF042, Sterlitech) which houses the membrane. According to the manufacturer, the active membrane area in the cell was 42 cm^2, the cell width was $w = 9.40$ cm, and the height of the cell channel was $h = 1.73$ mm without a spacer. A 0.864 mm (34 mil) spacer was used in the cell to simulate the effect of turbulence promoters in spiral wound UF modules and is representative of those used in industry [36]. Use of the spacer reduces the effective channel height to $h = 0.864$ mm.

The permeate exits the crossflow cell and its mass was recorded versus time using an electronic scale (Scout Pro 6000x0.1g, Ohaus). The feed exits the crossflow cell as concentrate and is returned to the feed tank. The oil to emulsion volume fraction does not increase beyond 5% during long experiment times. Liquids in the tank were at room temperature throughout all experiments.

Pressure was precisely maintained in the flow cell with a flow-through back pressure regulator (EB1HF2, Equilibar) fed by a nitrogen tank connected to a two-stage gas regulator (Airgas). Pressure was measured using a differential pressure gauge (DPG409-015DWU, Omega) which output 0-5 Vdc to a data acquisition system (OM-USB-1408FS, Omega) read by a desktop computer.

The volumetric flow rate for all experiments was set to 0.1 GPM. Using the effective channel height (with spacer) h, cell width w, and conversion constants the velocity was $v = 7.77$ cm/s which yields a Reynolds number of Re $= \rho v D_h / \mu = \rho v (2hw) / \mu (h + w) = 133$ assuming a dynamic viscosity equal to that of pure water[2]. This Reynolds number describes laminar internal flow through the channel. Small velocities relative to those used in commercial systems [36, 37] were used in our experiments to exacerbate fouling.

As received membranes were placed into the crossflow cell and DI water was first circu-

---

[2]According to Einstein's equation valid for emulsions with small volume fraction (small ϕ), colloid viscosity is described by $\mu = \mu_{continuous} \cdot (1 + 2\phi_{dispersed})$ where $\phi_{dispersed} = V_{dispersed}/V_{solution}$ [8]. For the low volume fractions used in this study ($\phi = 8 \times 10^{-4}$), the colloid viscosity is effectively that of the continuous water phase.

lated through the system. Feed pressure was adjusted for each run until an initial flux of 50 ± 1 LMH was obtained. These feed pressures were 12.1 ± 1.0 kPa and slightly deviate from those used in the dead-end tests due to minor hydrostatic differences in the feed and permeate inlets to the differential pressure gauge. After the baseline flux was obtained for one hour, the permeate tank was emptied and concentrated emulsion mixture and DI water were added to the feed tank until the tank and system lines contained a total of 10 L of solution as indicated by a calibrated marker inside of the tank.

After each experiment, the tank and system lines were drained using bypass lines and DI water was added to the tank and circulated through a filter (EW-01508-93 0.5 μm cartridge, Cole-Parmer) to clear the system of contaminants. All experiments with model oil-water emulsions were repeated twice and averaged. Tests were performed for 3 hours at which point steady state fluxes were attained.

2.4 Results and discussion

2.4.1 Model emulsions

Figure 2-3 shows flux as a function of time for hexadecane-in-water emulsions stabilized by anionic (SDS), nonionic (Tween 80), and cationic (CTAB) surfactants. Initial fluxes during dead-end batch experiments given in Fig. 2-3a and crossflow experiments given in Fig. 2-3b were set to $\sim$ 50 LMH and tests were allowed to continue until steady state had been achieved (10 hrs for dead-end batch and 3 hrs for crossflow tests). Table 2.4 gives the average initial and steady fluxes as well as the average specific volume (permeate per unit area of membrane) including standard deviation for each surfactant stabilized model emulsion.

Although we may expect cationic surfactant-stabilized emulsions to foul membranes most severely due to an electrostatic attraction between the positive surfactant potential and negative membrane potential, in dead-end batch tests we observed that both SDS and CTAB had a low steady state flux and specific permeate volume. Fouling was least severe for Tween 80 stabilized emulsions in terms of both a higher steady state flux and greater specific volume as shown in Table 2.4. This is very likely due to the fact that Tween 80

33

has the lowest absolute zeta potential of all surfactants used and therefore has the lowest droplet-droplet electrostatic repulsion; leading to increased flocculation/coalescence and creaming (the rise of oil flocs or coalesced oil in a gravitational field) within the cell.

In crossflow tests, we observed a hierarchy for steady state flux which indicates that droplet-membrane interactions are more important than droplet-droplet interactions: anionic stabilized emulsions fouled the least, followed by nonionics, then cationic stabilized emulsions. Interestingly, the initial rate of fouling for the nonionic surfactant is much greater than the cationic emulsion. This behavior is also observed in the dead-end batch tests. Note that although dead-end tests were performed at a pressure which yielded 50 LMH during a DI water membrane preparation step, the nonionic emulsion initial flux for all tests was roughly 35 LMH. This is the same rapid fouling behavior also observed in crossflow tests. This is could be due to the significant hydrophilicity of the Tween 80 surfactant head relative to SDS and CTAB (as evidenced by the molar weight of the hydrophilic portion of each surfactant M_h in Table 2.2) which may interact with the hydrophilic membrane surface more than cationic stabilized emulsions which experience electrostatic attraction with the membrane surface. Also, once nonionic surfactants and nonionic-stabilized oil droplets reach the membrane surface, they may be able to form close-packed layers of a greater density than surfactants which repel each other by electrostatic forces. Jönnson and Jönnson also found severe fouling for Tween 80 (without oil) on hydrophilic, but not hydrophobic, membranes past the critical micelle concentration (CMC) of Tween 80 [39].

Because the concentration of Tween 80 exceeded the CMC in our tests, we also used Triton X-100 nonionic surfactant in several hexadecane-in-water emulsion fouling tests. Triton X-100 has a higher CMC than Tween 80. These tests were run in dead-end batch mode to ensure that the same destabilization phenomenon which resulted in a higher flux for Tween 80 than SDS and CTAB stabilized emulsions was due to a nearly neutral zeta potential and not due to being above the CMC. Figure 2-4 shows that Triton X-100 emulsions are indeed 'broken' in dead-end batch filtration. We observed that flux declined rapidly and subsequently rose after roughly an hour of fouling in multiple tests. We attribute this behavior to a mass flocculation or coalescence event which occurred only when a critical number of stabilized oil droplets reached the surface of the membrane and were brought close enough

(a) Dead-end batch
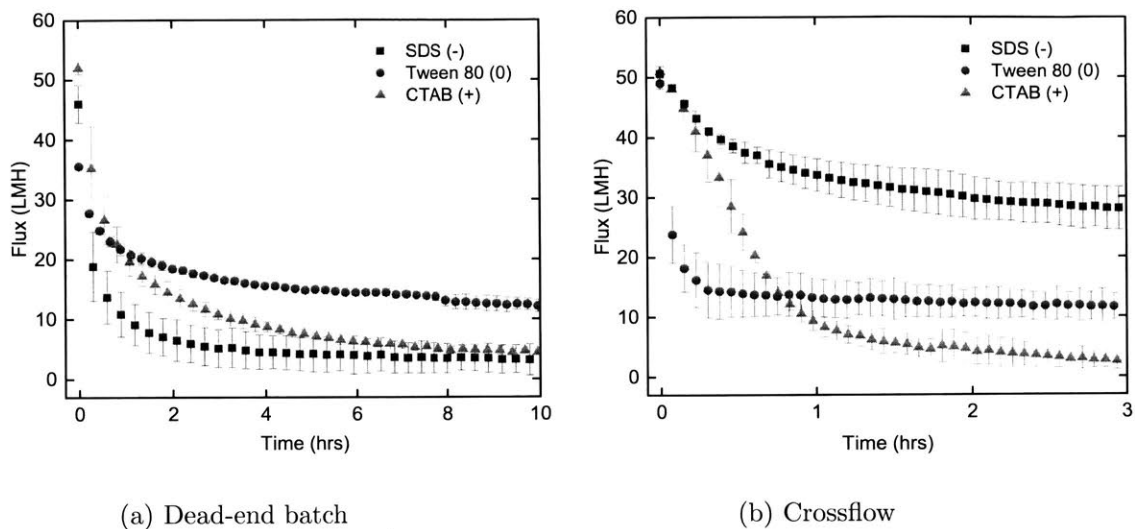
(b) Crossflow

Figure 2-3: Flux vs. time for hexadecane-in-water emulsions stabilized by anionic SDS (squares), nonionic Tween 80 (circles), and cationic CTAB (triangles) surfactants in (a) dead-end batch and (b) crossflow.

for the Van der Waals force to overcome the weaker electrostatic repulsive force. We surmise that nonionic stabilized oil-in-water emulsions can be 'broken' in dead-end batch filtration more easily than ionic stabilized emulsions.

Table 2.4: Initial flux J_0, steady state flux J^*, and specific volume v (L/m^2) results for model emulsion fouling runs.

Surfactant	Dead-end batch			Crossflow		
	J_0	J^*	v	J_0	J^*	v
SDS	46.01 ± 3.17	3.33 ± 2.22	60.17 ± 28.53	50.67 ± 3.30	27.98 ± 3.30	100.94 ± 11.23
Tween 80	35.62 ± 0.18	12.18 ± 0.69	161.54 ± 5.47	50.57 ± 1.34	19.53 ± 8.65	42.73 ± 6.15
CTAB	52.00 ± 1.05	4.55 ± 0.45	104.54 ± 12.04	50.97 ± 0.28	2.64 ± 1.41	36.74 ± 2.32
Triton X-100	41.76 ± 3.40	16.73 ± 1.14	130.85 ± 0.21	-	-	-

Flux, time, volume, initial flux, and steady state flux were used with the time-flux-volume set of equations in Table 2.1 to determine R^2 values and fitting parameters K_n as shown in Fig. 2-5 for CTAB emulsion fouling in dead-end batch and crossflow filtration. Note that nearly all of the R^2 values for each mechanism are above 0.9, including the standard blocking mechanism. With obtained values of K_n we modeled the flux decline for each emulsion and mechanism using the time-flux set of equations. This resulted in values of AAPD which we used to infer which mechanism may have played a dominant role. While it is likely that multiple mechanisms may have simultaneously contributed to fouling, or

35
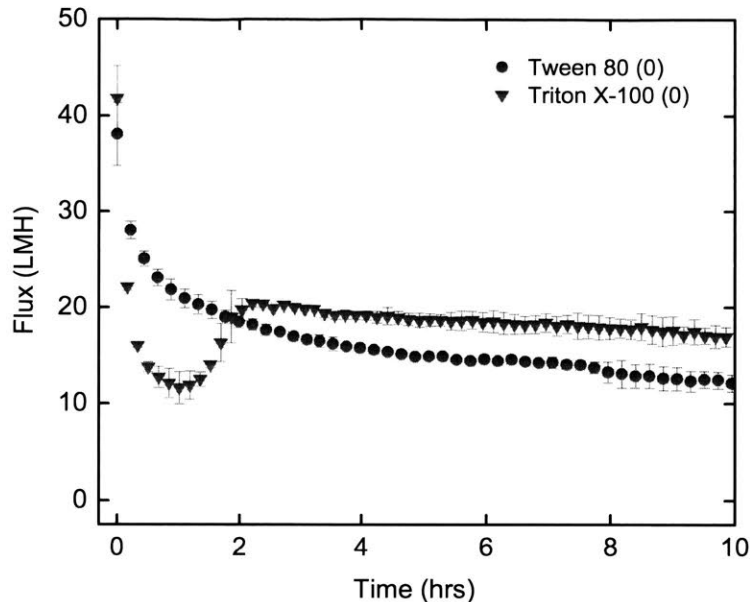
Figure 2-4: Dead-end batch filtration of Tween 80 (circles) and Triton X-100 (inverted triangles) stabilized emulsions. Data points are averages and error bars are standard deviations from two experiments for each surfactant.

that one mechanism may have dominated at earlier experiment times than others, we apply the blocking laws to the entire flux decline time series to infer which mechanism may have dominated throughout the process. We do not apply fouling models to the Triton X-100 fouling curves because their non-monotonic decline yields errors.

Values of AAPD, R^2, and K_n averaged over two runs categorized by stabilizing surfactant and fouling mechanism are provided in Table 2.5. The standard deviation of AAPD values from the two runs is also included. Mechanisms with the lowest average AAPD value have a bolded row for ease of reference. We can infer that SDS and CTAB emulsions largely resulted in either partial or complete blocking in both dead-end batch and crossflow tests. This is in agreement with the conventional model for oil fouling: deposition and spreading of oil [50] on the surface of the membrane leading to pore blockage.

From Table 2.5 we may infer that Tween 80 emulsion fouling was dominated by cake blocking in both dead-end batch and crossflow filtration. Other studies in literature also found evidence of cake filtration when using nonionic surfactants to stabilize diesel and

36
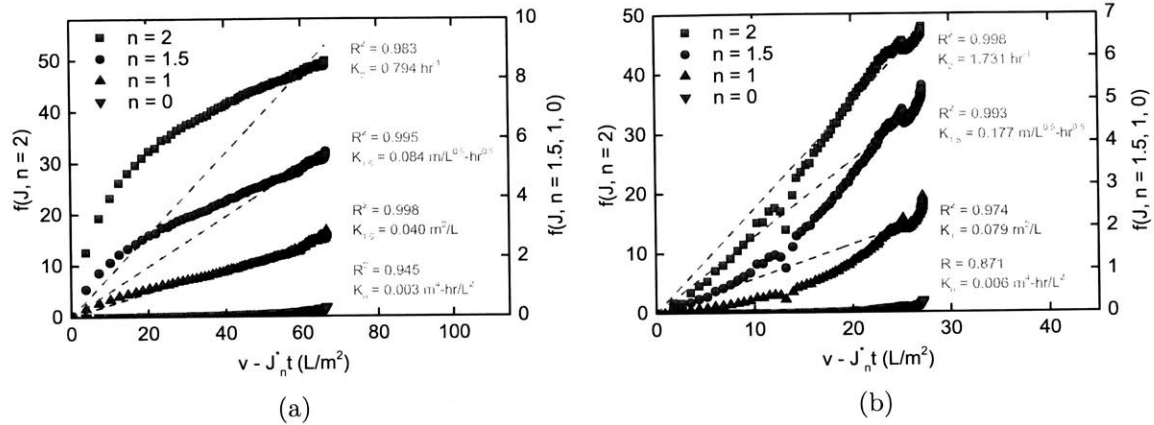
Figure 2-5: Blocking filtration modeling for fouling of CTAB stabilized emulsion in (a) dead-end batch and (b) crossflow.

motor oil emulsions for fouling of polyvinylidene fluoride (PVDF) membranes [51, 52]. Although those authors used a constant flux rather than constant pressure crossflow setup, they found evidence for cake formation followed by a pseudo-steady state operation where trans-membrane pressures reached a constant value. Similar behavior may be occurring in our study, where the rate of fouling for Tween 80 is initially high but decreases to nearly zero in both dead-end batch and crossflow tests.

Note that standard blocking did not appear likely for any emulsion. This is likely due to the extremely small average pore size of the PAN membrane used in this study (0.019 μm) relative to the average oil droplet size in each emulsion ($\sim 0.90 \pm 1.27$ μm). Also, although standard blocking R^2 values may have been high for some emulsions, corresponding AAPD values were also high. This is because the time-flux-volume set of equations allows for a steady state flux term J^* while the time-flux set does not, yielding high AAPD during model to data comparisons but high R^2 values during linear fitting.

2.4.2 Produced water samples

Figure 2-6 shows flux decline for two produced water samples from D-J Basin and Barnett in dead-end batch filtration. Although pressure was set to give an initial flux of $\sim$50 LMH, resulting initial fluxes were around 40 LMH for both samples. From Fig. 2-3a, we see that high steady state fluxes in the Tween 80 and Triton X-100 stabilized emulsions are due to smaller droplet-droplet electrostatic repulsive forces relative to SDS and CTAB stemming

Table 2.5: Statistics for blocking law fitting of model oil-water emulsions. Average absolute percentage deviation AAPD, goodness of fit R^2 values, and fitting parameter K_n are averaged for two runs and provided for each fouling mechanism. Standard deviation for AAPD is provided. Mechanism statistics with lowest AAPD is bolded for ease of reference. Units for fitting parameters are: complete K_2 (hr^{-1}), standard $K_{1.5}$ ($m/L^{0.5}\text{-}hr^{0.5}$), partial K_1 (m^2/L), and cake K_0 ($m^4\text{-}hr/L^2$).

Model oil-water emulsions

Surfactant/configuration	SDS/Dead-end			Tween 80/Dead-end			CTAB/Dead-end		
Fouling mechanism	AAPD	R^2	K	AAPD	R^2	K	AAPD	R^2	K
Complete	26.88 ± 11.70	0.988	1.757	9.75 ± 2.27	0.977	0.626	16.68 ± 6.05	0.988	0.853
Standard	30.42 ± 2.91	0.996	0.201	25.54 ± 1.65	0.984	0.064	18.21 ± 5.97	0.997	0.086
Partial	**7.05 ± 3.99**	**0.998**	**0.105**	5.47 ± 1.74	0.990	0.027	**9.03 ± 0.17**	**0.996**	**0.038**
Cake	19.80 ± 15.86	0.960	0.012	**3.30 ± 1.98**	**0.995**	**0.001**	21.21 ± 1.10	0.934	0.003

Surfactant/configuration	SDS/Crossflow			Tween 80/Crossflow			CTAB/Crossflow		
Fouling mechanism	AAPD	R^2	K	AAPD	R^2	K	AAPD	R^2	K
Complete	1.65 ± 0.01	0.998	1.406	18.40 ± 12.70	0.937	5.053	**21.20 ± 14.13**	**0.995**	**1.652**
Standard	58.52 ± 0.95	0.999	0.111	76.35 ± 4.09	0.944	0.478	29.69 ± 12.69	0.984	0.013
Partial	**1.11 ± 0.22**	**0.999**	**0.0035**	14.15 ± 10.21	0.951	0.189	55.78 ± 37.71	0.955	0.084
Cake	1.71 ± 0.67	0.996	0.001	**9.40 ± 7.15**	**0.962**	**0.008**	65.46 ± 38.05	0.818	0.008

from low absolute zeta potentials. Noting from Table 2.3 that the D-J Basin and Barnett samples had zeta potentials of -4.11 and -2.42 mV, respectively, we may expect them to also attain high steady state fluxes. The fact that both emulsions foul as severely as the SDS and CTAB stabilized emulsions in Fig. 2-3a suggests that the stabilizing agents in the produced water emulsions rely on steric rather than electrostatic repulsion [8]. This could arise from the adsorption of solid particles such as polymers, asphaltenes, or colloidal silica at the oil-water interface [13]. The fact that the produced water samples had a neutral zeta potential and remained cloudy for months after extraction is further evidence of steric rather than electrostatic repulsion.

It could also be the case, however, that the severe fouling in the produced water samples resulted from pore blockage by other total suspended solids, such as small soil particles or organic matter, rather than suspended oil droplets. Nevertheless we conclude that nonionic surfactant stabilized emulsions, despite having near neutral zeta potentials relative to SDS and CTAB emulsions, do not foul similarly to produced water samples in dead-end batch filtration due to poor droplet stability during concentration.

By fitting blocking models to the flux decline curves, we can infer that partial fouling may have played a dominant role during produced water sample fouling in dead-end batch filtration. This is a similar result to what was found in the ionic surfactant-stabilized
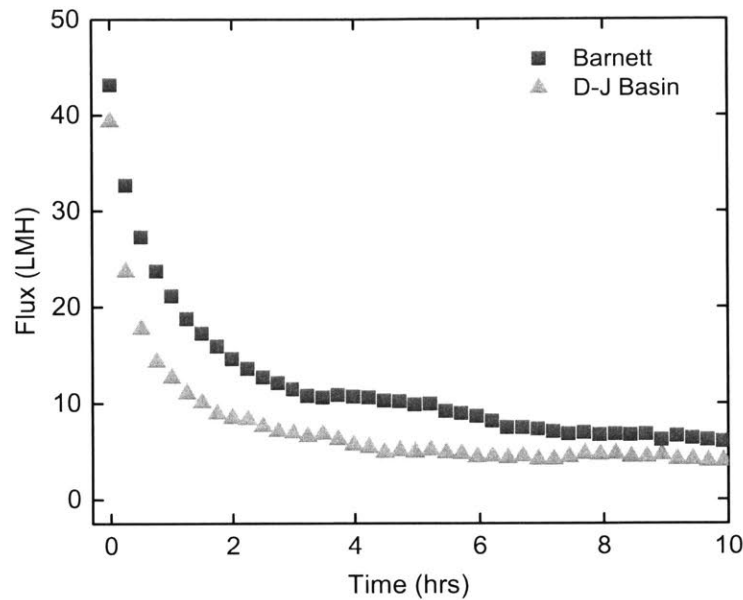
Figure 2-6: Flux vs. time for D-J Basin (squares) and Barnett (circles) produced water samples in dead-end batch filtration. Initial fluxes were 39.3 and 43.2 LMH for D-J Basin and Barnett samples, respectively.

emulsions shown in Fig. 2-3a. Table 2.6 gives the R^2, K_n, and AAPD values for each sample and fouling mechanism. We observe that D-J Basin fouls more than Barnett not only visually from Fig. 2-6 but also because D-J Basin has a greater blocking parameter K_1 than Barnett. This is very likely due to the fact that the D-J Basin sample TOC value is a factor of 3.2 greater than that of Barnett.

Table 2.6: Statistics for blocking law fitting of produced water. Average absolute percentage deviation AAPD, goodness of fit R^2 values, and fitting parameter K_n are given for each fouling mechanism. Mechanism statistics with lowest AAPD is bolded for ease of reference. Units for fitting parameters are: complete K_2 (hr^{-1}), standard $K_{1.5}$ (m/L$^{0.5}$-hr$^{0.5}$), partial K_1 (m^2/L), and cake K_0 (m^4-hr/L^2).

Produced water samples

| Sample/configuration | D-J Basin/Dead-end | | | Barnett/Dead-end | | |
Fouling mechanism	AAPD	R^2	K	AAPD	R^2	K
Complete	14.11	0.990	1.224	31.01	0.974	0.424
Standard	63.64	0.997	0.142	50.24	0.988	0.047
Partial	**5.21**	**0.999**	**0.072**	**6.91**	**0.998**	**0.023**
Cake	14.72	0.967	0.006	10.50	0.973	0.002

2.5   Conclusions

In this chapter, we have investigated the role that surfactant charge plays in the fouling of a polyacrylonitrile ultrafiltration membrane by surfactant-stabilized oil-in-water emulsions. Model emulsion concentrations and droplet size distributions were representative of obtained produced water samples. Six produced water samples were characterized and two were tested in dead-end batch filtration. Model emulsions were filtered in dead-end batch and crossflow modes.

Results from this study are as follow:

- In dead-end batch filtration, cationic and anionic stabilized emulsions foul membranes most severely while nonionic emulsions are observed to destabilize easily.

- In crossflow filtration, cationic stabilized emulsions result in the lowest steady state flux followed by nonionic then anionic emulsions.

- Results suggest that droplet-droplet electrostatic repulsion dominates fouling in dead-end batch filtration while droplet-membrane electrostatic interactions are more relevant in crossflow operations.

- Applying fouling blocking models, we may infer that nonionic emulsions form cakes while anionic and cationic surfactants completely and partially block membrane pores indicative of a thin coating of oil on the membrane surface.

- Despite having nearly neutral zeta potentials, the two produced water samples filtered in dead-end batch mode yield fouling similar to anionic and cationic (not nonionic) emulsions, implying that oily wastewaters in the produced water space may be stabilized by steric rather than electrostatic repulsion.

- Two tested produced water samples appeared to foul membranes in dead-end batch filtration via partial pore blocking.

On the basis of steady state flux results, we therefore recommend that anionic surfactants be used to stabilize emulsions treated by crossflow filtration and nonionic surfactants be used to stabilize emulsions treated by dead-end batch filtration.

Acknowledgments

Chapter 3

A single-step multifunctional membrane for oil-water separation and in-situ organic pollutants degradation: Experiments and performance model

Talal F. Qahtan[1], Leonardo D. Banchik[2], Mohammed A. Gondal, Gibum Kwon, Divya Panchanathan, Mohammed A. Dastageer, and Gareth McKinley

Chapter abstract

In this work we present a single-step multifunctional membrane which uses two distinct coatings on a porous mesh to simultaneously separate oil emulsions via gravity and decontaminate organics in the water permeate in-situ. Our top surface is a novel superhydrophilic/superoleophobic, chemically robust coating which allows water to pass while oil is retained with high oil rejection ($\sim$99.99%) for bulk oil-water mixtures and surfactant sta-

---

[1]TFQ contributed to the work in this chapter by performing all experiments and aiding in writing of the manuscript.

[2]LDB contributed to the work in this chapter by collaborating on the novel feed-side membrane coating, performing all modeling, and aiding in writing of the manuscript.

bilized oil-in-water and water-in-oil emulsions without the need for membrane pre-wetting. The bottom surface (permeate side) is a superhydrophilic titanium dioxide (TiO_2) coating which allows for highly effective (~99.9%) in-situ degradation of organic pollutants present in the water phase when exposed to UV radiation. Our multifunctional membrane allows for flexibility in the choice of photocatalyst because the separation and photocatalysis functions are provided by two separate coatings on different sides of the membrane. Additionally, by illuminating UV from the bottom of our system apparatus, we reduce UV attenuation relative to systems which transmit radiation through a column of turbid feed solution. In addition to demonstrating excellent bulk and emulsified oil-water mixture separation and organic pollutant degradation performance, we present a model (mean error = 1.2%) to predict the purification performance of our multifunctional membrane as a function of relevant system parameters. Our model provides a figure of merit for multifunctional membrane systems which can be used to compare the performance of other researchers systems.

3.1 Introduction

Stringent environmental protection legislation has led to many industries such as oil and gas, metal working, tanneries, and food production to invest in better technologies for separating oil-water emulsions and removing organic pollutants before discharging wastewater streams into the environment [2]. Due to their ability to reject fine emulsified droplets of oil (droplet diameter < 10 μm) and their relatively lower energy and chemical consumption compared to flocculation, hydrocyclones, and dissolved air flotation, ultra- and micro-filtration membranes are often applied for oily wastewater treatment [5, 36]. While these membranes can effectively separate emulsified oil droplets, they can still be energy intensive and are not capable of degrading organics in the permeate in-situ. Additional organics degradation may be needed in cases where permeates are still contaminated with organic pollutants, such as dyes or Phenol, and when permeate quality requirements are high [15]. Combining the separation and degradation steps into a single-step unit operation by using a specialized membrane could save wastewater treatment plant operators significant capital and operational expenses.

Several studies have investigated the use of hydrophilic (HL, advancing water contact angle < 90°)/oleophobic (OB, advancing oil contact angle > 90°) and super hydrophilic (SHL, water contact angle = 0°)/superoleophobic (SOB, advancing oil contact angle > 150° and sliding angle < 10°) coatings for oil-water separation [26, 29, 30, 53]. Many studies have also investigated the kinetics and performance of TiO_2 and ultraviolet (UV) enabled photocat-

alytic degradation of organic materials [54–59]. Fewer studies, however, have used photocatalysis to degrade pollutants in combination with oil-water separation processes [60–62]. To the authors knowledge, this is the first study to fabricate a single-step, robust, multifunctional membrane via spray coating with in-air selective wettability towards oil and water (oil is retained) and photocatalytic properties to simultaneously separate suspended oil from water as well as degrade organics in the permeate. Compared to the multifunctional membranes reported in literature which use in-air superhydrophilic/superoleophilic coatings, such as TiO_2, our membranes are not affected by the issue of dry-out and oil penetration due to their in-air SHL/SOB wetting characteristics [26]. We demonstrate, for the first time, two separate coatings for the feed (water to be treated) and permeate (treated water) sides of our membrane. The feed-side coating (coating facing the feed) is chemically robust and possesses in-air superhydrophilicity (water contact angle $= 0°$) and superoleophobicity (advancing oil contact angle $> 150°$) with very low contact angle hysteresis (sliding angle $< 5°$) which allows water to pass through while oil is retained with high rejection ($\sim 99.99\%$ rejection) for bulk oil-water mixtures and oil-in-water and water-in-oil surfactant stabilized emulsions. The permeate-side coating (coating facing the permeate) is comprised of a photocatalytic material, titanium dioxide, and allows for highly effective ($\sim 99.9\%$) in-situ degradation of organic pollutants present in the water phase when exposed to UV radiation. Our multifunctional membrane allows for flexibility in the choice of photocatalyst because the separation and photocatalysis functions are provided by two separate coatings on different sides of the membrane. Other usable photocatalysts might include nitrogen or palladium doped or co-doped metal oxide (TiO_2, WO_3, ZnO, NiO, CuO) films, for instance, which allow for photocatalysis using visible light or sunlight [15, 63]. Additionally, by illuminating UV through the bottom of the device rather than through the feed into a feed-side coating, our system is not affected by severe UV attenuation through the turbid feed solution column according to the Beer-Lambert law [64]. We also derive and present a highly accurate analytical model to predict the degradation performance of our membrane as a function of relevant system parameters. Our model provides a figure of merit, β with units of $cm/mW^{1/2}$-s, for photocatalytic separation systems which can be used to compare the degradation performance of multifunctional membranes used in batch

or continuous mode by other researchers.

3.2 Experimental section

3.2.1 Materials and membrane fabrication

The substrates used in this study were 316 stainless steel mesh (2 micron pore size, T316L, TWP) and glass slides (VWR Microscope Slides, Germany). SiO_2 nanoparticle suspension with a concentration of 15 mg/mL was prepared by adding SiO_2 nanoparticles (average diameter 7 nm, Aerosil 380, Evonik Industries) into acetone (Sigma Aldrich) using a magnetic stirrer at 800-1000 rpm. Then, 5 mg of SF-100 (Super-fast instant adhesive, 3M Scotch-Weld) was added per 1 mL of SiO_2 nanoparticle solution to yield a SiO_2/SF-100 solution in acetone. Fluorosurfactant solution (Capstone FS-50, DuPont) was prepared by diluting FS-50 with ethanol (Sigma Aldrich) to attain a 45 mg/mL solution. A TiO_2 nanoparticle solution with a concentration of 5 mg/mL was prepared by adding TiO_2 nanoparticles (Aeroxide TiO_2 P 25, Evonik Industries) in tetrahydrofuran (THF, Sigma Aldrich) using a magnetic stirrer at 800-1000 rpm. All meshes and glass substrates used in this study were rinsed with acetone, isopropanol, and deionized (DI) water, respectively, to remove contaminants and subsequently dried before each coating process. A spray gun (nozzle diameter of 0.38 mm, Paasche) operated with compressed nitrogen at 200 kPa was used. The gun was maintained at a distance of 10 cm from the glass substrates/meshes for all coatings. For the SSF coating, 1 mL of SiO_2/SF-100 solution and 0.5 mL of FS-50 per 1 cm^2 of substrate are sequentially sprayed on the feed side of the mesh/glass. For the TiO_2 coating, 1.5 mL of the TiO_2 solution per 1 cm^2 of substrate was sprayed onto the permeate side of the mesh/glass.

3.2.2 Preparation of bulk oil-water mixtures and oil-water emulsions

Three bulk oil-water mixtures (1:1 by volume) were used in this study hexadecane ($\gamma_{LV} = 27.5$ mN/m). Three hexadecane-water emulsions (1:4, 1:1 and 4:1 by volume) were prepared by mixing hexadecane and water using a magnetic stir bar (at 800 - 1000 rpm) with 0.3 mg per mL of solution of sodium dodecyl sulfate (SDS, Sigma Aldrich) for the 1:4 and 1:1 emulsions and Span80 (Sigma Aldrich) for the 4:1 emulsion. The 1:4 and 1:1 emulsions

were oil-in-water type and the 4:1 emulsion was water-in-oil type. This is due to the HLB value of the stabilizing surfactant used for each mixture and was also verified optically by using oil and water soluble dye in each mixture to determine the continuous phase. A small degree of demulsification was observed over time for some emulsions. Feed emulsion droplet sizes were digitally extracted from high resolution optical microscope images using the *imfindcircles* function in the MATLAB image processing toolbox. Droplet size distributions of the permeate were measured using a differential light scanning device (Microtrac Nanotrac Wave II).

3.2.3   UV irradiation

UV irradiation was provided and adjusted by a collimating adapter (OmniCure Adjustable Spot Collimating Adapter) through a fiber optic cable from a Mercury Vapor Short Arc UV lamp source (Omnicure S2000). The UV intensity was measured by OmniCure R2000 UV Radiometer.

3.2.4   Surface characterization

Static and advancing contact angles and sliding angle measurements

Droplet volumes used in this study were 5 μL. Static and advancing contact angle measurements were performed using a Goniometer Kruss Easy Drop DSA20X. Sliding angles were measured by increasing the elevation angle of the goniometer stage until each oil droplet began moving due to an imbalance of forces.

Microscopy

A field emission scanning electron microscope (FE-SEM, TESCAN ultra high resolution), was used for surface morphology analysis. An optical microscope (NikonECLIPSE Ti) was used to take optical images of oil-water feed emulsions and water permeate.

Characterization of oil-water separation and organic pollutant degradation efficiencies

The oil content in all permeates after oil-water separation was measured using thermogravimetric analysis (STA 449F3-Jupiter, Netzsch). The temperature of each sample was increased from room temperature to 105 °C at a rate of 5 °C/min, and then held at 105 °C for 50 min. The boiling points of water and hexadecane are 100 °C and 287 °C, respectively. The loss in water weight was used to estimate the oil rejection. The concentration of methyl blue dye was measured with a UV-VIS spectrophotometer (Jasco 670).

3.3   Results

Figure 3-1 shows schematic illustrations of the multifunctional membrane, its fabrication procedure, and wettability. The in-air SHL and SOB wetting behavior of the feed-side enables solely gravity-driven oil-water separation without the need for pre-wetting with water while the photocatalytic property of the permeate-side of the membrane enables in-situ degradation of organic pollutants from the water phase upon UV irradiation as shown in Fig. 3-1a. We fabricated our membrane using a simple spray-coating method as shown in Fig. 3-1b. First, silicon dioxide (SiO_2) nanoparticles, SF-100 (cyanoacrylate), and FS-50 (fluoro-surfactant) were sequentially sprayed onto the feed side of a stainless steel mesh membrane with small pores (2 μm). We used small pores to improve rejection of small emulsified oil droplets which are common in wastewaters containing surfactant stabilized oil-water emulsions [11, 19, 65]. This coated surface exhibits in-air SHL and SOB. SiO_2 nanoparticles were added to create hierarchical roughness on the surface, see Supplementary Fig. B-2, which is essential for achieving superhydrophilicity and superoleophobicity through a Cassie-Baxter state of wetting [66, 67]. SF-100 was added to enhance the durability of the membrane coating in the presence of water and we found that its addition bound the SiO_2 and FS-50 more effectively to the substrate.

The permeate side of the membrane was coated with TiO_2 nanoparticles which, under UV illumination, can degrade organic pollutants contacting the surface via catalytic redox reactions [55–58]. Henceforth, we will refer to the feed-side layer coating as SSF

(SiO_2/SF-100/FS-50), the permeate-side layer coating as T (TiO_2) and their combination as SSFT (SiO_2/SF-100/FS-50/TiO_2). From Field Emission Scanning Electron Microscopy (FE-SEM), SiO_2 nanoparticles were found to form granular structures affixed to the stainless steel mesh with micro and nanoscale hierarchical surface roughness (Fig. 3-1b, upper part). FE-SEM images of the micro-nano hierarchical surface morphology of the TiO_2 coated membrane are shown in Fig. 3-1b (lower part) and we can visualize a high surface area for photocatalytic degradation of organic pollutants.
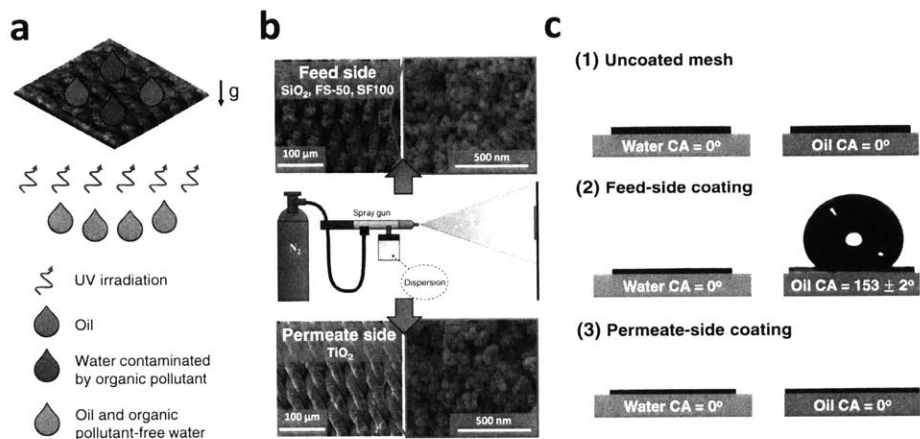
Figure 3-1: Operation, surface morphology, and wettability of multifunctional membrane for oil-water separation and in-situ degradation of organic pollutants. (a) Coated multifunctional membrane can separate oil and water without water pre-wetting by gravity and degrade organic pollutants from the water phase upon UV irradiation. (b) Spray-coating based fabrication of the SSFT (SiO_2/SF-100/FS-50/TiO_2) multifunctional membrane: SiO_2/SF-100 and FS-50 (SSF) dispersions are sequentially sprayed onto the feed side of the membrane (side facing the water to be treated) while a TiO_2 (T) dispersion is sprayed onto the permeate side of the membrane (side facing the treated water). (c) Water and oil (hexadecane) wetting behavior on uncoated membrane (1), SSF coated membrane (2), and TiO_2 coated membrane (3).

To evaluate the wettability of our membranes, we measured the apparent advancing contact angles for water and hexadecane on SSF and TiO_2 coated stainless steel mesh membranes as shown in Fig. 3-1c. For comparison, we measured the apparent advancing contact angles for water and hexadecane on a neat stainless steel mesh. It is clear that the uncoated stainless steel mesh is superhydrophilic (SHL, $\theta^*_{wa} = 0°$) and superoleophilic (SOL, $\theta^*_{oa} = 0°$) in an air environment, while the SSF coated membrane is SHL ($\theta^*_{wa} = 0°$) and

SOB ($\theta_{oa}^* = 153 \pm 2°$) in an air environment. This selective wetting behavior is attributed to a surface reconfiguration of the perfluorinated alkyl chains in the fluorosurfactant first characterized by Sawada et al. [68] and explored by others more recently [26, 27, 68, 69]. The in-air SHL and SOB wetting behavior of our SSF coated membrane indicates a potential for oil-water separation solely under gravity without the need for pre-wetting [26]. Furthermore, the extreme water wettability ($\theta_{wa}^* = 0°$) of the TiO$_2$ coated membrane as shown in Fig. 3-1c3 suggests that the organic pollutant-contaminated water can easily wet the photocatalytic surface on the permeate side of the membrane which should enhance the photo-degradation of organic pollutants during UV illumination.

Figure 3-2a shows a schematic illustration of the apparatus used for simultaneous oil-water separation and in-situ degradation of organic pollutants. Our SSFT coated membrane is sandwiched between two glass tubes, and we prevent leakage through the sides of the membrane using two oil-resistant rubber O-rings on both sides of the membrane pressed together with clips. The apparatus is tilted by 20 degrees with respect to the vertical axis so that the UV lamp is protected from the permeate falling during the operation of the system. The robustness of the SSF coated membrane, see Supplementary Fig. B-3 and Fig. B-4 for robustness of the TiO$_2$ coated membrane, was measured by observing the advancing oil contact angle in air vs number of passes as shown in Fig. 3-2b. The number of passes refers to the number of times water is added to the gravity separator. It is clear that the SSF coating is robust - having an almost constant oil contact angle of $153 \pm 2°$ after 10 passes. We attribute this result to the addition of SF-100 which was used to physically bind FS-50 and SiO$_2$ to the membrane. The SSF coated membrane also has a high constant flux (4015 ± 144 L/m^2-hr) for each pass during the separation process of bulk oil-water mixtures as shown in Fig. 3-2b. To test the degradation and separation performance of our multifunctional membrane, we first used the membrane for bulk hexadecane-water separation and in-situ MB dye degradation. A hexadecane-water mixture (1:1 by volume) with MB dye present in the water phase was poured into our apparatus without pre-wetting the membrane. MB dye is a model organic pollutant which has been used in many studies [56, 57, 62, 70, 71] and has negligible solubility in hexadecane. With a UV intensity of 1050 mW/cm^2 and 10 passes, neither oil nor MB dye were visually observed in the water permeate, demonstrating

high separation and purification performance. A thermogravimetric analysis plot of the permeate from the oil-water mixture showed extremely high oil rejection ($\sim 99.99\%$) as shown in Supplementary Fig. B-5. Oil rejection is defined as $R = 1 - C_p/C_f$ where C_p is the concentration by volume of oil in the final permeate and C_f is the oil concentration by volume in the initial feed. Figure 3-2c shows the absorbance spectrum of the MB dye as a function of the number of passes shown as contours. The first pass has 5 mg/L of MB dye initially and increasing passes decreases the peak wavelength at which MB dye is identified until the peak is no longer detected.
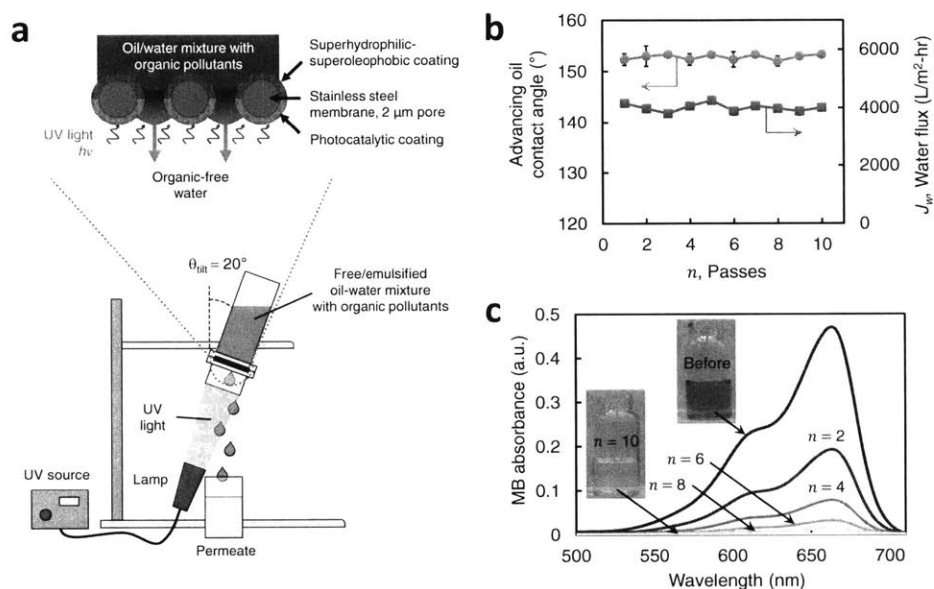
Figure 3-2: Schematic illustrations of the apparatus for gravity-driven bulk and emulsified oil-water separation and simultaneous in-situ degradation of organic pollutants using SSFT multifunctional membrane. (a) A schematic illustration of the separation and purification apparatus used in our experiments. (b) Contact angles for oil (hexadecane) on the feed-side of the multifunctional membrane and water flux as a function of the number of passes. The number of passes corresponds to the number of times that water is added to the separation apparatus. (c) Absorbance spectra of the organic pollutant after consecutive passes at UV intensity of 1050 mW/cm^2. Inset photos show water-contaminated MB dye before and MB dye-free water after 10 passes.

Figure 3-3 depicts the experimental apparatus and performance of the multifunctional membrane for the separation of surfactant-stabilized oil-in-water emulsions and in-situ organic pollutants degradation. MB dye-contaminated DI water was used to prepare three

surfactant-stabilized hexadecane-water emulsions with volume ratios of 1:4, 1:1, and 4:1 oil to water. The 1:4 and 1:1 emulsions were prepared with SDS surfactant and are oil-in-water while the 4:1 emulsion was prepared with Span80 surfactant and is a water-in-oil emulsion. The prepared emulsions were separated and treated by photocatalysis as shown in Fig. 3-3a. As a result of the selective wettability and photocatalytic activity of the multifunctional membrane, the oil phase is retained above the membrane during the separation of all the emulsions and MB dye-free water permeates through our membrane upon UV illumination ($I = 1050$ mW/cm^2) after only one pass as shown in Fig. 3-2b. Optical microscopy images and droplet size distributions of each emulsion and its permeate, provided in Supplementary Fig. B-6 and Fig. B-7, indicate that large droplets (> 2 μm) did not permeate through the multifunctional membrane. The oil rejection and MB dye degradation efficiency for each emulsion are given in Fig. 3-3c. These results indicate that our multifunctional membranes demonstrate excellent oil rejection efficiency ($\sim$ 99.99%) with surfactant stabilized emulsions in addition to simultaneous organics degradation efficiency ($\sim$99.9%) for all emulsions. Because the tested emulsions are more viscous than bulk water and because a gel layer of retained oil droplets inevitably forms on the membrane surface [36, 72], the flux is retarded to 190 ± 9, 128 ± 6, and 60 ± 3 L/m^2-hr for the 1:4, 1:1, and 4:1 oil-water emulsions, respectively. While these fluxes are lower than what is shown in Fig. 3-2c, they are still high for micro- and ultra-filtration processes [36] and are achieved solely by gravity. The flux retardation increases the residence time of water through the TiO$_2$-UV reactor and leads to complete degradation of organics in all emulsions with a single pass.

We now characterize the photocatalytic degradation performance of water contaminated by MB dye. Degradation efficiency is defined as $\alpha = 1 - C_t/C_0$ where C_t is the concentration of pollutant as a function of time and C_0 is the initial concentration (mg/L). The degradation efficiency of our multifunctional membrane can be seen to increase asymptotically towards 100% with increasing number of passes for a constant UV intensity ($I = 372$ mW/cm^2) until $\alpha = 95.3$% at 12 passes as shown in Fig. 3-4a. The same trends were observed with respect to increasing intensity for a constant number of passes (n = 2, 6, and 10) as shown in Fig. 3-4b. α reaches its maxima ($\sim$100%) for $I \geq 1050$ mW/cm^2 and $n = 10$ passes.

In order to better understand system performance for a wide variety of operating param-
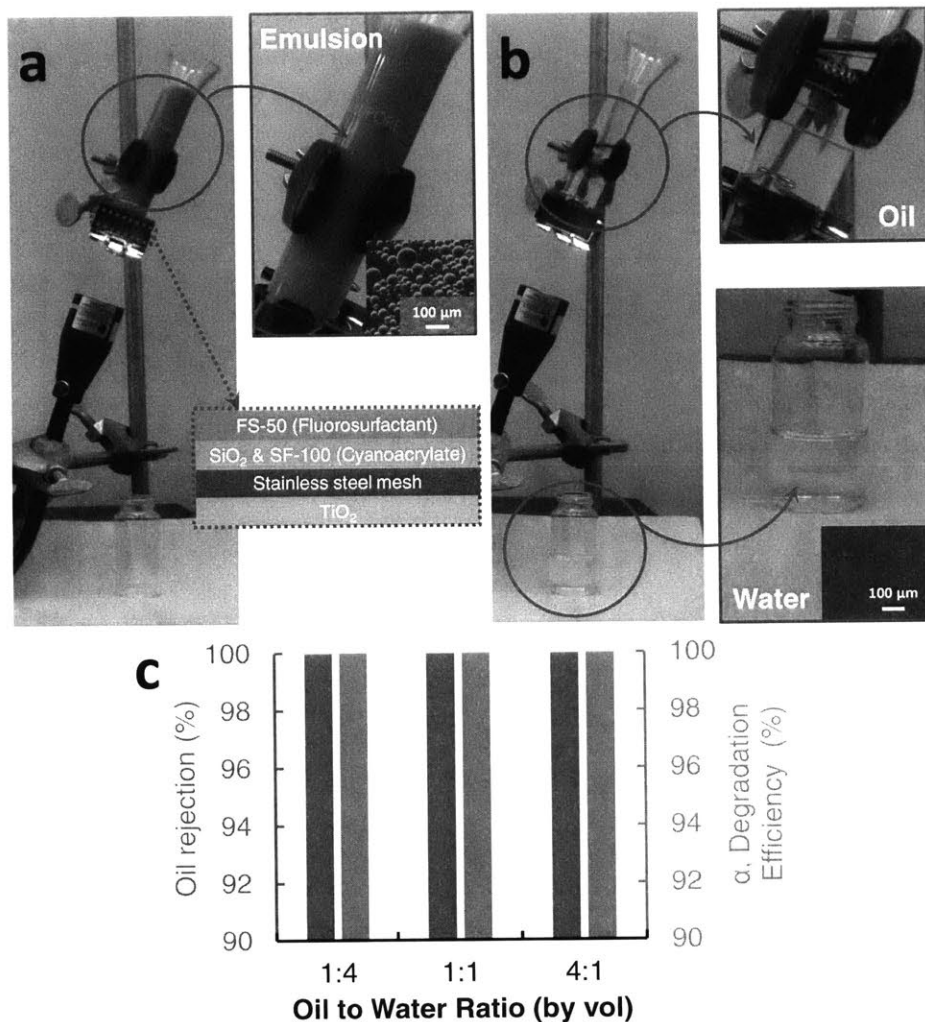
Figure 3-3: Solely gravity-driven separation of surfactant-stabilized oil-water emulsions and simultaneous in-situ degradation of organic pollutant. (a) A photograph of the apparatus for oil-water emulsions separation. Hexadecane-in-water surfactant-stabilized feed emulsion (1:1 by volume) sits above the SSFT membrane. Water is dyed blue (methylene blue dye as an organic pollutant). (b) Organic pollutant-free water is collected as permeate at the bottom of the apparatus while oil is retained. (c) Simultaneous emulsion oil rejection (1:4, 1:1, and 4:1 by volume hexadecane-water surfactant-stabilized feed emulsions respectively, left blue bars) and organic pollutants (MB dye) degradation efficiency (right red bars) of SSFT multifunctional membrane after one pass under $1050 \ mW/cm^2$ UV irradiation intensity.
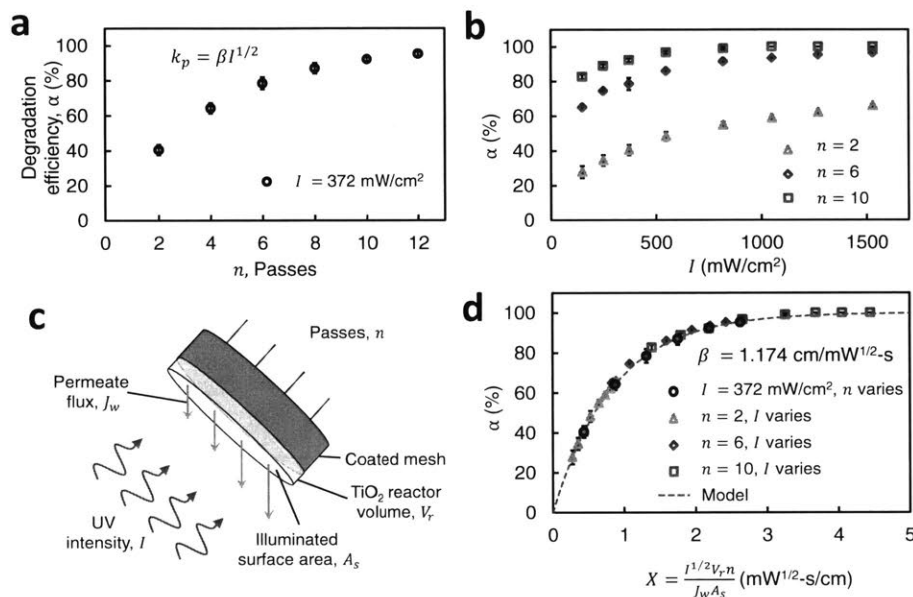
Figure 3-4: Degradation of organic pollutants (MB dye) using a TiO$_2$ coated membrane upon UV illumination. (a) Degradation efficiency α (%) of TiO$_2$ coated membrane as a function of number of passes at constant UV light intensity. (b) Degradation efficiency α of TiO$_2$ coated membrane as a function of UV light intensity at constant number of pass. (c) Schematic illustration of organics degradation system and relevant parameters for degradation model (not to scale). (d) Collapsed plot of degradation efficiency α (%) as a function of X (mW$^{1/2}$-s/cm). Symbols correspond to empirical data while the dashed line corresponds to the degradation model. Model yields very low maximum ($< 4\%$) and mean errors (1.2%). Where error bars (standard deviation of three measurements) cannot be seen, the uncertainty is smaller than the data marker.

eters, we develop a model to describe the trends seen in Fig. 3-4a and Fig. 3-4b. Figure 3-4c shows the degradation system comprised of the coated mesh membrane and permeate coating in addition to parameters which are relevant for the degradation model. The TiO_2 reactor volume refers to the effective volume over the membrane surface area which participates in the photo-degradation process when excited by UV (See Supplementary Fig. B-8). Equation 3.1 gives the expression for degradation efficiency (see Supplementary Sec. B.1 for derivation details):

$$\alpha = 1 - \exp\left(\frac{-\beta I^{1/2} V_r n}{J_w A_s}\right) = 1 - \exp\left(-\beta X\right) \tag{3.1}$$

where I is the intensity of the UV illumination (mW/cm^2), V_r is the active volume (volume of reactor) of the TiO_2 coating reactor through which the permeate flows (m^3), J_w is the average permeate flux per pass (m/s), A_s is the wetted surface area of the membrane (m^2), n is the number of passes, and X is a variable which encapsulate all system operating parameters. β is the photocatalytic degradation system figure of merit with units of ($cm/mW^{1/2}$-s) and is a function of the choice of photocatalytic surface used, the wavelength of the UV source, the type of reactor, the type of organic pollutant present in the water phase, and the turbidity of the feed solution. Equation 3.1 shows that a higher value of β results in greater degradation efficiency for fixed X. Our figure of merit can be used by other researchers for photocatalytic purification in both batch mode ($n > 1$) and continuous operation ($n = 1$). In our experiments, the intensity was varied from $I = 150$ to 1530 W/cm^2 with up to 12 passes. Our permeate flux was $J_w = 1.12 \times 10^{-3}$ m/s and our reactor volume was estimated to be $V_r = 2.55 \times 10^{-9}$ m^3 (Calculations are detailed in Supplementary Sec. B.2).

A collapsed plot showing degradation efficiency α as a function of X is shown in Fig. 3-4d, where we see that α reaches its maxima ($\sim 100\%$) at a high UV intensity ($I = 1050\,mW/cm^2$) and $n = 10$ passes. Detailed experimental parameter inputs, empirical results, model results, and errors are provided in Supplementary Sec. B.2. Fitting Eq. 3.1 to the data shown in Fig. 3-4d results in $\beta = 1.174$ $cm/mW^{1/2}$-s. For the range of parameters used in our study, the first-order photocatalytic rate constant $k_{app} = \beta I^{1/2}$ varies between 14.38×10^{-3} and 45.93×10^{-3} s^{-1} which is similar in magnitude to values reported in the literature [59,

73]. Across all data, our maximum model error was 3.9% while our mean error was 1.2%. According to our model, at a UV intensity of 1185 mW/cm^2, if we were to retard the flux in our experimental apparatus[3] to 5.56×10^{-3} m/s (200 L/m^2-hr), a typical flux used in the micro- and ultra-filtration industry [36], a 4-log reduction ($\alpha > 99.99\%$) in organic contaminants can be achieved with only 1 pass or continuous flow.

According to Eq. 3.1, a factor of 10 reduction in flux results in greatly enhanced organic degradation performance as can be seen in Fig. 3-3d, where all emulsions achieve nearly 100% degradation efficiency. Using the mean flux values given above for each emulsion along with the intensity used during emulsion separation, the number of passes, and the TiO$_2$ coating excitation volume, our values for X were 7.79, 11.56, and 24.65 mW$^{1/2}$-s/cm for the 1:4, 1:1, and 4:1 emulsions, respectively. Using these values of X, the β value corresponding to our system, and Eq. 3.1, our model correctly predicts absolute 100% degradation efficiencies.

3.4 Conclusions

In summary, we have successfully developed and demonstrated the first single-step multi-functional membrane with in-air selective wettability (oil is retained) and photocatalytic properties. Our fabricated membrane is highly robust and easy to manufacture. It uses two distinct coatings on one porous mesh to simultaneously separate oil and water via gravity and purify permeate in-situ with ultraviolet radiation. Because a separate coating is used for degradation which does not participate in oil-water separation, our membrane provides flexibility in the choice of photocatalyst based on the pollutants present in the water phase and the wavelength of the radiation source. Our multifunctional membranes demonstrated excellent oil rejection with bulk oil-water mixtures and oil-in-water and water-in-oil sur-factant stabilized emulsions in addition to simultaneous organics degradation (using MB dye as a model contaminant). We presented an accurate analytical model (mean error = 1.2%) to predict the organic degradation performance of the permeate-side coating (TiO$_2$)

---

[3]We can retard the flux by introducing the oil-water mix at a lower desired flow rate, using a feed solution with a greater viscosity, using a mesh with smaller pore sizes, or by implementing a porous plug above the membrane to increase the hydraulic resistance to flow.

of our multifunctional membrane for batch and continuous flow systems. We defined a figure of merit, β with units of cm/mW$^{1/2}$-s, which can be used to compare degradation performance between photocatalytic systems by other researchers. We expect that our single-step multifunctional membranes could be used for effective separation of oily wastewaters and simultaneous degradation of organic pollutants, showing great potential for oil-water separation and simultaneous treatment of hazardous pollutants from wastewater at an industrial level.

Acknowledgments

Chapter 4

On the limitations of in-air superhydrophilic/oleophobic membranes for oil-water emulsion separation

Chapter abstract

Novel surfaces which are simultaneously hydrophilic and oleophobic (HL/OB) in air are of emerging interest for oil/water separation applications. In this work, we determine the anti-oil fouling potential of in-air superhydrophilic/oleophobic microfiltration membranes vs. in-air superomniphilic (superphilic to water and oil) membranes. This is the first study to isolate the effects of in-air oleophobicity on membrane fouling performance by maintaining in-air hydrophilicity constant between experiments. We present theory for anti-oil fouling membranes and discuss all known mechanisms which endow a surface with HL/OB properties including surface reconstruction by mobile perfluoroalkyl chains. Cellulose membranes are functionalized with perfluoroalykl chains using silane chemistry and characterized with scanning electron microscopy, atomic force microscopy, x-ray photoelectron spectroscopy, and goniometry. Coated and uncoated membranes are fouled with surfactant-stabilized and surfactant-free oil-in-water emulsions and flux decline and flux recovery after cleaning are quantified. We find that despite excellent oil repellency in air, coated and uncoated membranes exhibit the same underwater advancing and receding oil contact angles due to surface reconstruction. During fouling tests, we also find no discernible difference in flux decline or recovery between coated and uncoated membranes. Given observed results, we conclude that in-air HL/OB membranes which rely on surface reconstruction for their unique

in-air wettability do not boost anti-fouling performance underwater. Finally, we discuss future research directions for the development of anti-fouling membranes using fluorinated moieties.

4.1 Introduction

Effective separation of oil-water (O/W) emulsions is a growing field of research and is important for treating oily wastewater from a variety of industries including oil & gas, metalworking, and food production. Membranes are typically preferred for oily wastewater treatment over chemical methods, hydrocyclones, and dissolved air flotation due to their low cost, ease of use, and their ability to separate fine emulsified droplets of oil (droplet diameter $d < 10$ μm) [4, 35, 36, 74]. Oily wastewaters in particular, however, are difficult to treat with membranes due to their tendency to severely foul membrane surfaces during operation [2, 19–22]. An oily wastewater of emerging concern is produced water, a byproduct of hydraulic fracturing. These wastewaters can contain up to 1500 mg/L of total organic carbon and up to 60 mg/L of oil/grease [5]. Much of this oil is in an emulsified form with average oil droplet diameters around 1 μm [75].

To mitigate the effects of membrane fouling from oil and other organics present in feed streams, the academic literature has focused intensely on the fabrication of anti-fouling membranes via surface modification for reverse osmosis and micro-, ultra-, and nanofiltration membranes [23–25]. The vast majority of surface modification literature has focused on increasing membrane hydrophilicity in order to prevent foulant attachment. A hydrophilic surface is one which has a low apparent water contact angle on a substrate in an air environment ($\theta_{wa}^* < 90°$) and prevents foulant attachment underwater due to steric repulsion through the formation of a hydration layer [76]. Surfaces are typically made more hydrophilic by surface grafting/deposition of polymer brushes or thin films which contain long-chain hydrophilic materials such as polyethylene glycol (PEG) [23] or zwitterionic polymers [25].

Recently, surfaces were reported which show simultaneous in-air hydrophilicity and oleophobicity (high apparent oil contact angle, $\theta_{oa}^* > 90°$) [26–31]. While some works did not display surfaces with in-air oil contact angles greater than 90°, they have still demon-

strated surfaces where $\theta_{oa}^* > \theta_{wa}^*$ [33, 34, 68, 77]. In this work, we seek to determine whether in-air hydrophilic/oleophobic membranes can outperform conventional in-air hydrophilic/oleophilic membranes during oil-in-water emulsion separation.

Each previous study has achieved in-air hydrophilicity/oleophobicity by combining two elements: a fluorinated component to function as an omniphobic moiety with a hydrophilic moiety and/or substrate to attract water. Some authors add nanoparticles or surface texturing to enhance roughness and thereby magnify wetting behavior according to classical Wenzel and Cassie-Baxter wetting states [66, 78]. These polymers can be coated onto porous substrates by dip-coating, spin-coating, spray-coating, grafting, layer-by-layer deposition, or chemical vapor deposition. Porous substrates can include woven metal meshes or fabrics. Some in-air hydrophilic/oleophobic surfaces were fabricated by phase inversion [33]. Many of these surfaces have been used for separation of oil-water bulk mixtures and dispersions in addition to surfactant stabilized oil-in-water emulsions[1] by trans-membrane pressures from gravitational and hydraulic head [26, 27, 29, 30, 32–34].

4.1.1 Mechanisms for in-air hydrophilicity/oleophobicity

Two reported mechanisms are responsible for endowing a surface with in-air hydrophilic and oleophobic wettability. The first is surface reconstruction of mobile perfluoroalkyl (PFA) chains in the presence of water [26, 27, 29, 30, 68, 81]. Sawada et al. were one of the first to create in-air hydrophilic/oleophobic surfaces using a morpholino group as a hydrophilic moiety and coupling them to a fluoroalkylated omniphobic tail. The functional group was a trimethoxyvinylsilane and once functionalized onto a surface, these flip-flop type silane coupling agents allowed for slow water wetting and oil (dodecane, $\gamma_{LV} = 25.4$) non-wetting. Kota et al. used fluorodecyl polyhedral oligomeric silsesquioxane (f-POSS) cross-linked with polyethylene glycol diacrylate (PEGDA) [26]; Yang et al. used a complex of sodium perfluorooctanoic acid (PFOA) and poly(diallyldimethylammonium chloride) (PDDA) and chitosan [30, 81]; Pan et al. used a sparse deposition of fluorinated silane on cellulose sub-

---

[1]Surfaces have also been reported which are in-air superoleophilic and superhydrophobic which can be used to pass oil and retain water during separation [79, 80]. We will not focus on these surfaces, however, as much of the industrial oily wastewater requiring treatment has a much greater volume fraction of water than oil [2, 5, 10, 11] and therefore it is more effective to pass water through the membranes.

strates [29]; and Brown and Bhushan used a layer-by-layer spray coating of fluorosurfactant (FS-50) and PDDA as the omniphobic and hydrophilic moieties [53], respectively. Authors claim that reconstruction of mobile PFA chains allow for water wetting and oil non-wetting behavior. It would seem that water, and not oil, wets these surfaces because of water's polarity [29] which may interact with polar CF_3 groups to aid in surface reconstruction. The PFA chains used in these studies were long chains and had at least 8 fluorinated carbon atoms ($[CF_2]_{y-1}CF_3$ where $y \geq 8$).

Surface reconstruction in the presence of certain liquids has been explored in the literature [82, 83]. Honda et al. showed that for saturated surfaces where the intermolecular distance between PFA chains is very small, long PFA chains ($y \geq 8$) remain crystalline when in the presence of water on spin-coated fluoroalkyl acrylate thin films which makes these surfaces hydrophobic. Despite the fact that the studied surfaces were saturated with PFA chains, shorter PFA chains reconstructed in the presence of water, exposing the carbonyl groups which laid below the PFA chain [82]. As further evidence of surface reconstruction, Honda et al. showed that surfaces with shorter PFA chains exhibited strong CF_3 and CF_2 bond presence in air using x-ray photoelectron spectroscopy. After wetting these surfaces in water, however, the hydrated surfaces showed no CF_3 or CF_2 bonds.

One may deduce, therefore, that in-air hydrophilic/oleophobic surfaces with long PFA chains are able reconstruct in the presence of water and not oil due the sparse packing density of PFA chains. We also may expect that once in a hydrated state, CF_3 and CF_2 groups may not be exposed due to surface reconstruction.

The second observed mechanism for in-air hydrophilicity/oleophobicity is kinetic wetting [84]. In this case, water and oil both slowly penetrate 'pores' created and eventually wet coated surfaces after long times. Because water molecules are smaller than oil molecules, however, they are able to more quickly penetrate 'pores', resulting in an in-air hydrophilic/oleophobic surface. While membranes by Zhu et al. may take advantage of this mechanism [33], the majority of membranes in the literature rely on surface reconstruction. We therefore considered surface reconstructing membranes in the present work.

4.1.2   Advantages of in-air hydrophilic/oleophobic membranes

The literature has claimed four distinct advantages for in-air hydrophilic/olephobic surfaces over simply in-air hydrophilic/oleophilic surfaces. These include (1) in-air self-cleaning without detergents, (2) no water pre-wetting required for oil-water separation, (3) separation of water-in-oil emulsions, and (4) anti-fouling.

(1) Self cleaning is the ability of a surface to repel a liquid so effectively that the liquid carries away surface-bound detritus during its movement along the surface. Numerous works have described self-cleaning HL/OB surfaces in which an oil droplet pinned to the surface of a membrane can be carried away once water is added to the membrane surface in an air environment [30, 32, 77, 85].

(2) In-air hydrophilic/oleophilic membranes require pre-wetting with water before separation of oil-water mixtures. An in-air hydrophilic/oleophobic membrane obviates the need for pre-wetting because oil contacting these membranes does not wet and become imbibed within the surface in an air environment [26, 80].

(3) Separation of water-in-oil emulsions with water passage through membrane pores has also been demonstrated by researchers [26] and is only possible using in-air hydrophilic and oleophobic membranes.

(4) Finally, anti-fouling stemming from the presence of fluorinated moieties has been claimed by several researchers in the literature [26, 32, 33, 86]. Anti-fouling performance can be quantified by reduced flux decline and/or greater flux recovery [26, 33, 86] during oil-water fouling tests and cleaning. It may also be measured by reduced passage of oils through coated membrane surfaces [32].

With the exception of anti-fouling, the above advantages function in an air or oil environment. With regards to advantage (3), many oily wastewaters which require treatment are comprised of oil-in-water emulsions [2, 5, 10, 11]. With regards to advantages (1) and (2), conventional membrane systems are thoroughly pre-wetted by water before any exposure to foulants. These membrane systems remain underwater, unless during air-sparging in certain applications [22], throughout their lifetimes. Therefore, to understand whether in-air hydrophilic/oleophobic membranes outperform conventional in-air hydrophilic/oleophilic

membranes, we test both types of membranes for anti-oil fouling performance.

In this work, we functionalized in-air superhydrophilic/superoleopilic membranes to become in-air superhydrophilic/oleophobic. These membranes owe their unique in-air wettability to surface reconstruction. We characterized membrane surfaces using scanning electron microscopy, atomic force microscopy, x-ray photoelectron spectroscopy. We also measured in-air water and oil and underwater air and oil contact angles to understand how coated membranes function underwater. Due to surface reconstruction, we observed that underwater oil contact angles were identical for coated and uncoated membranes. Finally, we observed that uncoated and coated membranes exhibited very similar flux decline when fouled with surfactant-stabilized hexadecane-in-water emulsions and similar flux recoveries after rinsed with water.

4.2 Anti-fouling and wetting theory

In this section we will show that the anti-fouling performance of a membrane can be inferred from its underwater oil substrate contact angle. We will also show how increasing the in-air contact angle for oil on a substrate can lead to greater underwater oleophobicity.

4.2.1 Work of adhesion for droplet attachment and removal

Consider a substrate submerged in a water environment. If colloidal oil droplets are present in the feed and if the substrate is a membrane which passes water, then oil droplets will be advected towards the membrane surface via a drag force during operation. Eventually an oil droplet may land on the membrane surface, forming a three phase interface between water (w), oil (o), and substrate (s) with an apparent underwater contact angle θ_{ow} as shown in Fig. 4-1a. An anti-fouling membrane is one which would both prevent droplets from attaching to the substrate in the first place and enhance droplet removal from the substrate. To consider these interactions, one could express the work of adhesion W (mJ/m^2) for droplet attachment and removal as a function of three interfacial energies (substrate-oil, γ_{so}; substrate-water, γ_{sw}; and oil-water, γ_{ow}):

$$W_{\text{attachment}} = \gamma_{so} - (\gamma_{sw} + \gamma_{ow}) \tag{4.1}$$

$$W_{\text{removal}} = -W_{\text{attachment}} \tag{4.2}$$

Equation 4.1 is derived by considering the work required to create a substrate-oil interface from a substrate-water and oil-water interface while Eq. 4.2 is derived by considering the work required to create a substrate-water and oil-water interface from a substrate-oil interface. We can relate the three interfacial energies to the contact angle of the droplet on a flat substrate using the Young-Dupré equation:

$$\gamma_{ow} \cos \theta_{ow} = \gamma_{sw} - \gamma_{so} \tag{4.3}$$

where θ is the contact angle on a flat surface. We will now express the work of adhesion for droplet attachment and removal as a function of contact angle. First let us consider that during oil droplet attachment, an oil droplet will advance onto the substrate whereas during droplet removal, a droplet will recede from the substrate. Therefore, $W_{\text{attachment}} = f(\theta_{ow}, A)$ and $W_{\text{removal}} = f(\theta_{ow}, R)$. Substituting Eq. 4.3 into Eqs. 4.1 and 4.2, we obtain the work of adhesion for droplet attachment and removal as a function of the oil-water interfacial energy and the dynamic contact angles of oil on the substrate:

$$W_{\text{attachment}} = -\gamma_{ow}(1 + \cos \theta_{ow, A}) \tag{4.4}$$

$$W_{\text{removal}} = \gamma_{ow}(1 + \cos \theta_{ow, R}) \tag{4.5}$$

Since the work of adhesion is defined as > 0 for work done by the system comprised of the three phases in contact, we can infer that $W_{\text{attachment}} < 0$ because work must be done on the system to prevent oil droplet attachment. Figure 4-1b shows $W_{\text{attachment}}$ and W_{removal} for a range of underwater advancing and receding oil contact angles and the interfacial energy between hexadecane and water $\gamma_{ow} = 52.5$ mJ/m^2. We can see that the work of adhesion for both droplet attachment and removal approach zero as the advancing and receding contact angles approach 180°. Therefore, droplet attachment is minimized and

removal is maximized for an underwater superoleophobic ($\theta_{ow} > 150°$) substrate with very small hysteresis $\Delta\theta_{ow} = \theta_{ow,A} - \theta_{ow,R} \ll 1$. In the presence of surfactant, the interfacial energy between oil and water will decrease, thereby decreasing the work of adhesion for attachment and removal.

Despite the fact that the above framework is developed for flat surfaces and that many conventional membranes are not flat, we can use the above framework to infer which membrane may be more anti-fouling to oil within a water environment by comparing the advancing and receding underwater oil contact angles and given two membranes with a similar surface texture but different surface chemistry.
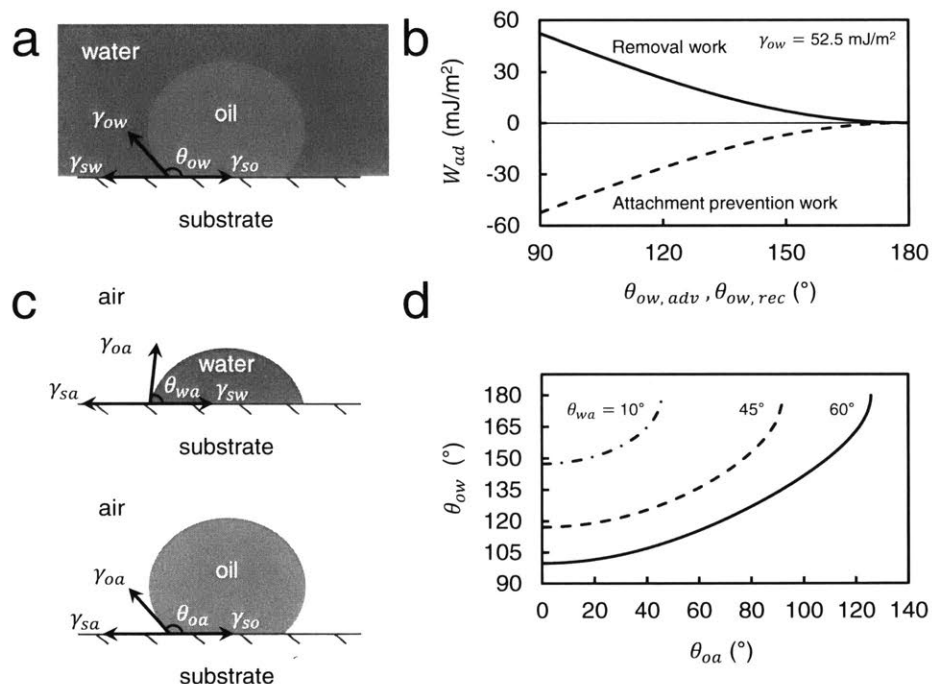
Figure 4-1: Wetting of a substrate by liquids in water and air environments. (a) Drawing of an oil droplet on a substrate in a water environment. (b) Work of adhesion for oil droplet attachment and removal as a function of the advancing and receding contact angles of oil underwater. (c) Drawings of a water and oil droplet on a substrate in an air environment. (d) Underwater oil contact angle as a function of the in-air oil contact angle on a substrate for contours of in-air water contact angle.

4.2.2 Increasing underwater oleophobicity

Here we show that classic wetting theory explains how a substrate which is in-air hydrophilic/oleophobic can improve its underwater oleophobicity for a given hydrophilicity. Following Jung & Bhushan [48], we write the Young-Dupré equation for a water and oil droplet on a substrate in an air environment as shown in Fig. 4-1c:

$$\gamma_{wa} \cos \theta_{wa} = \gamma_{sa} - \gamma_{sw} \tag{4.6}$$

$$\gamma_{oa} \cos \theta_{oa} = \gamma_{sa} - \gamma_{so} \tag{4.7}$$

We can now combine Eqs. 4.3, 4.6, and 4.7 to express the static underwater oil contact angle on a substrate as a function of the static in-air water and oil contact angles in addition to the liquid-liquid and liquid-air interfacial energies:

$$\cos \theta_{ow} = \frac{\gamma_{oa} \cos \theta_{oa} - \gamma_{wa} \cos \theta_{wa}}{\gamma_{ow}} \tag{4.8}$$

Equation 4.8 shows us that for an in-air hydrophilic surface ($\theta_{wa} < 90°$), as the in-air oil contact angle is increased, it is thermodynamically possible for the underwater oil contact angle to increase as well as shown in Fig. 4-1d. We must assume, however, that the surface energies γ_{sa}, γ_{sw}, and γ_{so} do not change from one environment to another. This assumption is violated during surface reconstruction. As we will see in the results section, in-air oleophobicity does not yield greater underwater oleophobicity when surface reconstruction occurs. As a result, only hydrophilicity is required for anti-oil fouling and coated membranes do not outperform uncoated membranes.

4.3 Experimental section

4.3.1 Membranes

Microfiltration membranes used were made of 100% regenerated cellulose with a mean pore size of 0.2 μm (Whatman RC58, General Electric).

4.3.2 Coating preparation and application

The present coating method makes use of a perfluoroalklyl-triethoxysilane monomer shown in Fig. 4-2a. Before coating, many polymer membranes exhibit hydrophilicity and super-oleophilicty as shown in Fig. 4-2b. The triethoxysilane functional group in the fluorosilane monomer reacts with surface-bound hydroxyl (OH^-) groups via a condensation reaction to form a C-O bond and ethanol. Hydroxyl groups are naturally present in cellulose substrates but are enhanced by oxygen plasma treatment (corona treatment) as shown in Fig. 4-2c and d. This reaction bonds a perfluoroalkyl (PFA) chain to the membrane surface. The PFA chain is responsible for endowing a surface with omniphobicity (HB/OB). However, because the polymer substrates used in this study also contain strong hydrophilic moieties, and because the ethoxy functional group has a mild reactivity which limits the graft density of fluorosilane on the substrate surface [29], the coated polymer surface allows polar solvents, such as water, to wet the surface while non-polar solvents, such as oil, bead up on the membrane surface after coating as shown in Fig. 4-2e. A longer length of the PFA chain, determined by y number of carbons in the fluoroalkyl chain (not including the CH_2 spacer group), should increase the water and oil contact angles on the membrane surface [82, 87].

We follow four steps to make polymer membranes simultaneously HL/OB. Plasma treatment at 18 W power for 300 sec in a 13.3 Pa vacuum is first used to create OH^- (hydroxyl) groups on the surface of polymer membranes. Membranes are then placed into a vacuum chamber (Bel-Art) with roughly 5 mL of (Heptadecafluoro-1,1,2,2-tetrahydrodecyl)-triethoxysilane (Gelest) solution at the bottom of the chamber for functionalization in a heated environment. The reaction is allowed to occur for 20 hrs at $20°$, $40°$, $60°$, $80°C$. Coated membranes are submerged in EtOH ($\geq 99.8\%$, Sigma Aldrich) for 5 min and air dried before use to dissolve unreacted silane oligomers.

4.3.3 Membrane surface characterization

Surface visualization and roughness

A field emission scanning electron microscope (FESEM) (Zeiss Supra 55VP) is used to visualize the surface of as received and O_2 plasma treated membranes. We performed this
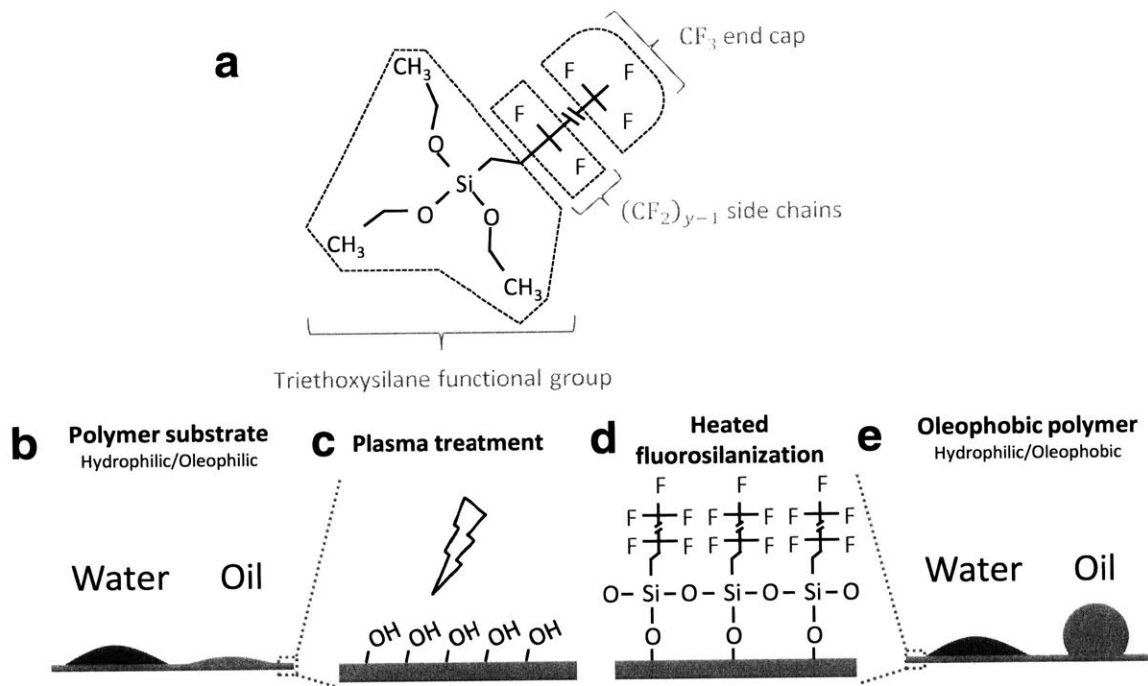
Figure 4-2: Scheme for creating hydrophilic/oleophobic coatings on commercial polymer membranes. (a) Fluorosilane monomer used for surface coating. (b) Typical polymer membranes are ambiphilic to water and oil. (c) Plasma treatment creates hydroxyl groups on polymer surface. (d) Triethoxysilane functional group reacts with hydroxyl groups to bond the PFA chain to the membrane surface. (e) Resulting membrane is in-air hydrophilic/oleophobic.

test to visualize whether plasma treatment significantly altered or damaged the surface of the membranes. Membranes are sputter coated with platinum before imaging to prevent charging and FESEM images are taken at 2.00 kV electron beam potential.

We use atomic force microscopy (AFM) (NX10, Park systems) on a 10×10 μm section of membrane to analyze the roughness of as received and coated membranes. AFM results are used to calculate RMS roughness R_q and Wenzel roughness $r = A_{\mathrm{actual}}/A_{\mathrm{projected}}$ where A is area. Standard deviations are calculated for both parameters by calculating R_q and r at four 5×5 μm locations (NW, NE, SW, and SE).

Surface chemical analysis

We analyze the elemental composition and covalent bond structures of the coated membranes with X-ray photoelectron spectroscopy (XPS) (K-Alpha, Thermo Scientific). We take survey spectra from 0-1350 eV as well as C1s core level spectra for each membrane with XPS using a 0° take-off angle.

Contact angles

We use a goniometer (Model 500-F1, ramé-hart) with an automated dispensing system (100-22, ramé-hart) for measuring in-air contact angles for water ($\gamma_{LV} = 72.5$ mN/m) and hexadecane ($\gamma_{LV} = 27.5$ mN/m) and underwater contact angles for hexadecane and air. Throughout all advancing, static, and receding contact angle measurements, we use less than 7 μL of solvent to ensure that gravity/buoyancy effects are negligible (Bo $\ll$ 1). Static angles are taken by removing the dispensing needle after a drop of water, oil, or air has been dispensed onto the surface and waiting 1 min. We use a standard quartz cell (100-07-50, ramé-hart) with an inverted stainless steel needle for underwater oil and air measurements. For in-air and underwater measurements, averages and standard deviations were calculated from six data points resulting from the left and right contact angles of three runs per phase (water, oil, or air).

4.3.4 Fouling tests

Dead-end and crossflow tests were performed to assess the flux decline and flux recovery of coated vs. uncoated plasma treated membranes. We use O_2 plasma treated membranes as the control rather than uncoated membranes in the case that plasma treatment may slightly alter membrane pore sizes. After plasma treatment, uncoated membranes are not used for at least 1 day in order to allow for OH^- groups to equilibrate.

Dead-end batch tests

Dead-end flow tests were performed in batch mode using a stainless steel stirred cell (HP4750, Sterlitech). Pressure was measured using a pressure gauge (GH-68930-10, Ashcroft) and was supplied to the cell via a nitrogen tank connected to a two-stage gas regulator (Airgas) and an accurate low pressure gas regulator (R-800-3.5, Airtrol) in series. Pressure was mantained at 10 kPa throughout all experiments. Permeate was collected on a digital scale (Ohaus) and its mass was measured as a function of time. The cell has an active membrane area of 14.6 cm^2. Before filtration, both coated and plasma treated membranes were prepared by soaking in EtOH for 5 min and then DI water for 10 min.

Flux as a function of time in LMH (L/m^2-hr) was calculated by a forward finite difference method: $J = \Delta m/(\Delta t \cdot A_m \cdot \rho_p)$ where Δm and Δt are the incremental differences in permeate mass and time, A_m is the membrane area, and ρ_p is the density of permeate which we assume to be that of pure water.

All dead-end fouling tests were comprised of a DI water permeability test, in which 300 mL of DI water was filtered through the membranes; a fouling step, in which the membranes are subjected to concentrated emulsion for 2 hrs to assess flux decline; a cleaning step, where membranes are rinsed once for a 5 sec duration under flowing tap water at 23.0 L/min; and a second permeability test, in which membranes are once again tested with 300 mL of DI water to assess flux recovery. A stirrer at 200 rpm was used during both DI water filtration runs to minimize pore blockage from possible contaminants in the cell. No stirrer was used during the emulsion filtration step to simulate a worst-case scenario.

Flux decline was defined as FD $= 1 - J_{ss}/J_o$ where J_o is the initial flux during the

71

fouling run and J_{ss} is the steady state flux after two hours of fouling. Flux recovery was defined as FR = J_{w2}/J_{w1} where J_{w1} is the average flux during the first DI water filtration step and J_{w2} is the average flux during the DI water filtration step after fouling.

Surfactant-stabilized emulsions for dead-end batch tests were 2500 mg/L oil-in-water with a 10:3 oil to surfactant ratio by weight. They were prepared by adding 1300 μL of hexadecane (99.9%, Sigma Aldrich) and 0.30 g of sodium dodecyl sulfate surfactant (SDS, Sigma Aldrich) to 400 mL of deionized (DI) water and shearing in a blender (Waring) at 22,000 rpm for 3 min. Surfactant-free emulsions were prepared by blending 1300 μL of hexadecane in 400 mL of DI water. Of this mixture, 300 mL was added to the dead end flow cell after the gas-liquid foam resulting from the blending destabilized over roughly 30 min. The remaining 100 mL was saved for analysis. Surfactant concentrations (2.6 mM) were well below the critical micelle concentration of SDS (7-10 mM). Surfactant-stabilized emulsions were visibly stable for at least a 24 hr period and surfactant-free emulsions were visually stable with the exception of a small amount of coalesced oil observed after 2 hrs.

No trend was observed between the permeability of uncoated plasma treated and coated membranes. Average membrane permeability across all membranes, as measured during the first DI water filtration run, was 11485.3 $\pm$ 1084.0 LMH/barg.

Crossflow tests

Crossflow tests were performed using a setup described elsewhere [75] with an additional positive displacement pump (Tuthill) connected to the permeate line. The pump was precisely controlled using a variable frequency drive (Lenze) and a low-flow digital mass flow meter (Bronkhorst). A closed-loop control scheme was implemented which allowed for membranes to be backwashed by clean permeate at a constant flux. For crossflow tests, initial flux was set to $J_o = 100$ LMH before foulant addition. For Triton-X100 emulsion tests, membranes were backwashed for exactly 1 min at $J_b = 200 \pm 5$ LMH after 45 min of fouling. After backwashing, the permeate line was removed from the permeate tank for exactly 80 sec to prevent a spike in flux due to rapid pressure equilibration.

Emulsions for crossflow tests were prepared by adding 11.66 g of hexadecane and 1.17 g of SDS surfactant or 724 μL of nonionic Triton X-100 (Sigma Aldrich) to 500 mL of DI

water and shearing in a blender for 3 min. Of this mixture, 400 mL was added to 9.6 L of DI water in the system feed tank after the gas-liquid foam resulting from the blending destabilized over roughly 30 min. Prepared emulsions were visibly stable for at least a 24 hr period.

Droplet size distributions for dead-end and crossflow emulsions were determined using dynamic light scattering (ZetaSizer, Malvern) and had a log-normal distribution with an average oil droplet diameter of 1 ± 0.1 μm for both surfactant-stabilized and surfactant-free emulsions. These oil droplet sizes are representative of those found in feedwaters from produced water applications [75].

4.3.5 Robustness test

Coated membranes are ensured to be robust underwater by submerging them in a water bath for 5 hrs, drying them in a vacuum, and measuring in-air hexadecane contact angles. No change in contact angle was observed after this test, indicating that membranes were robust for filtration tests.

4.4 Results and discussion

4.4.1 Surface visualization and roughness

Silane grafted PFA chains are deposited on coated membrane surfaces in an extremely thin layer which will not be visually observable. The plasma treatment step, however, may lead to some membrane alteration. To ensure membrane integrity was maintained after plasma treatment, Fig. 4-3 shows FESEM results for uncoated (a) and O_2 plasma treated membranes (b). Both surfaces were porous with a loose network of cellulose fibers and we observed that membrane surfaces were not significantly altered after plasma treatment.

Figure 4-4 shows AFM results for (a) uncoated and (b) coated membranes which underwent PFA deposition at 20 °C. We observed that the coated membrane exhibited a slight decrease in roughness due to plasma treatment. Uncoated membranes had an RMS roughness of $R_q = 217.75 \pm 22.51$ nm and a Wenzel roughness of $r = 1.74 \pm 0.02$. Coated membranes had $R_q = 160.25 \pm 11.67$ nm and $r = 1.41 \pm 0.02$.
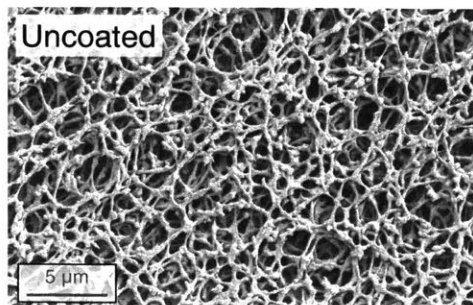
(a) Uncoated membrane
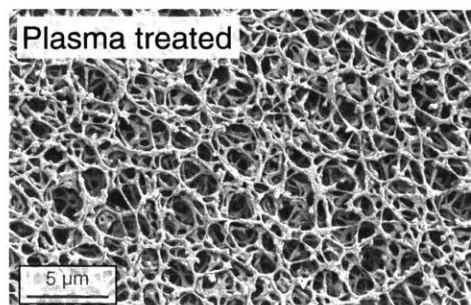
(b) 5 min O$_2$ plasma treated membrane

Figure 4-3: FESEM results for an (a) uncoated and (b) 5 min plasma treated membrane.
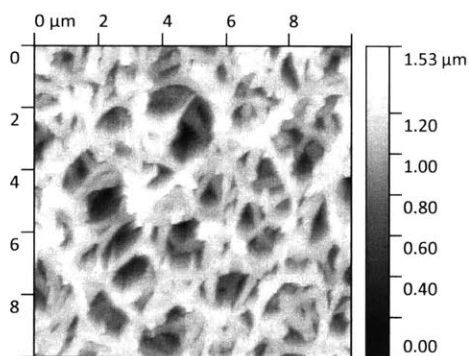
(a) Uncoated membrane
$R_q = 217.75 \pm 22.51$ nm and $r = 1.74 \pm 0.02$
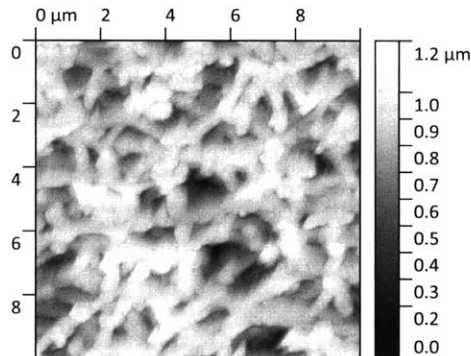
(b) Coated membrane
$R_q = 160.25 \pm 11.67$ nm and $r = 1.41 \pm 0.02$

Figure 4-4: AFM results for (a) Uncoated and (b) 20 °C coated membrane. Root mean square (RMS) roughness R_q and Wenzel roughness r are given for each substrate surface.

4.4.2 Surface chemical analysis

XPS results are shown in Fig. 4-5. Before coating, membranes showed strong O1s and C1s peaks indicative of the cellulose chemical structure as shown in Fig. 4-5a. Coated membrane surfaces showed significant F1s peaks, indicating the coating technique was successful. We observed that an increase in PFA deposition temperature increased F1s peaks as evident between the 20 °C and 80 °C coated membrane spectra. The C1s core level spectra resolving results for the uncoated and 20 °C and 80 °C coated membranes are shown in Fig. 4-5b. We clearly observed a presence of CF_3 and CF_2 bonds in coated membranes which comprise the PFA chain. As expected, these peaks are more present in the 80 °C coated membrane than the 20 °C membrane. We attribute this increase in CF_3 and CF_2 to an increase in PFA graft density (PFA chains/nm^2). From here, we used deposition temperature as a proxy for PFA graft density.

(a) Survey scan	(b) C1s scan
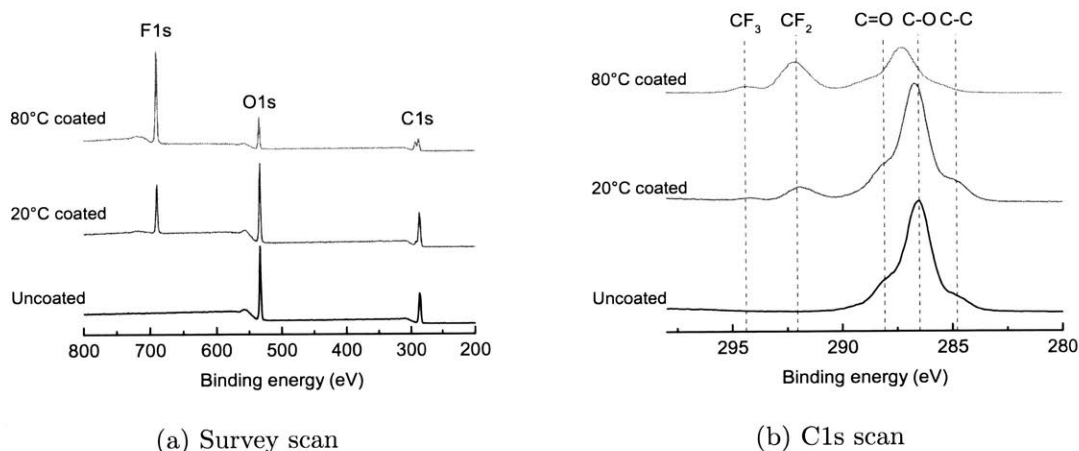
Figure 4-5: XPS survey scan for (a) uncoated vs. 20 °C and 80 °C coated membranes. (b) C1s core level spectra resolving results for uncoated vs. 20 °C and 80 °C membranes.

4.4.3 Contact angles

The increase in PFA chain graft density resulting from increasing deposition temperature also affected surface wetting behavior. Figure 4-6 shows that an increase in deposition temperature resulted in an increase in advancing water contact angle in an air environment. Advancing hexadecane contact angles increased slightly from ~ 120° with deposition

75

temperature. Although not shown, water fully wets the 20°, 40°, 60°, 80 °C coated membranes due to surface reconstruction, although time of wetting increases with deposition temperature.
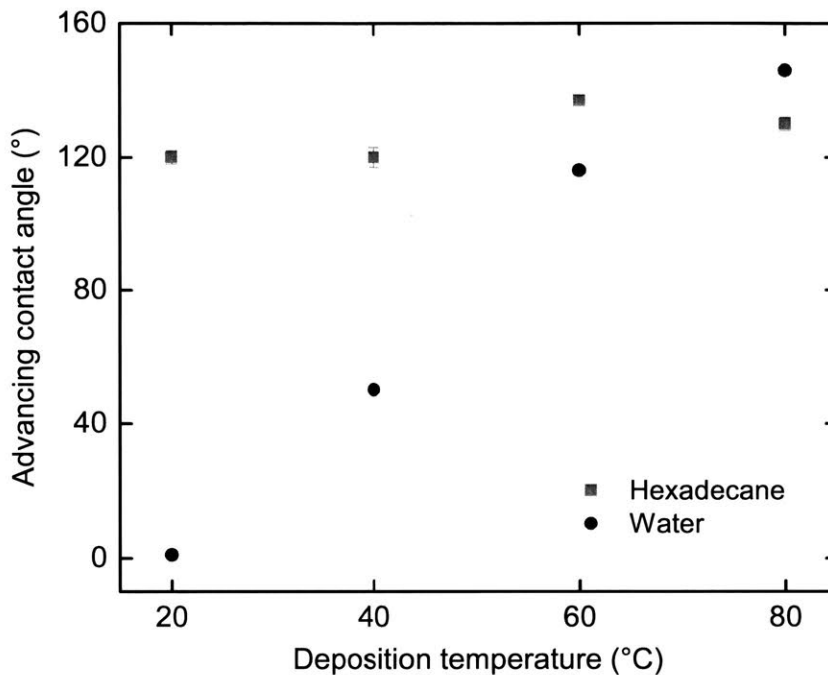
Figure 4-6: In-air advancing contact angles for water and oil (hexadecane) on coated MF membranes.

Figure 4-7 provides surface wetting results for water and hexadecane in air and water environments. Results are given for uncoated, 20 °C coated, and 80 °C coated membranes. From the in-air static contact angle results, we observed that uncoated membranes were omniphilic, 20 °C coated membranes were superhydrophilic and oleophobic, and 80 °C coated membranes exhibited high water and oil contact angles after solvent deposition.

In air environments, cellulose membranes wick in water due to their highly porous nature as can be seen in Fig.4-7a. Therefore, underwater static contact angles for air are provided to give a better measure of hydrophilicity. After submerging all membranes in water, their hydrophilicity is maintained as is evidenced by the nearly identical underwater air contact angles.

Oil contact angles for uncoated vs. coated membranes, despite being drastically different in air, were nearly identical under water. This is due to surface reconstruction. Remember that, given enough time, water is able to wet 20 °C-80 °C coated membranes in air due to the high mobility of PFA chains. When membranes are submerged in water, the same surface reconstruction occurs so that when oil is placed onto the membrane with a reconstructed surface, the oil appears to see no fluorinated groups which may have contributed to an increase in oil contact angle. We also noted an extremely low hysteresis for underwater oil contact angles. This is due to the extreme hydrophilicity of cellulose membranes stemming from its numerous hydroxyl groups.

Note that at such high underwater contact angles ($> 150°$), the goniometer begins to lack resolution to distinguish between angles. Therefore, we subjected uncoated and coated membranes to emulsion fouling tests to determine whether coated membranes were more anti-fouling than uncoated membranes.

4.4.4 Fouling tests

Figure 4-8 shows results from dead-end batch filtration of SDS-stabilized hexadecane-in-water emulsions using uncoated plasma treated membranes and 20°, 40°, 60°, 80 °C coated membranes. From Fig. 4-8a, we observed that the coating, irrespective of increasing graft density as controlled by deposition temperature, did not lead to significant anti-fouling improvements. Fig. 4-8b shows no trend between coating deposition temperature and either flux decline or recovery. Systematic errors or membrane swelling were responsible for some membranes having a flux recovery of greater than 100%. Along with the lack of improvement in underwater oil contact angles shown in Fig. 4-7, Fig. 4-8a and Fig. 4-8b are further evidence that surface reconstruction underwater does not improve flux decline or flux recovery performance.

An argument could be made that without a stirrer during fouling tests, flux decline may have predominantly been due to a buildup of a gel layer on the membrane surface [36, 72] which would have formed regardless of membrane surface chemistry. While dead-end batch filtration tests without stirring have been used in other studies to determine improvements in flux decline performance after membrane surface modification [32], we also subject uncoated

In-air water CA	In-air oil CA	Underwater air CA	Underwater oil CA

a

b

c

d

$\theta^* = 0°$ $\theta^* = 0°$ $\theta^* = 19 \pm 0°$

$\theta_A^* = 166 \pm 7°$
$\Delta\theta^* = 0 \pm 1°$

e

f

g

h

$\theta^* = 0°$ $\theta^* = 116 \pm 2°$ $\theta^* = 13 \pm 5°$

$\theta_A^* = 165 \pm 0°$
$\Delta\theta^* = 0 \pm 0°$

i

j

k

l

$\theta^* = 127 \pm 6°$ $\theta^* = 124 \pm 3°$ $\theta^* = 14 \pm 1°$

$\theta_A^* = 166 \pm 0°$
$\Delta\theta^* = 1 \pm 2°$
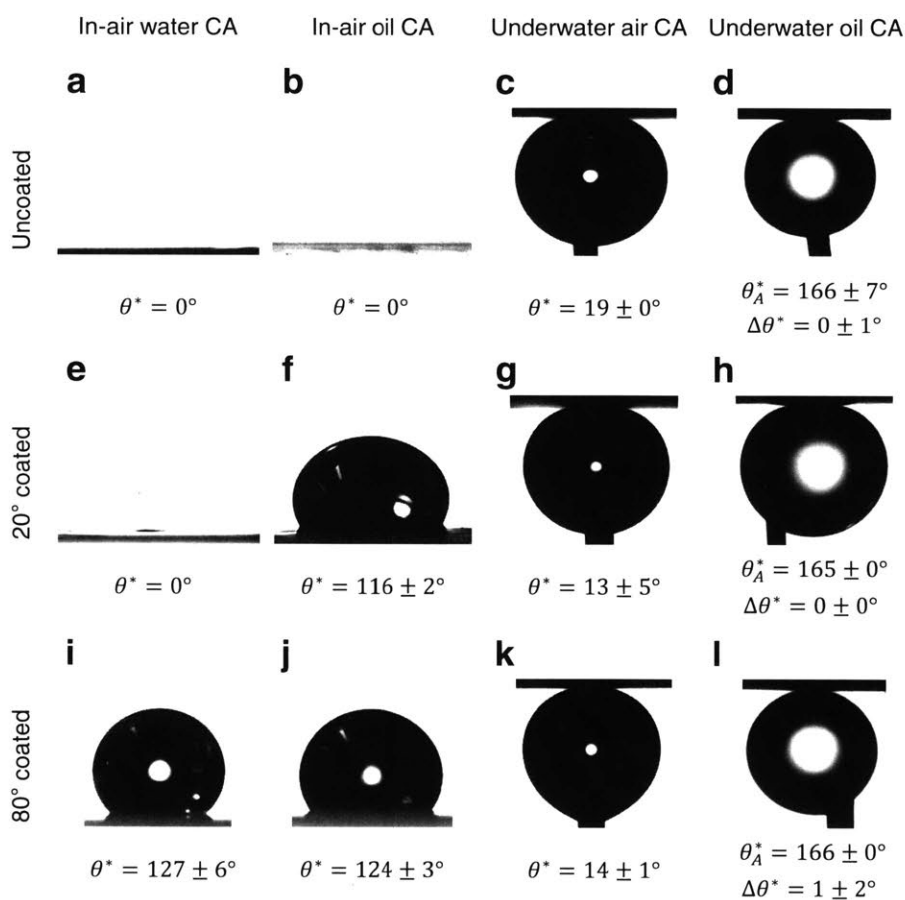
Figure 4-7: Contact angles for water, oil (hexadecane), and air on uncoated membranes (a)-(d), 20° coated membranes (e)-(h), and 80° coated membranes in an air and water environment. (d), (h), and (l) give the underwater advancing contact angle (θ_A^*) and hysteresis ($\Delta\theta^*$) for oil on uncoated and 20 °C and 80 °C coated membranes.

78

plasma treated and coated membranes to crossflow emulsion fouling.

(a) Dead-end batch filtration

(b) Flux decline and flux recovery
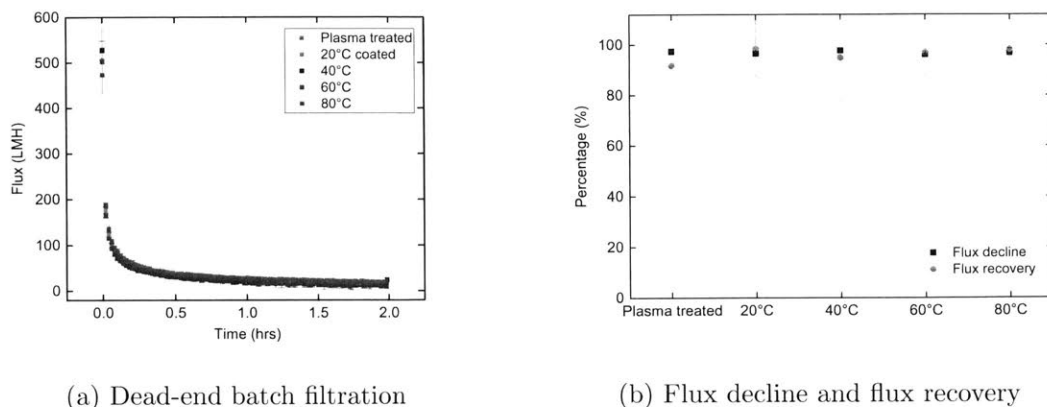
Figure 4-8: Dead-end batch filtration of SDS-stabilized hexadecane-in-water emulsions for uncoated plasma treated and coated (20°, 40°, 60°, and 80 °C) membranes. (a) Flux vs. time plots (b) Flux decline and flux recovery. Error bars in (a) and (b) are standard deviation from two tests for each membrane.

Figure 4-9 shows flux vs. time results for crossflow filtration of uncoated plasma treated and coated membranes using an SDS-stabilized (Fig. 4-9a) and Triton X-100-stabilized (Fig. 4-9b) oil-in-water emulsion. We again observed no difference in flux decline or recovery (in the case of Fig. 4-9b) during crossflow experiments.

Given observed results from underwater oil contact angle measurements, dead-end batch experiments, and crossflow filtration experiments, we surmise that hydrophilic/oleophobic membranes which rely on surface reconstruction for their unique wettability in air environments have no special application in water environments for oil/water separation.

4.5   Implications and directions for future research

Given our observed results, we recommend that future research on anti-fouling reverse osmosis membranes continue to focus on improving in-air hydrophilicity and underwater oleophobicity for mitigating the effects of oil fouling during desalination of oily wastewaters. If fluorinated moieties, such as PFA chains, are to be used for mitigating fouling we believe that they should not be allowed to dynamically reconstruct as they do in the present coating. This can be achieved by securing the PFA chain within a monolith in combination with
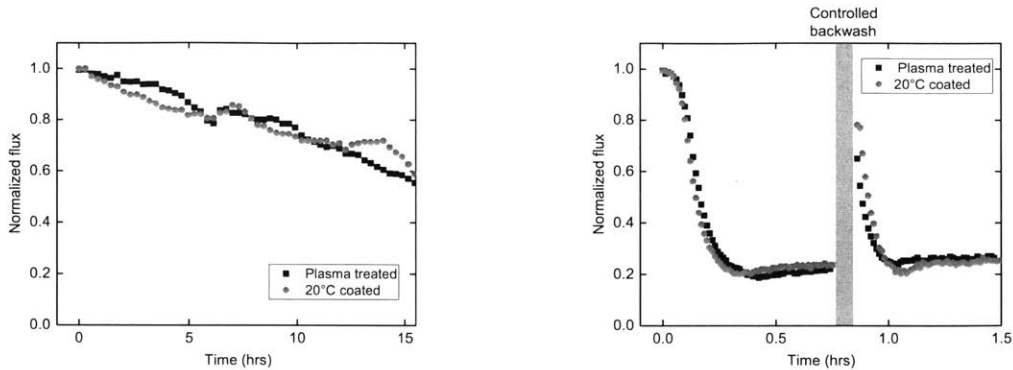
(a) Crossflow filtration of SDS-stabilized emulsion (b) Crossflow filtration of Triton-X100 stabilized emulsion with constant flux backwash

Figure 4-9: Crossflow filtration of SDS and Triton X-100-stabilized hexadecane-in-water emulsions for uncoated plasma treated and 20 °C coated membranes. (a) SDS-stabilized emulsion (b) Triton X-100-stabilized emulsion

hydrophilic moieties to create a so-called amphiphilic membrane via phase inversion [33] or phase inversion with "forced surface segregation" [88]. Amphiphilic surfaces fabricated via initiated chemical vapor deposition which have been shown to reduce biofouling by hindering protein adsorption [89] could also potentially be used to prevent PFA chain mobility in order to mitigate oil fouling.

Finally, we recommend that researchers present the underwater oil contact angles of coated and uncoated membranes, where possible, in future works investigating the potential of in-air HL/OB membranes to prevent fouling.

4.6 Conclusions

In this work, we have prepared and characterized in-air superhydrophilic and oleophobic cellulose membranes. For the first time, we have subjected in-air coated membranes to realistic fouling conditions representative of conventional oil/water separation applications. This is the first study to isolate the effects of in-air oleophobicity on membrane fouling performance by maintaining in-air hydrophilicity and roughness as constant between experiments. We present theory for anti-oil fouling membranes and discuss all known mechanisms which endow a surface with HL/OB properties including surface reconstruction by mobile

perfluoroalkyl chains.

Our major findings are below:

- Anti-oil fouling membranes should have high underwater oil contact angles to prevent droplet attachment and aid in droplet removal.

- It is theoretically possible for a surface to experience an increase in underwater oil contact angle with increasing in-air oil contact angles for a given in-air hydrophilicity. These ideal surfaces, however, must retain their chemical nature underwater.

- Fluorosilane coated membranes in this work are in-air hydrophilic and oleophobic due to reconstruction of mobile PFA chains in the presence of water. Their chemical nature is not maintained underwater, however, as determined by identical underwater oil contact angles for uncoated and coated membranes.

- No discernible difference is observed in flux decline or recovery for uncoated vs. coated membranes due to reconstruction.

Given our observed results, we conclude that simultaneously in-air hydrophilic and oleophobic membranes which rely on surface reconstruction by mobile perfluoroalkyl chains for their unique in-air wettability do not experience an improvement in anti-oil fouling performance during underwater oil/water separation.

Acknowledgments

Chapter 5

In-air hydrophilic and oleophobic reverse osmosis membranes

Chapter abstract

Today's polymer membranes are cheap and effective at desalinating saline water streams via reverse osmosis (RO) or separating oil and solids from wastewater streams via ultra/microfiltration (UF and MF). For desalination of oily wastewater streams, however, these polymer materials suffer from degradation by suspended oil particles over time, adding maintenance and membrane replacement costs for plant operators. RO membranes are perhaps the most oil intolerant of all membranes, with some membrane manufacturers recommending a remarkably low 0.1 mg/L minimum oil content in feed waters. Here we explore a method for coating RO membranes to become in-air hydrophilic/oleophobic without affecting their permeability or salt passage using a perfluoroalkyl-silane chemistry. Fabrication steps are detailed and optimized to produce an RO membrane with the highest in-air oil contact angle and lowest water contact angle. Optimized coated and uncoated membranes were characterized by X-ray photoelectron spectroscopy, attenuated total reflectance-Fourier transform infrared spectroscopy, atomic force microscopy, and by measuring in-air and underwater oil contact angles. The coatings required the membranes to undergo some oxygen plasma treatment which increased their roughness. Filtration tests using surfactant stabilized and surfactant-free oil-in-water emulsions were performed on the optimized coated membranes using as received RO membranes as a control. The coated membranes saw little to no improvement in flux decline performance but did exhibit a slight increase in flux recovery. These results, however, are likely attributed to the increase in the roughness of the membrane during the coating process rather than the modified surface chemistry of the membranes. Given observed results, we discuss future research directions for the development of anti-fouling RO membranes.

5.1 Introduction

One impediment to using reverse osmosis (RO) membranes to desalinate produced water and other industrial wastewater streams is that RO membranes are highly prone to fouling by oil during operation. Pretreatment processes are therefore crucial for enabling RO membranes to perform reliably over a sustained period without significant maintenance or replacement. By removing remaining oil and other suspended materials prior to the desalination step, pretreatment processes can prevent irreversible damage from oil and particulate fouling. RO membrane manufacturers such as DOW recommend pretreatment when oil and grease contaminate RO feedwaters at levels above 0.1 mg/L [18]. Pretreatment processes are designed to effectively remove both organic and inorganic solids from feed waters such as those going to RO modules. These processes include gravity based separation tanks, media filtration, and membrane-based technologies such as ultra/microfiltration (UF/MF) [37].

Improving the ability of a membrane to separate foulants, such as oil, from water while maintaining high fluxes at low operating pressures has been a major focus of membrane research for decades [23, 25]. It is well-known that the most desirable anti-fouling properties of a membrane are hydrophilicity and low surface roughness [23, 24]. A membrane is hydrophilic if the in-air static contact angle of water is less than $90°$ ($\theta_w^* < 90°$). A lower water contact angle indicates a greater surface affinity to water and results in lesser interactions between the membrane surface and organic foulants.

Only recently has it been shown, however, that simultaneously in-air hydrophilic (HL) and oleophobic (OB) membranes could significantly improve both the anti-fouling properties and post-cleaning flux recovery of polymer membranes [32, 34]. The introduction of in-air oleophobicity while maintaining a surface's hydrophilicity could introduce a new degree of freedom with which to fabricate fouling resistant membranes. A membrane surface is oleophobic if the in-air static contact angle of oil is greater than $90°$. While some HL/OB membrane surfaces in the literature do not exhibit $\theta_o^* > 90°$, they did show in-air oil contact angles greater than that of water [32, 33, 84].

Several authors have fabricated in-air HL/OB membranes via different methods including polymer phase inversion [33], spray-coating [27, 30], spin-coating [26], dip-coating [26,

a

Commercial
RO membrane

Coated
membrane

Water Oil   Water Oil

37° 10°   37° 116°

5 mm

b

Gravity
Filtration   UF   **Uncoated RO**

Oily
Waste →   → Permeate
water

Bulk   Emulsified   Brine
Oil   Oil

Gravity
Filtration   **Coated RO**

Oily
Waste →   → Permeate
water

Bulk   Oily
Oil   Brine
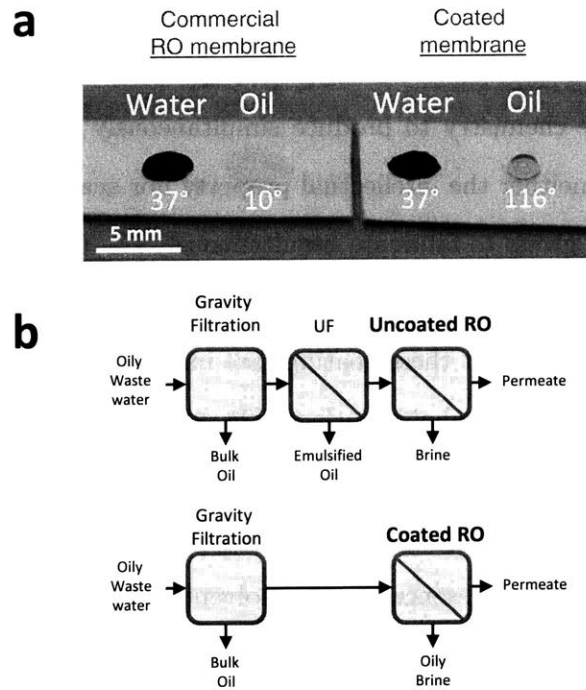
Figure 5-1: Photo and drawing of uncoated and coated reverse osmosis (RO) membranes and their use for oily wastewater filtration and desalination. (a) Static in-air water (dyed with Methylene Blue) and oil (hexadecane, dyed with Oil Red) contact angles on omniphilic as received RO membranes and on coated membranes. (b) For oily wastewater desalination, ultrafiltration (UF) pretreatment is typically required before desalination by RO due to oil sensitivity of the polyamide active layer. The use of coated RO membranes could obviate this pretreatment step.

27, 32], and chemical vapor deposition using silane [29]. All of these fabrication methods were performed on micro- and ultra-filtration membranes with defined pores which were comprised of either a polymer blend, cotton fabrics, glass membranes, or weaved stainless steel meshes.

In this work we present a method, based on chemical vapor deposition of a perfluoroalkylated silane monomer, to make thin film composite reverse osmosis (RO) membranes simultaneously HL and OB. Although silane modification of RO membranes has been demonstrated in the literature [90, 91] for increasing salt rejection and improving chlorine tolerance, using silane chemistry to produce simultaneously HL/OB RO membranes has been demonstrated in neither the intellectual property nor academic literature. To our knowledge, we are the first group to fabricate simultaneously HL/OB RO membranes. It is non-obvious that a fluorosilane coating should allow for HL/OB surfaces because reports in the academic literature suggest that these coatings are instead used for achieving simultaneously hydrophobic (HB) and oleophobic surfaces [28, 92, 93]. We achieve in-air HL/OB by interrupting the chemical deposition process before the surface has reached a saturated graft density. This lower graft density of surface bound perfluoroalkyl (PFA) chains allows for greater chain mobility in the presence of polar solvents. We find the PFA chains crystallize and do not become mobile in the presence of non-polar solvents, allowing water, but not oil, to wet the optimally coated membranes in an air environment.

Our fabrication technique yields RO membranes with high in-air oil contact angles and low water contact angles as shown in Fig. 5-1a. Underwater oil-resistant RO membranes would offer substantial value in the simultaneous filtration and desalination of oily wastewaters. This is because oil-resistant membranes could not only increase RO membrane lifetimes, but also reduce capital and operational expenses by reducing or potentially eliminating RO pretreatment, such as ultra-filtration systems, as shown in Fig. 5-1b.

We show that although the in-air HL/OB wetting behavior of coated RO membranes seems promising, the dynamic nature of the surface grafted PFA chains underwater does not improve their anti-fouling performance during desalination of foulant-contaminated feedwaters. We first characterize coated and as received membrane surfaces to show the coating behavior in-air and underwater. We then provide results for flux decline during desalination

of saline oil-in-water emulsion flux recovery after in-air washing with water. We show that while we found little to no improvement in flux decline, some flux recovery was seen for coated membranes. This was likely due, however, to the surface roughness incurred during plasma treatment. Finally, we provide recommendations for future research on membranes using fluorinated moieties for anti-fouling performance.

5.2 Experimental section

5.2.1 Reverse osmosis membranes

Toray (UTC-82V and UTC-70LF, polyamide) membranes were donated (Toray). DOW (SW30HR, polyamide) membranes were purchased from the manufacturer while Tri-Sep (X201, polyamide-urea) and GE (CE, cellulose acetate) membranes were purchased through a distributor (Sterlitech). All membranes were thin film composite membranes with a different active layer polymer.

5.2.2 Coating preparation and application

The present coating method makes use of a perfluoroalklyl-triethoxysilane monomer shown in Fig. 5-2a. Before coating, many polymer membranes exhibit superoleophilicty and hydrophilicity as shown in Fig. 5-2b. The triethoxysilane functional group in the fluorosilane monomer reacts with surface-bound hydroxyl groups created on the polymer membrane via oxygen plasma treatment (corona treatment) as shown in Fig. 5-2(c-d). This reaction bonds a perfluoroalkyl (PFA) chain to the membrane surface. The PFA chain is responsible for endowing a surface with omniphobicity (HB/OB). However, because the polymer substrates used in this study also contain strong hydrophilic moieties, and because the ethoxy functional group has a mild reactivity which limits the graft density of fluorosilane on the substrate surface [29], the coated polymer surface allows polar solvents, such as water, to wet the surface while non-polar solvents, such as oil, bead up on the membrane surface after coating as shown in Fig. 4-2e. A longer length of the PFA chain, determined by y number of carbons in the fluoroalkyl chain (not including the CH_2 spacer group), should increase the water and oil contact angles on the membrane surface [82, 87].

Figure 5-2: Scheme for creating hydrophilic/oleophobic coatings on commercial polymer membranes. (a) Fluorosilane monomer used for surface coating. (b) Typical polymer membranes are ambiphilic to water and oil. (c) Plasma treatment creates hydroxyl groups on polymer surface. (d) Triethoxysilane functional group reacts with hydroxyl groups to bond the PFA chain to the membrane surface. (e) Resulting membrane is in-air hydrophilic/oleophobic.

Four steps are performed to make polymer membranes simultaneously HL/OB. Plasma treatment at P_{plasma} power for t_{plasma} sec in a 13.3 Pa vacuum is first used to create OH$^-$ (hydroxyl) groups on the surface of polymer membranes. Membranes are then placed into a vacuum chamber (Bel-Art) with roughly 5 mL of (Heptadecafluoro-1,1,2,2-tetrahydrodecyl)-triethoxysilane (Gelest) solution at the bottom of the chamber for functionalization in a heated environment. The reaction is allowed to occur for t_{coat} hours at T_{coat} °C.

In addition to creating hydroxyl groups on the polymer surface, plasma treatment can also physically etch deformations onto the surface of the membrane [94]. For large P_{plasma} and t_{plasma}, the active layer of a polymer membrane can become damaged. We have observed that $P_{\text{plasma}} = 18$ W and $t_{\text{plasma}} = 120$ sec can repeatably and catastrophically damage the surface of RO membranes. Therefore P_{plasma} and t_{plasma} should be low enough to limit damaging by surface etching and high enough that a sufficient number of hydroxyl groups are created on the surface for strong oleophobicity while not compromising membrane function.

The operating conditions used here are listed in Table 5.1.

Table 5.1: Operating conditions for this study.

Parameter	Value
P_{plasma}	6.8 W
t_{plasma}	60 s
T_{coat}	50 °C
t_{coat}	4, 8, 12, 16, 20 hrs
$(\text{CF}_2)_{y-1}$	$y = 8$

5.2.3 Membrane characterization

We use a goniometer (Model 500-F1, ramé-hart) with an automated dispensing system (100-22, ramé-hart) for measuring in-air contact angles for water ($\gamma_{LV} = 72.5$ mN/m) and hexadecane ($\gamma_{LV} = 27.5$ mN/m) and underwater contact angles for hexadecane and air. Throughout all advancing, static, and receding contact angle measurements, we use less than 7 μL of solvent to ensure that gravity/buoyancy effects are negligible (Bo $\ll 1$). We use a standard quartz cell (100-07-50, ramé-hart) with an inverted stainless steel needle for underwater oil and air measurements. In-air contact angles were measured after substrates

were completely submerged in pure ethanol for 5 min and air dried. Underwater contact angles were taken after membranes were fully submerged in ethanol for 5 min and then immediately transferred to a water environment without air drying. This is because we found that air drying membranes after ethanol or water submersion increased their surface roughness.

We analyze the elemental composition and covalent bond structures of the coated membranes with X-ray photoelectron spectroscopy (XPS) and attenuated total reflectance-Fourier transform infrared spectroscopy (ATR-FTIR). We take total surveys as well as carbon elemental analyses for each membrane with XPS (K-Alpha, Thermo Scientific). For ATR-FTIR (Nicole iS 50, Thermo Fisher) we take 256 scan measurements using a germanium crystal and record a background measurement before each membrane spectrum is taken.

We use atomic force microscopy (AFM) on 10×10 μm of membrane to analyze the roughness of as received and coated membranes. AFM (NX10, Park systems) results are used to calculate Wenzel roughness $r = A_{\text{actual}}/A_{\text{projected}}$ where A is area and RMS roughness R_q. Standard deviations are calculated for both parameters by calculating R_q and r at four 5×5 μm locations (NW, NE, SW, and SE).

5.2.4 Fouling tests

The value of an oil fouling-resistant reverse osmosis membrane can be demonstrated by an oil-in-water emulsion fouling test. We used two surfactant stabilized oil-in-water emulsions and an oil-in-water emulsion without surfactant. The surfactant stabilized emulsions were comprised of 1500 mg/L of hexadecane and 150 mg/L of anionic (SDS, sodium dodecyl sulfate) or non-ionic (Tween 80, polyoxyethylenesorbitan monooleate) surfactant (Sigma Aldrich) and 2 g/L aqueous NaCl solution (brackish water) made with sodium chloride (Sigma Aldrich). The oil, surfactant, and brackish water are blended at 22,000 rpm for 5 min using a commercial blender (Waring) to shear the oil droplets to a small mean diameter (~ 1 μm) representative of produced water samples [11]. Emulsions without surfactants contain 1500 mg/L of pure hexadecane with 2 g/L NaCl and are blended in the same way as surfactant stabilized emulsions.

Membranes were tested in batch dead-end mode using a stainless steel stirred cell (HP4750, Sterlitech) using an digital pressure gauge (Ashcroft) and a digital scale (Mettler Toledo) connected to a computer for recording permeate mass over time. The active membrane area in the cell is 14.6 cm^2. Crossflow tests were performed using a custom setup described elsewhere [95]. Each fouling test was performed by first submerging coated and uncoated membranes in ethanol for 5 min to remove unreacted silane oligomers and then water for 10 min to dissolve ethanol from the substrate. Membranes are then made to filter DI water for at least 1 hour until permeate water flux stabilizes. During this step, permeability (L/m^2-hr-bar) is calculated as $A = J/(\Delta P - \Delta \Pi)$ where flux J is the steady state flux achieved towards the end of the test, ΔP is the transmembrane pressure, and $\Delta \Pi$ is the transmembrane osmotic pressure which is equal to zero during filtration of DI water.

Next, a salt passage test is performed on each membrane with 2 g/L aqueous NaCl solution for at least 45 min. Salt passage, defined as SP $= C_{\text{permeate}}/C_{\text{feed}}$, is determined using a conductivity meter on the feed and permeate (Hach). Membranes are then subjected to emulsion fouling for exactly 2 hrs. After emulsion fouling, a cleaning protocol is performed where membranes are subjected to ten rinses of a 5 sec duration each using tap water at 19 L/min in air and the cell is thoroughly rinsed with isopropyl alcohol and DI water. The cleaning protocol is similar to one used in literature [94, 96, 97]. After cleaning, membranes are once again are made to filter 2 g/L aqueous NaCl solution to determine the extent of irreversible fouling. All dead-end tests are performed at 13.8 barg (200 psig) with a magnetic stirbar at 500 rpm. Crossflow tests were performed at 200 psig with a feed velocity of 1.75 cm/s and no feed spacer. The cleaning step in the crossflow tests was comprised of decreasing the feed pressure to zero and increasing the feed flow rate to 8.3 cm/s for 30 min.

5.3 Results and discussion

5.3.1 Membrane characterization

Figure 5-3a shows the in-air static contact angles of oil (hexadecane) and water on a variety of reverse osmosis membrane substrates. To the authors' knowledge, the high oleophobicity on the reverse osmosis substrates shown in Fig. 5-3 has not been demonstrated in the

literature. We tested multiple RO active layer polymer compositions for in-air oleophobicity performance which included three polyamide (PA) membranes, one polyamide-urea (PA-u) membrane, and one cellulose acetate (CA) membrane. To improve the surface graft density of the PFA chains using silane chemistry, a surface should have an abundance of hydroxyl groups either naturally or after plasma treatment [98]. Interestingly, we were able to achieve the highest oil contact angles for polyamide active layers, which are initially devoid of hydroxyl groups and only gain them after oxygen plasma treatment. Furthermore, the CA membrane surface yielded the lowest oleophobicity despite the abundance of hydroxyl groups initially present within the polymer.

In addition to their high oleophobicity, all coated substrates exhibit in-air self-cleaning where oil droplets become displaced and mobile once the substrates are wet with water [27, 30, 32]. This is because coated surfaces more strongly prefer to be wet by water than oil and because the oil droplets are more easily rinsed away by water when they are in a Cassie-Baxter state on membranes which exhibit high oleophobicity (Toray 82V).

From here, we investigate the effect of the present coating on the Toray 82V RO membrane shown in Fig. 5-3a because it exhibits the highest in-air oil contact angle relative to other membranes. Figure 5-3b shows that for the Toray 82V RO membrane, increasing deposition time at $50\,^\circ$C leads to increasing in-air oil contact angles. In-air water contact angles are also seen to increase as deposition time (and also temperature, although not shown here) is increased. This rise in both oil and water contact angles is attributed to the increased surface graft density of PFA chains on the membrane substrate. For higher temperatures ($\sim 70\,^\circ$C), substrates exhibit in-air water and oil contact angles above 100°. The highest in-air oil contact angle and the lowest water contact angle in Fig. 5-3b is provided by the 12 hour deposition time, therefore the results which follow are provided for the Toray 82V membrane with 12 hours of heated chemical vapor deposition at $50\,^\circ$C.

Two mechanisms are responsible for controlling the water wetting and oil non-wetting characteristics of coated membranes. The first is an interaction between polar solvents, the CF_3 end cap on each PFA chain, and the intrinsic hydrophilicity of the substrate which results in surface reconstruction of PFA chains [29]. Surface reconstruction has been shown on surfaces saturated with short PFA chains ($y < 8$) [82, 87]. In the present work, surface
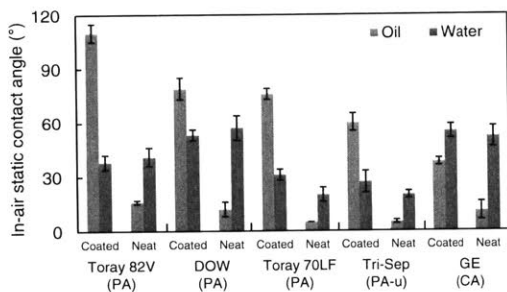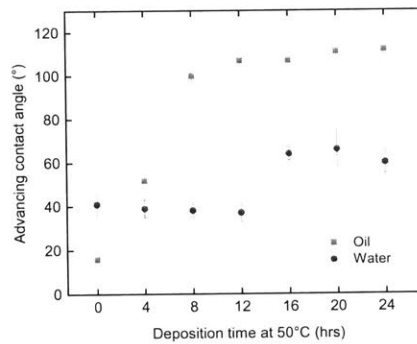
Figure 5-3: In-air contact angle results for coated and uncoated reverse osmosis membranes. (a) In-air water and oil (hexadecane) contact angles for a variety of coated and uncoated (neat) reverse osmosis membranes. Membranes are listed from left-to-right in order of decreasing in-air oil contact angle and all membranes were coated with PFA-silane for 12 hrs at $50\,^{\circ}$C. Active layer compositions were polyamide (PA), polyamide-urea (PA-u), and cellulose acetate (CA). (b) Toray 82V advancing water and oil (hexadecane) contact angles for uncoated (0 hr) and coated RO membrane substrates. O_2 plasma treatment times of 60 sec at 6.3 W of power and coating temperatures of $50\,^{\circ}$C were used for all substrates. Error bars in (a) and (b) are standard deviations of six measurements calculated from the left and right sides of at least three droplets placed on different dry sites on the membrane surface.

reconstruction also occurs for long PFA chains ($y = 8$) because the surfaces are not fully saturated with PFA-silane - allowing them to be mobile when in contact with a polar solvent. The second mechanism involves penetration of solvents through the porous perfluorinated film [84]. Evidence of the first mechanism, surface reconstruction for polar solvents, can be observed with a contact angle test using hexane and 1-hexanol: two solvents of a similar molecular size and composition which have a different polarity. Table 5.2 shows the contact angles on a coated membrane for water, hexadecane, hexane, and 1-hexanol with relevant chemical and physical properties. It is clear that although 1-hexanol and hexane share very similar chemical structure and molecular weight, 1-hexanol wets the surface of the membrane much more than hexane likely because it has a higher dielectric constant.

Table 5.2: Solvent polarity causes chain reconstruction on coated membranes

Properties / Solvent:	Water	Hexadecane	Hexane	1-Hexanol
Structure	H_2O	$CH_3[CH_2]_{14}CH_3$	$CH_3[CH_2]_4CH_3$	$CH_3[CH_2]_5OH$
Mol. Weight (Da)	18.0	226.4	86.2	102.2
Surface tension (mN/m, $20\,^{\circ}C$)	72.8	27.5	18.5	26.3
Dielectric constant at $20\,^{\circ}C$	80.10	2.08	1.88	13.30
In-air static CA ($^{\circ}$)	37 ± 4	116 ± 1	63 ± 5	8 ± 3

Figure 5-4 shows ATR-FTIR results comparing the coated and uncoated membrane surfaces. At 1206 cm^{-1} a peak indicative of a CF_2 bond is clearly observed in the coated, but not the uncoated, membrane spectrum. We find that because of other peaks from the surface chemical structure, the CF_3 peak on the coated membrane is not observable. We use XPS to further confirm the presence of fluorine and especially CF_3 groups on the coated membrane surface.

XPS results are shown in Fig. 5-5. Before plasma treatment and coating, the membrane shows modest presence of carbon, oxygen, and nitrogen as shown in Fig. 5-5a which is indicative of a polyamide active layer. O_2 plasma treatment causes an increase in hydroxyl groups which is evident by the increased presence of oxygen compared to the uncoated membrane. Coated membrane surfaces are shown to have a significant count of fluorine atoms, indicating the coating technique was successful. The C1s core level spectra resolving results for the coated and uncoated membranes shown in Fig. 5-5b clearly show the CF_3 and CF_2 groups which comprise the PFA chain.

Membrane roughness after plasma treatment and fluorosilane deposition is shown in Fig. 5-6. The increase in Wenzel roughness by nearly 30% shown for coated membranes is predominantly incurred during the plasma cleaning step and, to some extent, during air drying after ethanol submersion.

Figure 5-7 shows underwater contact angles for air and oil compared to the in-air contact angles for water and oil. Comparing Fig. 5-7c and g, we can see that the hydrophilicity of the membrane underwater is maintained. Comparing Fig. 5-7d and h, however we observe that the oleophobicity of the membrane is not increased despite having been coated with fluorosilane. This is due to chain reconstruction: the same mechanism which allowed water to penetrate the PFA chains in-air. We will see in the next section that because of PFA chain reconstruction, coated membranes do not perform better than uncoated membranes during fouling.
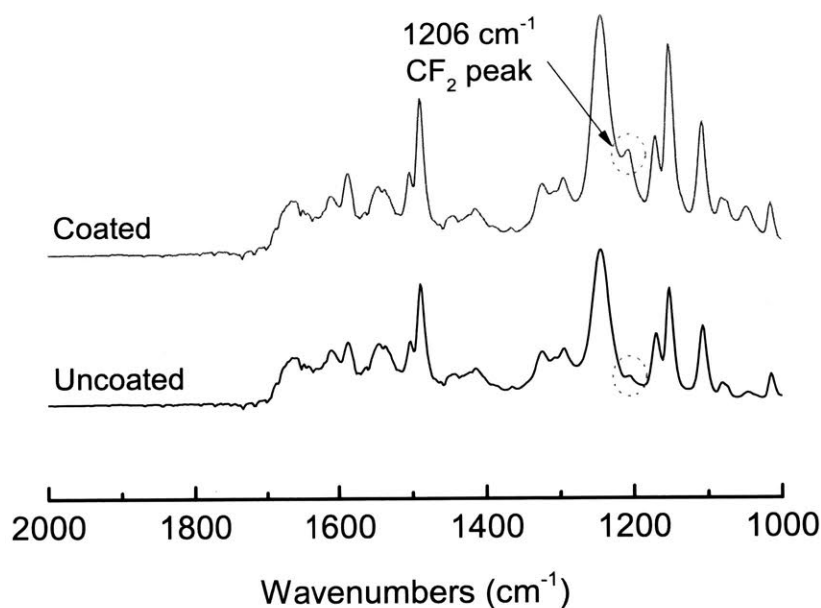
Figure 5-4: ATR-FTIR results for uncoated vs. coated (12 hrs at 50 °C) RO membranes. The 1206 cm^{-1} peak corresponds to the CF$_2$ side chains of the PFA chain. The CF$_3$ peak is difficult to observe because its location overlaps with other peaks from the RO membrane chemical structure.

It is important to note that the unique in-air wettability of coated RO membrane surfaces
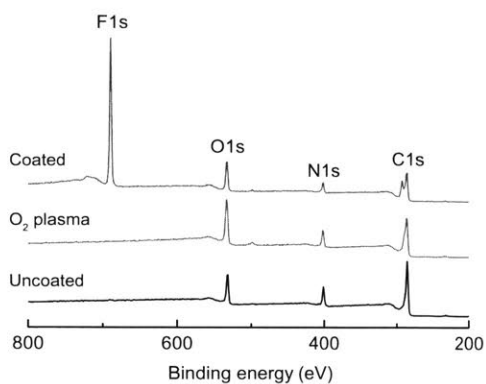
(a) Survey scan
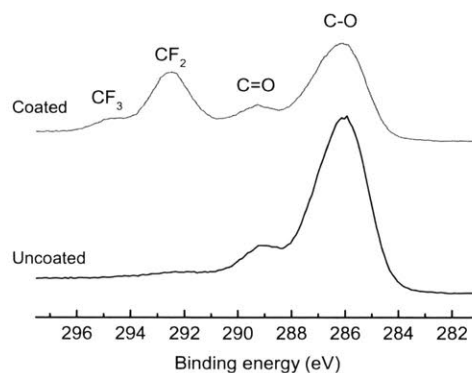
(b) C1s scan

Figure 5-5: XPS survey scan for (a) uncoated, O_2 plasma treated, and coated (12 hrs at $50\,°C$) RO membranes. (b) C1s core level spectra resolving results of coated vs. uncoated membranes.
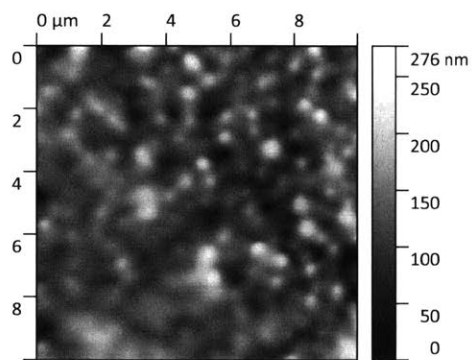
(a) Uncoated membrane
$R_q = 34.20 \pm 5.69$ nm and $r = 1.02 \pm 0.01$
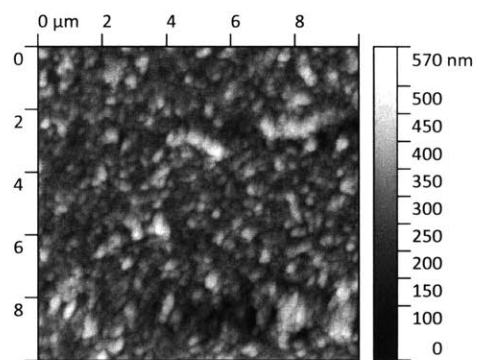
(b) Coated membrane
$R_q = 72.15 \pm 6.90$ nm and $r = 1.29 \pm 0.01$

Figure 5-6: AFM results for (a) uncoated and (b) coated membrane (after 5 min EtOH bath with air drying). Root mean square (RMS) roughness R_q and Wenzel roughness r are given for each substrate surface.

	In-air water CA	In-air oil CA	Underwater air CA	Underwater oil CA
Uncoated	**a** $\theta^* = 41 \pm 5°$	**b** $\theta^* < 10°$	**c** $\theta^* = 28 \pm 2°$	**d** $\theta_A^* = 159 \pm 3°$ $\Delta\theta^* = 4 \pm 2°$
Coated	**e** $\theta^* = 38 \pm 4°$	**f** $\theta^* = 110 \pm 5°$	**g** $\theta^* = 29 \pm 2°$	**h** $\theta_A^* = 155 \pm 4°$ $\Delta\theta^* = 3 \pm 1°$
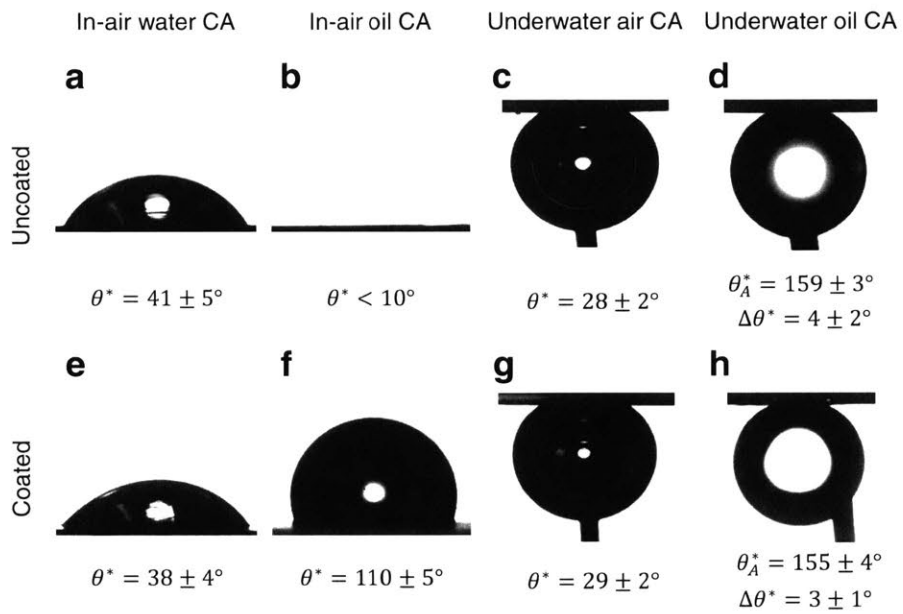
Figure 5-7: Contact angles for oil, water, and air on uncoated membranes (a)-(d) and coated membranes (e)-(h) in an air and water environment. (d) and (h) give the underwater advancing contact angle (θ_A^*) and hysteresis ($\Delta\theta^*$) for oil on the uncoated and coated membrane.

97
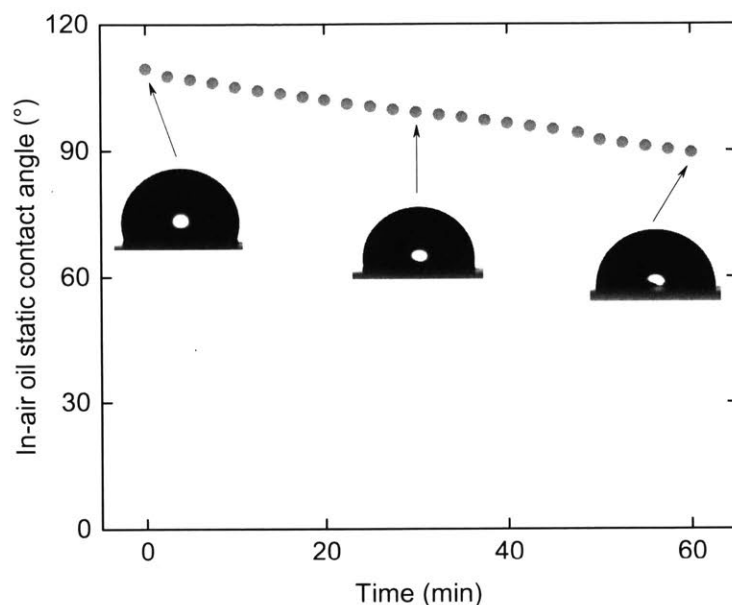
Figure 5-8: Contact angle vs. time for a hexadecane droplet on a coated RO membrane surface indicating low PFA chain graft densities.

in not only due to surface reconstruction, but also time dependent kinetic wicking. This is evident by the decrease in oil contact angle on the surface of coated membranes as a function of time as observed in Fig. 5-8. This decrease is not a result of hexadecane evaporation because hexadecane has a low vapor pressure. Oil stains on the RO membrane active layer accompanied the decrease in oil contact angle, indicating that hemiwicking was occurring. This behavior is most likely due to a lower graft density resulting from the lack of hydroxyl groups in the polyamide layer. In other words, the PFA chain graft density is high enough to be oleophobic but low enough to allow oil to wick through PFA chain 'pores' [84]. This kinetic wicking of oil into the coated RO membrane active layer was also observed for longer coating depositing times (> 12 hrs) and higher temperatures ($> 50\,^{\circ}$C).

5.3.2 Fouling tests

Before fouling the coated membranes, we first determine whether their permeability and salt passage were compromised by the fluorosilane coating. Figure 5-9 shows that the permeability (L/m^2-hr-bar) and salt passage for both coated and uncoated RO membranes

appear unchanged by the coating. This is because the PFA chains which are distributed as a monolayer are very thin ~10 nm and likely "porous" in that the surface graft density has been judiciously maintained low so as to not affect the hydrophilicity. Therefore, they do not provide a significant hydraulic resistance relative to the large resistance of the RO membrane active layer. The salt passage is higher than what is expected for RO membranes due to salt leakage around the O-rings used to seal the membranes in the dead-end flow cell.
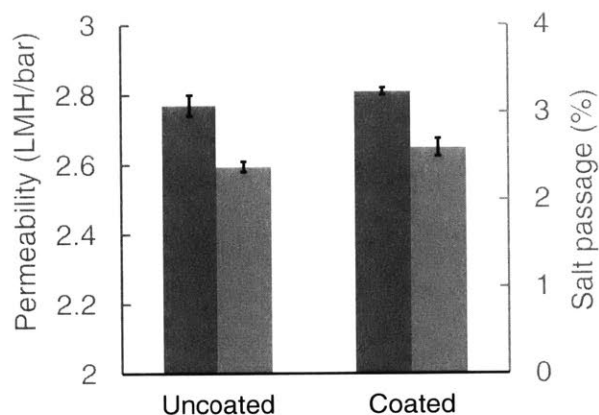
Figure 5-9: Permeability and salt passage of coated and uncoated membranes are maintained after coating. Error bars are standard deviation of at least two permeability and salt passage experiments for each membrane.

Figure 5-10 shows the membrane subjected to surfactant stabilized and surfactant-free emulsions of hexadecane-in-water. Anionic (SDS) and nonionic (Tween 80) surfactants are used as emulsion stabilizers in dead-end flow tests in Fig. 5-10a and Fig. 5-10b while surfactant-free emulsions are used in a dead-end flow test in Fig. 5-10c and a long term cross-flow test in Fig. 5-10d. The most severe fouling in the dead-end flow tests, as measured by the magnitude of steady state flux, was observed in the Tween 80 surfactant stabilized emulsion which is likely due to lower electrostatic repulsion between the membrane surface and surfactant stabilized oil droplets relative to the anionic surfactant (SDS). The least severe fouling was observed in the dead-end flow surfactant-free hexadecane-in-water emulsion and is likely due to flocculation and coalescence of oil droplets at the surface of the membrane followed by re-suspension of oil into the bulk. Most importantly, our results

indicate that the coated membrane had little to no improvement in resisting fouling from both surfactant stabilized and surfactant-free oil-in-water emulsions. While some promising anti-fouling performance is observed in Fig. 5-10b, we attribute this result to a stochastic emulsification process prevalent in non-ionic surfactant stabilized emulsions. We also attribute the observed positive flux recovery results in the dead-end flow tests to increased roughness incurred during plasma cleaning. Future tests should use a plasma treated membrane as a control instead of an as received membrane in order to understand the effect of the surface modification on flux recovery performance.

5.3.3 Implications and directions for future research

Given our observed results, we recommend that future research on anti-fouling reverse osmosis membranes continue to focus on improving in-air hydrophilicity and underwater oleophobicity for mitigating the effects of oil fouling during desalination of oily wastewaters. If fluorinated moieties, such as PFA chains, are to be used for mitigating fouling we believe that they should not be allowed to dynamically reconstruct in the presence of polar liquids as they do in the present coating. This can be achieved by securing the PFA chain within a monolith in combination with hydrophilic moieties to create a so-called amphiphilic membrane via phase inversion [33] or phase inversion with "forced surface segregation" [99]. Amphiphilic surfaces fabricated via initiated chemical vapor deposition which have been shown to reduce biofouling by hindering protein adsorption [89] could also potentially be used to prevent PFA chain mobility in order to mitigate oil fouling.
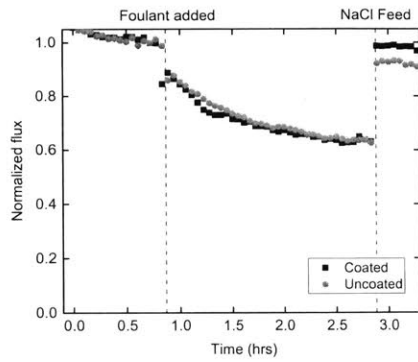
(a) 1500 mg/L SDS stabilized hexadecane-in-water emulsion Dead-end
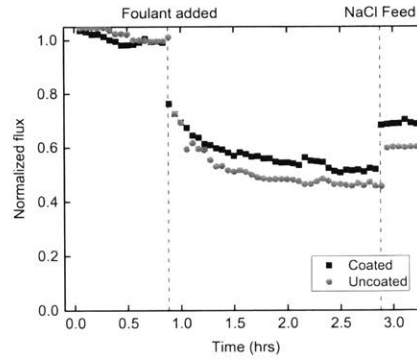
(b) 1500 mg/L Tween 80 stabilized hexadecane-in-water emulsion Dead-end
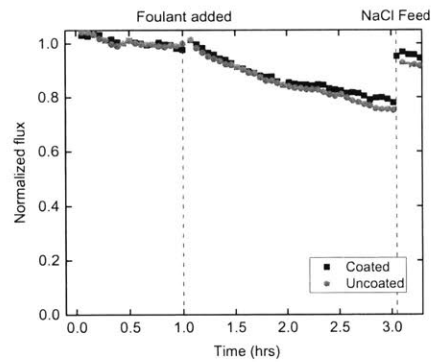
(c) 1500 mg/L hexadecane-in-water emulsion Dead-end
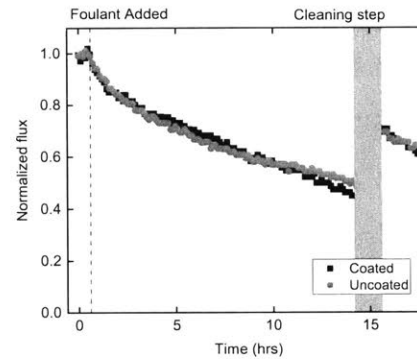
(d) 1500 mg/L hexadecane-in-water emulsion Crossflow

Figure 5-10: Fouling and cleaning performance for coated vs. uncoated membranes subjected to (a) 1500 mg/L SDS stabilized hexadecane-in-water emulsion, (b) 1500 mg/L Tween 80 stabilized hexadecane-in-water emulsion, (c,d) 1500 mg/L hexadecane-in-water emulsion. Tests (a-c) were performed in dead-end flow and test (d) was performed in a cross-flow setup. Initial flux for all tests was 30 ±2 LMH and 2 g/L NaCl desalination step is shown before foulant addition step.

5.4 Conclusions

In-air hydrophilic/oleophobic membranes have recently received attention from researchers due to their purported anti-fouling performance. In this work we have functionalized reverse osmosis (RO) membranes to be highly in-air oleophobic while maintaining their in-air hydrophilicity. We characterized uncoated and optimally coated surfaces by X-ray photoelectron spectroscopy, attenuated total reflectance-Fourier transform infrared spectroscopy, atomic force microscopy, and by measuring in-air and underwater oil contact angles. We show that although coated membranes exhibit a very high in-air oil contact angle relative to uncoated membranes, the underwater contact angles for both are nearly identical. We attribute this result due to PFA chain reconstruction: the same reconstruction which allowed hydrophilicity of the coated membranes in an air environment. Furthermore, we show that coated membranes exhibit little to no reduction in flux decline during surfactant stabilized and surfactant-free oil-in-water emulsion desalination and filtration. Coated membranes did exhibit a slight increase in flux recovery, but we attribute this to the roughness of the membrane during the coating process rather than the modified surface chemistry.

Acknowledgments

Appendix A

Supplementary information for Ch. 2

A.1 Data handling details

MATLAB was used to read data output from the scale which was recorded every 5 seconds for crossflow tests and every second for dead-end batch tests. The derivative of mass with respect to time was calculated by using a forward finite difference function averaged over 8 minutes. Flux was calculated by dividing this quantity by the product of the active membrane area and the density of pure water as given by Eq. A.1.

$$J = \frac{\Delta m}{\Delta t \cdot A_m \cdot \rho_p} \tag{A.1}$$

Vectors for time and mass were also averaged over 8 minutes so that the size of time, mass, and flux vectors were equal. From these data, roughly 1000 points were taken per hour for both dead-end and crossflow tests.

About 0.2% of the points in the dead-end batch mass data were higher than their later five neighboring points by greater than 0.25% and were removed using an automatic algorithm. These points were due to the high stagnation pressure arising from droplets striking the air-water interface in the permeate tank during mass collection and were randomly distributed throughout the data.

To attenuate high frequency noise in the flux data, a simple central moving average filter was applied for a total of seven neighboring points for dead-end and crossflow experiments. The steady state flux J^* was determined by averaging the last 30 values for flux in each dataset.

Appendix B

Supplementary information for

Ch. 3

Talal F. Qahtan[1], Leonardo D. Banchik[2], Mohammed A. Gondal, Gibum Kwon, Divya Panchanathan, Mohammed A. Dastageer, and Gareth McKinley

B.1   Organics degradation model

We begin our model with the Langmuir-Hinshelwood relation for concentration reduction as a function of time due to adsorption and reaction at a surface as is often done in the literature [56, 57, 59]:

$$\frac{dC}{dt} = -\frac{k_p k_{ads} C}{1 - k_{ads} C} \tag{B.1}$$

where C is the concentration of organic pollutant (mg/L), t is the organic pollutant residence time within the TiO$_2$ reactor volume (s), k_{ads} is the adsorption constant of the organic molecule to be degraded (L/mg), and k_p is a rate constant associated with the photocatalytic process (mg/L-s).

The maximum organic contaminant (MB dye) concentration used in this study was 5 mg/L and the adsorption constant for methylene blue dye is $k_{ads} = 1.95 \times 10^{-2}$ L/mg [57].

---

[1]TFQ contributed to the work in this chapter by performing all experiments and aiding in writing of the manuscript.

[2]LDB contributed to the work in this chapter by collaborating on the novel feed-side membrane coating, performing all modeling, and aiding in writing of the manuscript.

Therefore, we can safely assume that $k_{ads}C \ll 1$, so that Eq. B.1 reduces to a first order kinetics reaction:

$$\frac{dC}{dt} \approx -k_p k_{ads} C = -k_{app} C \tag{B.2}$$

where k_{app} is an applied rate constant (s^{-1}). When the UV illumination power I provided exceeds a threshold value of between 1 and 10 mW/cm^2, as it does in our current work, then k_{app} is linearly proportional to $I^{1/2}$ with a proportionality constant which we call β (cm/mW$^{1/2}$-s) [59, 73]:

$$k_{app} = \beta I^{1/2} \tag{B.3}$$

Rearranging and taking the integral of Eq. B.2 with initial condition $C(t_o = 0, t) = (C_0, C_t)$ yields the following expression for C as a function of time:

$$C_t = C_0 \exp(-\beta I^{1/2} t) \tag{B.4}$$

For a closed reactor within which there is no dispersion across particle streamlines, we can define the mean residence time t as the ratio of the reactor volume by the volume flow rate through the reactor [100]:

$$C_t = C_0 \exp\left(\frac{-\beta I^{1/2} V_r}{J_w A_s}\right) \tag{B.5}$$

where V_r (m^3) is the volume of the TiO$_2$ coating that participates in the degradation reaction and through which the permeate flows, J_w is the permeate flux through the membrane (m/s), and A_s is the wetted surface area of the membrane (m^2). Defining a dimensionless degradation efficiency as $\alpha = 1 - C_t/C_0$ and multiplying the term in the exponential function by n to allow for multiple passes of equal residence time through the reactor yields parameters relevant to the current system:

$$\alpha = 1 - \exp\left(\frac{-\beta I^{1/2} V_r n}{J_w A_s}\right) = 1 - \exp(-\beta X) \tag{B.6}$$

where X is a collapsed variable which encapsulates several input parameters.

V_r was estimated by considering the amount of TiO$_2$ which coats the permeate side of

the multifunctional membrane. Because the mesh used in this study was a complex twill Dutch weave wire cloth, we estimate the reactor volume by subtracting the volume of the wires of the mesh from the total volume occupied by the mesh. All the calculations were performed using data from the manufacturer's website. The volume of the wire material is attained by dividing the specific weight of the mesh 0.488 kg/m^2 by the density of 316 stainless steel 7990 kg/m^3 and multiplying by the wetted mesh area to give 1.23×10^{-8} m^3. The volume occupied by the mesh is given by multiplying the mesh thickness 86.36×10^{-6} m by the wetted mesh area to give 1.74×10^{-8} m^3. Taking the difference of these volumes gives the volume of the pores in the mesh of 5.08×10^{-9} m^3. We now consider that only the lower half of the mesh has been coated with TiO$_2$ and is photoactive so that the reactor volume is 2.55×10^{-9} m^3.

To verify whether this volume is justified, we calculated the volume of the pores from an SEM image of the mesh. The membrane is composed of a repeating array of pores as shown in Fig. B-1. The image on the right shows the structure of a typical 'twill Dutch weave' in order to visualize our reactor construct.
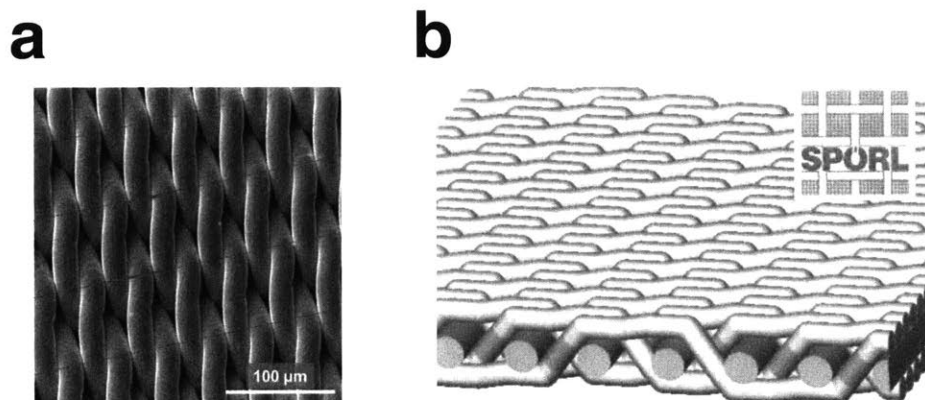
Figure B-1: Twill Dutch weave mesh: (a) SEM image of mesh, (b) Digital visualization of mesh from http://www.spoerl.de/en/wp-content/uploads/sites/2/2014/08/0008_big-458x300.jpg.

The contaminants in the water react on the TiO$_2$ coated bottom side of the mesh as they pass through the pores. Each pore is modeled as a microreactor whose approximate volume per unit projected area is approximately calculated as below:

Area of the repeating unit, $A_{unit} = 3096.88$ μm^2

Diameter of wire, $D_{wire} = 25.4$ μm

Width between the warp wires = Width of the pore, $w_{pore} = 21.5$ μm

Height of the pore, $h_{pore} = D_{wire}$

Length of the pore, $l_{pore} = 72.4$ μm

Volume of pore, $V_{pore} \approx h_{pore}w_{pore}l_{pore} = 39537$ μm^2

Volume of pore per unit area of mesh, $V_{pore} = \frac{V_{unit,pore}}{A_{unit}} = 12.77 \times 10^{-6}$ m^3/m^2

Multiplying the volume of the pore per unit area by the area of the wetted membrane yields a reactor volume of 2.57×10^{-9} m^3 which has a relative difference of 0.66% from the reactor volume of 2.55×10^{-9} m^3 calculated above. Therefore, our estimation of the TiO$_2$ reactor volume is verified.

B.2   Data from organics degradation experiment

Tables B.1 and B.2 contain the experimental parameter inputs (I, n, X), experimental degradation efficiency and standard deviation (α_{exp}, σ_{exp}), model degradation efficiency (α_{mod}), and model error (ε) for the fixed intensity and fixed passes data shown in Fig. 3-4d of the main paper, respectively. Model error was determined by $\varepsilon = 1 - \alpha_{mod}/\alpha_{exp}$. For all experiments, the average flux was $J_w = 4015$ L/m^2-hr which is 1.12×10^{-3} m/s, cross-sectional area was $A_s = 2.01 \times 10^{-4}$ m^2, and excited volume of the TiO$_2$ reactor was $V_r = 2.55 \times 10^{-9}$ m^3. From the manuscript, $\beta = 1.174$ cm/mW$^{1/2}$-s and the first-order photocatalytic rate constant $k_{app} = \beta I^{1/2}$ varies between 14.38×10^{-3} s^{-1} and 45.93×10^{-3} s^{-1} for the range of parameters used in our study.

Table B.1: Effect of fixed UV intensity and varying passes on degradation efficiency

I (mW/cm^2)	n	X (mW$^{1/2}$-hr/cm)	α_{exp} (%)	σ_{exp} (%)	α_{mod} (%)	ε (%)
372	2	0.44	40.5	3.0	40.3	0.6
372	4	0.88	64.3	3.0	64.3	0.0
372	6	1.32	78.5	3.5	78.7	0.2
372	8	1.75	87.0	3.0	87.3	0.3
372	10	2.19	92.2	1.1	92.4	0.2
372	12	2.63	95.3	2.0	95.5	0.2

Table B.2: Effect of varying UV intensity and fixed passes on degradation efficiency

I (mW/cm^2)	n	X (mW$^{1/2}$-hr/cm)	α_{exp} (%)	σ_{exp} (%)	α_{mod} (%)	ε (%)
150	2	0.28	27.8	3.5	27.9	0.4
250	2	0.36	34.5	3.1	34.4	0.2
372	2	0.44	40.5	3.0	40.3	0.6
548	2	0.53	48.3	2.8	46.5	3.7
820	2	0.65	54.9	1.8	53.4	2.6
1050	2	0.74	58.9	1.3	57.9	1.6
1270	2	0.81	62.2	1.2	61.4	1.3
1530	2	0.89	66.0	1.1	64.8	1.8
150	6	0.84	65.1	1.6	62.5	3.9
250	6	1.08	74.5	1.5	71.8	3.6
372	6	1.32	78.5	3.5	78.7	0.2
548	6	1.60	85.9	1.3	84.7	1.4
820	6	1.95	91.4	1.1	89.9	1.6
1050	6	2.21	93.4	1.4	92.5	1.0
1270	6	2.43	95.3	1.1	94.2	1.1
1530	6	2.67	96.4	1.0	95.6	0.8
150	10	1.39	82.7	1.4	80.5	2.6
250	10	1.80	88.9	1.0	87.9	1.1
372	10	2.19	92.2	1.0	92.4	0.2
548	10	2.66	96.7	0.8	95.6	1.1
820	10	3.26	99.0	0.6	97.8	1.2
1050	10	3.68	100.0	0.0	98.7	1.3
1270	10	4.05	100.0	0.0	99.1	0.9
1530	10	4.45	100.0	0.0	99.5	0.5

B.3   Supplementary figures

a Uncoated glass
Water CA = 0°   Oil CA = 0°

c SiO$_2$ coated glass
Water CA = 0°   Oil CA = 0°

b FS-50 coated glass
Water CA = 16±2°   Oil CA = 80±2°
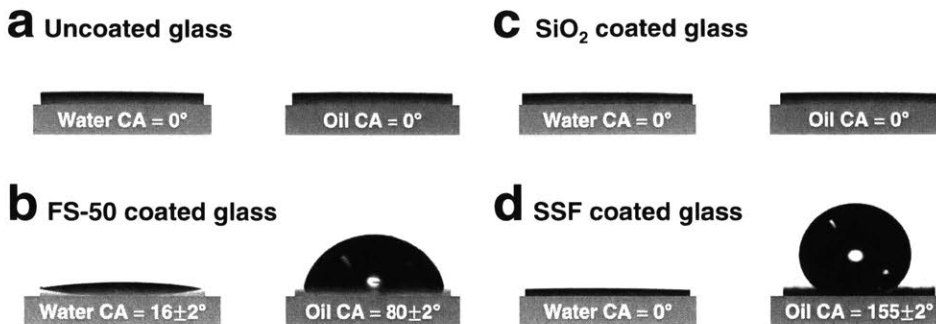
d SSF coated glass
Water CA = 0°   Oil CA = 155±2°

Figure B-2: Static contact angles of oil (hexadecane) and water on (a) uncoated glass and (b-d) coated glass.

Figure B-2 shows the static contact angles of uncoated, FS-50 coated, SiO$_2$ coated, and SiO$_2$/SF-100/FS-50 (SSF) coated glass by water and oil (hexadecane $\gamma_{LV} = 27.5$ mN/m). The uncoated glass is superhydrophilic and superoleophilic (SHL/SOL) as indicated in Fig. B-2a. FS-50 coated glass is hydrophilic (HL) and oleophobic (OB) due to the fluorinated groups inherent in FS-50 which are omniphobic but reconfigure when in the presence of polar liquids with a small molecular size such as water as depicted in Fig. B-2b. This wetting behavior holds promise for wettability enhancement with the addition of SiO$_2$ nanoparticles for roughness. As shown in Fig. B-2c, the SiO$_2$ coated surface, like uncoated glass, is also SHL/SOL. Both FS-50 and the SiO$_2$ dispersion in acetone have negative zeta potentials [53] indicating the importance of using a strong binder such as SF-100 (which is not soluble in water, unlike PDDA) to hold both layers together. SSF coated surfaces are SHL and superoleophobic (SOB) as depicted in Fig. B-2d. This result indicates that the wettability of SSF coated glass by oil is in the Cassie-Baxter state while water is in the Wenzel state.

Figure B-3 illustrates the robustness of the TiO$_2$ membrane coating by comparing the measured photocatalytic degradation efficiency α (%) for 5 separate feed samples with the same initial concentration of MB dye ($C_o = 5$ mg/L) and volume (10 mL) after 10 passes for each sample using the same membrane at a constant UV intensity (372 mW/cm^2). Standard deviation for these data were less than 0.45%. Inset shows the absorbance of the
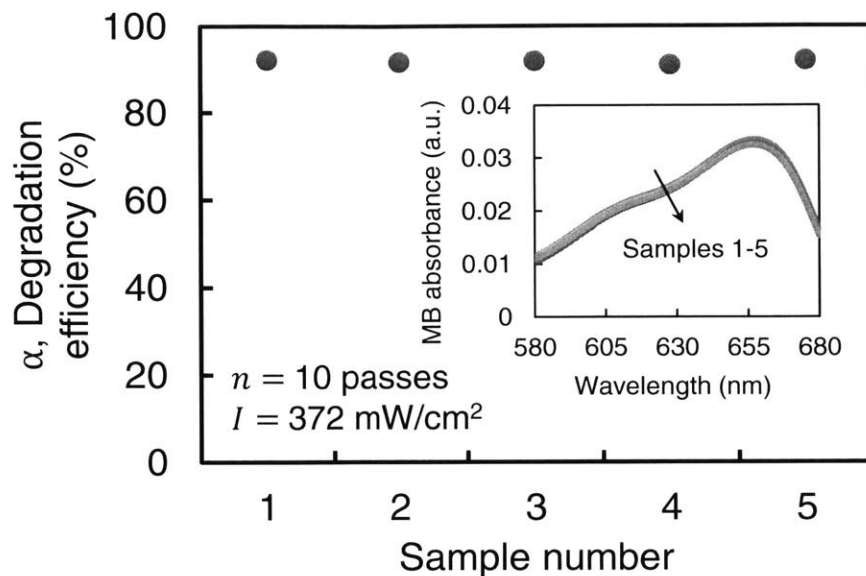
Figure B-3: Degradation experiment repeatability and TiO_2 robustness as shown by identical degradation efficiency and MB absorbance for 5 experimental runs.

five samples as nearly equivalent after each group of 10 passes illustrating the robustness of the permeate-side coating. In another robustness test, we also measured the degradation efficiency attained after every 2 passes as a function of the number of passes and found this value to be a constant $40.0 \pm 2.0\%$ as shown in Supplementary Fig. B-4.

Figure B-4 shows that for increasing passes at a given UV intensity and water flux, the concentration of MB Dye decreases exponentially while the degradation efficiency per two passes remains nearly constant. The latter result further indicates the robustness of the TiO_2 coating.

Figure B-5 illustrates high system oil rejection as evidenced by nearly pure permeate after 10 passes of gravity driven separation of a bulk 1:1 mixture of hexadecane and water by volume.

Figure B-6 shows the feed and permeate droplet size characteristics before and after the separation of surfactant-stabilized oil-water emulsions and simultaneous organics degradation of MB Dye present in the water phase. We can clearly see that many of the large droplets present in the feed stream are not present in the permeate stream after separa-
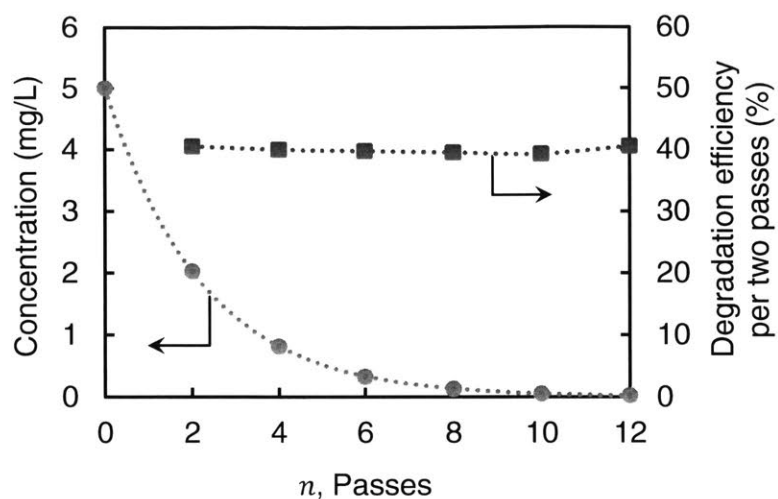
Figure B-4: Concentration of MB Dye (red circles) and degradation efficiency per two passes (green squares) as a function of the number of passes using TiO_2 coated membranes at constant UV light intensity ($I = 372$ mW/cm^2). Dotted lines connecting data markers were included to guide the eye. Uncertainties for all data are smaller than the data markers.
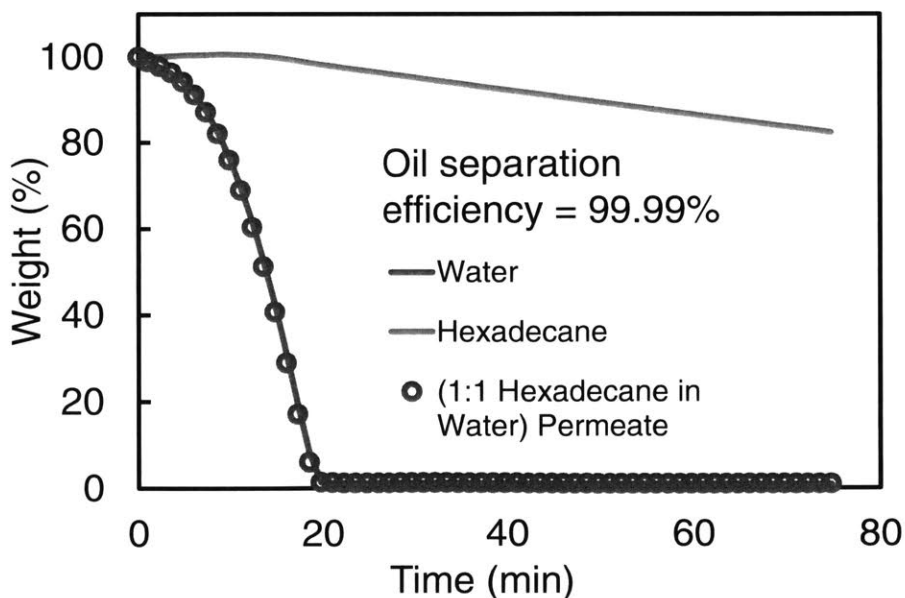
Figure B-5: Thermogravimetric analysis (TGA) data of water, hexadecane, and feed solution permeate after 10 passes with high oil rejection.

1:4 by volume
(oil:water)

1:1

4:1

a

c

e

100 μm

100 μm

100 μm

b

Frequency

60
40
20
0

3.42 ± 2.10 μm

0.1 1 10 100
Diameter (μm)

d

40

20

0

3.09 ± 1.33 μm

0.1 1 10 100
Diameter (μm)

f

60
40
20
0

1.81 ± 1.56 μm

0.1 1 10 100
Diameter (μm)

g

100 μm

h

100 μm

i

100 μm
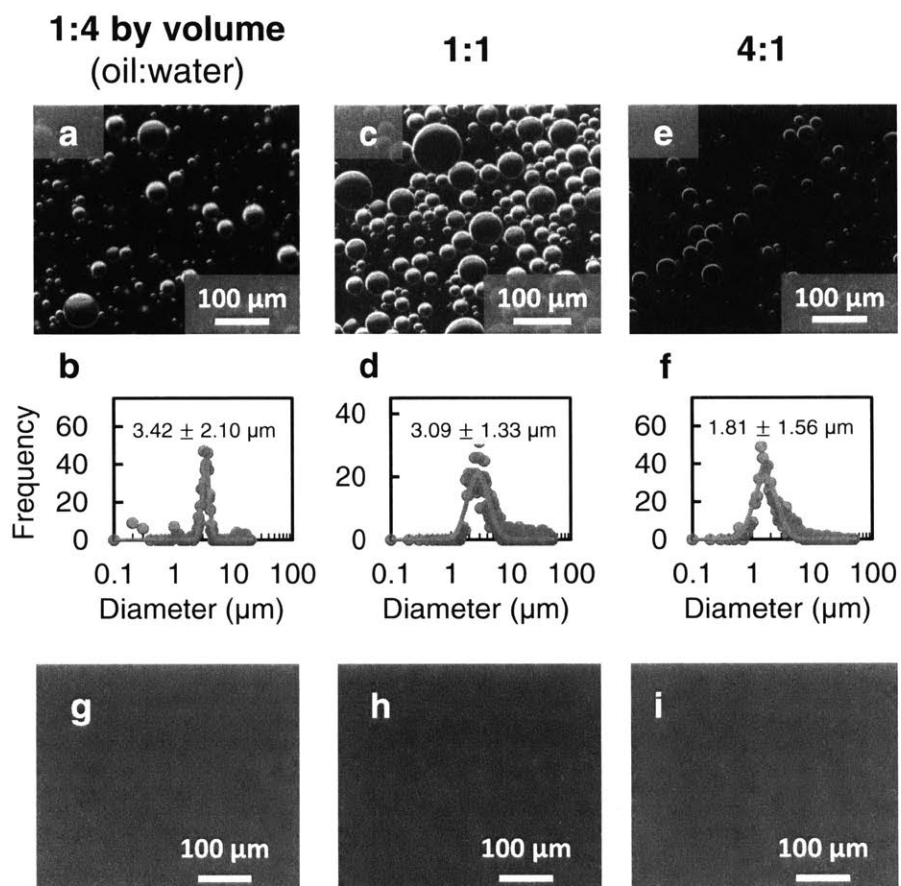
Figure B-6: Separation of surfactant-stabilized oil-water emulsions and simultaneous organics degradation of MB Dye present in the water phase. (a, c, and e) Optical microscopy images of 1:4, 1:1, and 4:1 (hexadecane:water by volume) emulsions, respectively. 1:4 and 1:1 emulsions are oil-in-water and 4:1 emulsion is water-in-oil. (b, d, and e) Droplet size distributions of 1:4, 1:1, and 4:1 emulsions, respectively. (g, h, and i) Optical microscopy images of 1:4, 1:1, and 4:1 permeates, respectively.

113

tion. Some droplets smaller than the membrane pore size, however, permeated through the membrane and their size distributions are provided in Supplementary Fig. B-7.
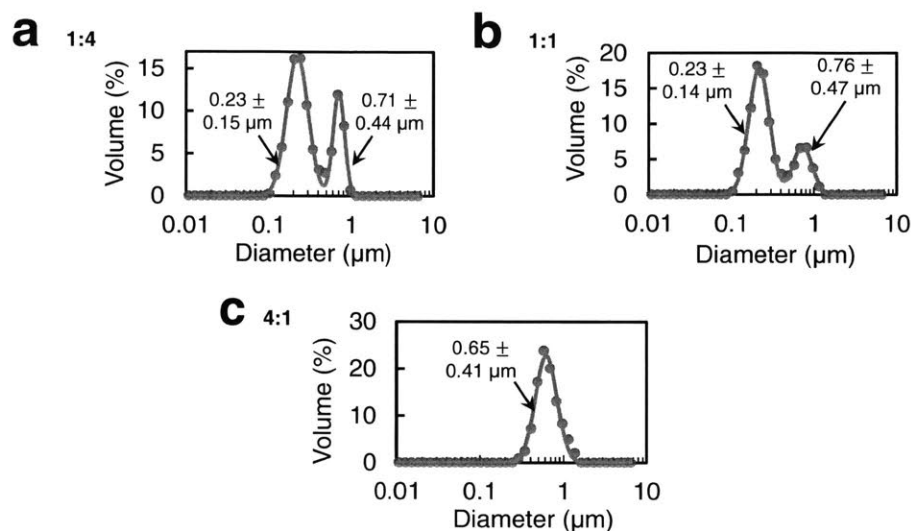
Figure B-7: Volume-based droplet size distributions of permeate from (a) 1:4, (b) 1:1, (c) 4:1 surfactant stabilized oil-water emulsions with one pass. 1:4 and 1:1 emulsions are oil-in-water (SDS stabilized) and 4:1 is a water-in-oil emulsion (Span80 stabilized).

Figure B-7 gives the volume-based droplet size distribution of permeate from feed solutions of (a) 1:4, (b) 1:1, and (4:1) surfactant stabilized oil-water emulsions with one pass. 1:4 and 1:1 emulsions are oil-in-water (SDS stabilized) and 4:1 is a water-in-oil emulsion (Span80 stabilized). 1:4 and 1:1 permeate droplet diameters are perfectly described by bimodal log-normal distributions whereas the 4:1 permeate droplet diameters are described by a log-normal distribution. Droplet diameter mean and standard deviation of both peaks are given. The largest detected permeate droplet diameters were 0.97, 1.16, and 1.38 μm for the 1:4, 1:1, and 4:1 emulsions, respectively, which are below the mesh pore size of 2 μm. The reason for the roughly 1 μm difference between pore size and the largest detected droplet in the permeate is predominantly due to the fact that the average pore size for the multifunctional membrane has been reduced below 2 μm due to the two applied coatings.

Figure B-8 shows the effective thickness of the TiO_2 coating as measured by the absorbance spectra of TiO_2 thin films in the UV region. 0.5, 1, and 1.5 mL of a 5 mg/mL TiO_2 in THF dispersion are sprayed onto 1 cm^2 of glass substrate to fabricate three TiO_2

114
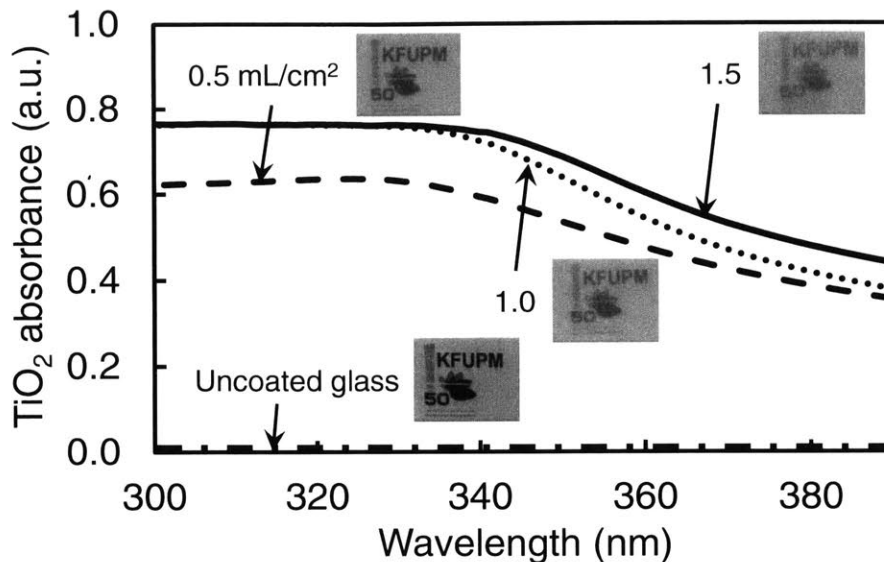
Figure B-8: Optimization of TiO$_2$ coating thickness.

thin films (Inset). The absorbance spectra of the three TiO$_2$ thin films measured between 300 and 388 nm which correspond to the wavelength associated with the maximum photon energy emission by the UV source used in our study and the band gap of TiO$_2$, respectively. Because the 1.5 mL/cm^2 absorption spectrum overlaps the 1 mL/cm^2 spectrum at 300 nm, we can deduce that it is an optimum thickness because it absorbs as much UV as the lesser thickness. From these results, we used 1.5 mL/cm^2 for all TiO$_2$ permeate-side coatings in the present study.

Bibliography

[1] A. Needs, "The HLB SYSTEM a time-saving guide to emulsifer selection," tech. rep., ICI Americas Inc., 1980.

[2] M. Cheryan and N. Rajagopalan, "Membrane processing of oily streams. Wastewater treatment and waste reduction," *Journal of Membrane Science*, vol. 151, pp. 13–28, 1998.

[3] C. H. Peterson, S. D. Rice, J. W. Short, D. Esler, J. L. Bodkin, B. E. Ballachey, and D. B. Irons, "Long-term ecosystem response to the Exxon Valdez oil spill," *Science*, vol. 302, no. 5653, pp. 2082–2086, 2003.

[4] K. Dahm and M. Chapman, "Produced water treatment primer: Case studies of treatment applications," tech. rep., U.S. Department of the Interior and Bureau of Reclamation, 2014.

[5] A. Fakhru'l-Razi, A. Pendashteh, L. C. Abdullah, D. R. A. Biak, S. S. Madaeni, and Z. Z. Abidin, "Review of technologies for oil and gas produced water treatment," *Journal of Hazardous Materials*, vol. 170, no. 2-3, pp. 530–551, 2009.

[6] W. L. Ellsworth, "Injection-induced earthquakes," *Science*, vol. 341, no. 6142, p. 1225942, 2013.

[7] A. McGarr, B. Bekins, N. Burkardt, J. Dewey, P. Earle, W. Ellsworth, S. Ge, S. Hickman, A. Holland, E. Majer, *et al.*, "Coping with earthquakes induced by fluid injection," *Science*, vol. 347, no. 6224, pp. 830–831, 2015.

[8] H. Butt, K. Graf, and M. Kappl, *Physics and Chemistry of Interfaces*. Darmstadt, Germany: WILEY-VCH GmbH & Co. KGaA, 2003.

[9] W. C. Griffin, "Calculation of HLB values of non-ionic surfactants," *Journal of the Society of Cosmetic Chemists*, vol. 5, pp. 249–256, 1954.

[10] L. Henthorne, "Evaluation of membrane pretreatment for seawater reverse osmosis desalination," tech. rep., U.S. Department of the Interior Bureau of Reclamation, 2007.

[11] B. D. Freeman, "Novel fouling-reducing coatings for ultrafiltration, nanofiltration, and reverse osmosis membranes," final scientific/technical report, Department of Energy, August 2008.

[12] A. Bevis, "The treatment of oily water by coalescing," *Filtration & Separation*, vol. 29, pp. 295–300, Jul 1992.

[13] M. Stewart and K. Arnold, *Emulsions and Oil Treating Equipment - Selection, Sizing and Troubleshooting.* Elsevier, Jan 2009.

[14] P. Cañizares, F. Martínez, J. Lobato, and M. A. Rodrigo, "Break-up of oil-in-water emulsions by electrochemical techniques," *Journal of hazardous materials*, vol. 145, pp. 233–40, jun 2007.

[15] M. Shannon, P. W. Bohn, M. Elimelech, J. G. Georgiadis, B. J. Mariñas, and A. M. Mayes, "Science and technology for water purification in the coming decades," *Nature*, vol. 452, no. March, pp. 301–310, 2008.

[16] G. P. Thiel, E. W. Tow, L. D. Banchik, H. W. Chung, and J. H. Lienhard, "Energy consumption in desalinating produced water from shale oil and gas extraction," *Desalination*, vol. 366, pp. 94–112, 2015.

[17] L. F. Greenlee, D. F. Lawler, B. D. Freeman, B. Marrot, and P. Moulin, "Reverse osmosis desalination: water sources, technology, and today's challenges.," *Water research*, vol. 43, pp. 2317–48, may 2009.

[18] DOW Water & Process Solutions, *FILMTEC Reverse Osmosis Membranes - Technical Manual*, 2011.

[19] J. Mueller, "Crossflow microfiltration of oily water," *Journal of Membrane Science*, vol. 129, no. 2, pp. 221–235, 1997.

[20] A. Koltuniewicz, R. Field, and T. Arnot, "Cross-flow and dead-end microfiltration of oily-water emulsion. Part I: Experimental study and analysis of flux decline," *Journal of Membrane Science*, vol. 102, pp. 193–207, 1995.

[21] T. Arnot, R. Field, and A. Koltuniewicz, "Cross-flow and dead-end microfiltration of oily-water emulsions Part II. mechanisms and modelling of flux decline," *Journal of Membrane Science*, vol. 169, pp. 1–15, 2000.

[22] G. K. Pearce, *UF/MF Membrane Water Treatment.* Wangthonglang: Water Treatment Academy, TechnoBiz Communications Co., Ltd., 2011.

[23] G. M. Geise, H.-S. Lee, D. J. Miller, B. D. Freeman, J. E. McGrath, and D. R. Paul, "Water purification by membranes: The role of polymer science," *Journal of Polymer Science: Part B: Polymer Physics*, vol. 48, pp. 1685–1718, 2010.

[24] D. Rana and T. Matsuura, "Surface modifications for antifouling membranes," *Chemical Reviews*, vol. 110, no. 4, pp. 2448–2471, 2010.

[25] Guo-dong Kang and Yi-ming Cao, "Development of antifouling reverse osmosis membranes for water treatment: A review," *Water Research*, vol. 46, pp. 584–600, 2012.

[26] A. K. Kota, G. Kwon, W. Choi, J. M. Mabry, and A. Tuteja, "Hygro-responsive membranes for effective oil-water separation.," *Nature communications*, vol. 3, p. 1025, jan 2012.

[27] P. Brown, O. Atkinson, and J. Badyal, "Ultrafast oleophobic-hydrophilic switching surfaces for anti-fogging, self-cleaning, and oil-water separation," *ACS Applied Materials & Interfaces*, vol. 6, pp. 7504–7511, 2014.

[28] P. S. Brown and B. Bhushan, "Bioinspired, roughness-induced, water and oil super-philic and super-phobic coatings prepared by adaptable layer-by-layer technique," *Scientific Reports*, vol. 5, 2015.

[29] S. Pan, R. Guo, and W. Xu, "Durable superoleophobic fabric surfaces with counterintuitive superwettability for polar solvents," *AIChE Journal*, vol. 60, no. 8, pp. 2752–2756, 2014.

[30] J. Yang, Z. Zhang, X. Xu, X. Zhu, X. Men, and X. Zhou, "Superhydrophilic-superoleophobic coatings," *Journal of Materials Chemistry*, vol. 22, pp. 2834–2837, 2012.

[31] X. Zhu, W. Tu, K.-H. Wee, and R. Bai, "Effective and low fouling oil/water separation by a novel hollow fiber membrane with both hydrophilic and oleophobic surface properties," *Journal of Membrane Science*, vol. 466, pp. 36–44, sep 2014.

[32] J. a. Howarter and J. P. Youngblood, "Amphiphile grafted membranes for the separation of oil-in-water dispersions," *Journal of Colloid and Interface Science*, vol. 329, no. 1, pp. 127–132, 2009.

[33] X. Zhu, H.-E. Loo, and R. Bai, "A novel membrane showing both hydrophilic and oleophobic surface properties and its non-fouling performances for potential water treatment applications," *Journal of Membrane Science*, vol. 436, pp. 47–56, jun 2013.

[34] X. Zhu, W. Tu, K.-H. Wee, and R. Bai, "Effective and low fouling oil/water separation by a novel hollow fiber membrane with both hydrophilic and oleophobic surface properties," *Journal of Membrane Science*, vol. 466, pp. 36–44, 2014.

[35] R. T. Duraisamy, A. H. Beni, and A. Henni, *State of the Art Treatment of Produced Water, Water Treatment*. InTech, 2013.

[36] R. W. Baker, *Membrane Technology and Applications: Ultrafiltration*. John Wiley & Sons, Ltd., 3rd ed., 2012.

[37] K. J. Howe, D. W. Hand, J. C. Crittenden, R. R. Trussell, and G. Tchobanoglous, *Principles of Water Treatment*. Wiley, 1 edition, 2012.

[38] R. Field, S. Hang, and T. Arnot, "The influence of surfactant on water flux through microfiltration membranes," *Journal of Membrane Science*, vol. 86, no. 3, pp. 291–304, 1994.

[39] A.-S. Jönsson and B. Jönsson, "The influence of nonionic and ionic surfactants on hydrophobic and hydrophilic ultrafiltration membranes," *Journal of Membrane Science*, vol. 56, no. 1, pp. 49–76, 1991.

[40] R. W. Field, D. Wu, J. A. Howell, and B. B. Gupta, "Critical flux concept for microfiltration fouling," *Journal of Membrane Science*, vol. 100, no. 3, pp. 259–272, 1995.

[41] A. B. Koltuniewicz and R. Field, "Process factors during removal of oil-in-water emulsions with cross-flow microfiltration," *Desalination*, vol. 105, pp. 79–89, 1996.

[42] J. Pope, S. Yao, and A. Fane, "Quantitative measurements of the concentration polarization layer thickness in membrane filtration of oil-water emulsions using NMR micro-imaging," *Journal of Membrane Science*, vol. 118, pp. 247–257, 1996.

[43] D. Lu, T. Zhang, and J. Ma, "Ceramic membrane fouling during ultrafiltration of oil/water emulsions: Roles played by stabilization surfactants of oil droplets," *Environmental Science & Technology*, vol. 49, pp. 4235–4244, 2015.

[44] E. N. Tummons, V. V. Tarabara, J. W. Chew, and A. G. Fane, "Behavior of oil droplets at the membrane surface during crossflow microfiltration of oil-water emulsions," *Journal of Membrane Science*, vol. 500, pp. 211–224, 2016.

[45] P. Hermans and H. Bredée, "Principles of the mathematical treatment of constant-pressure filtration," *J. Soc. Chem. Ind*, vol. 55, pp. 1–4, 1936.

[46] J. Hermia, "Constant pressure blocking filtration law application to power-law non-newtonian fluid," *Trans. Inst. Chem. Eng.*, vol. 60, pp. 183–187, 1982.

[47] R. W. Field and J. J. Wu, "Modelling of permeability loss in membrane filtration: Re-examination of fundamental fouling equations and their link to critical flux," *Desalination*, vol. 283, pp. 68–74, 2011.

[48] Y. C. Jung and B. Bhushan, "Wetting behavior of water and oil droplets in three-phase interfaces for hydrophobicity/philicity and oleophobicity/philicity," *Langmuir*, vol. 25, pp. 14165–14173, 2009.

[49] J. C. Crittenden, R. R. Trussell, D. W. Hand, K. J. Howe, and G. Tchobanoglous, *Water treatment: principles and design.* Wiley, 3 edition, 2012.

[50] D. M. Dresselhuis, G. A. van Aken, E. H. A. de Hoog, and M. A. Cohen Stuart, "Direct observation of adhesion and spreading of emulsion droplets at solid surfaces," *Soft Matter*, vol. 4, pp. 1079–1085, 2008.

[51] D. J. Miller, S. Kasemset, L. Wang, D. R. Paul, and B. D. Freeman, "Constant flux crossflow filtration evaluation of surface-modified fouling-resistant membranes," *Journal of Membrane Science*, vol. 452, pp. 171–183, feb 2014.

[52] Z. He, D. J. Miller, S. Kasemset, L. Wang, D. R. Paul, and B. D. Freeman, "Fouling propensity of a poly(vinylidene fluoride) microfiltration membrane to several model oil/water emulsions," *Journal of Membrane Science*, vol. 514, pp. 659 – 670, 2016.

[53] P. S. Brown and B. Bhushan, "Mechanically durable, superoleophobic coatings prepared by layer-by-layer technique for anti-smudge and oil-water separation," *Scientific Reports*, vol. 5, p. 8701, 2015.

[54] C. S. Turchi and D. F. Ollis, "Photocatalytic degradation of organic-water contaminants - mechanisms involving hydroxyl radical attack.," *Journal of Catalysis*, vol. 122, p. 178, 1990.

[55] G. L. Linsebigler, Amy L. and J. T. Yates Jr., "Photocatalysis on TiO_2 surfaces: Principles, mechanisms, and selected results," *Chemical Reviews*, vol. 95, no. 3, pp. 735–758, 1995.

120

[56] A. Fujishima, T. Rao, and D. Tryk, "Titanium dioxide photocatalysis," *Journal of Photochemistry and Photobiology C: Photochemistry Reviews*, vol. 1, no. March, pp. 1–21, 2000.

[57] A. Houas, H. Lachheb, M. Ksibi, E. Elaloui, C. Guillard, and J. Herrmann, "Photocatalytic degradation pathway of methylene blue in water," *Applied Catalysis B: Environmental*, vol. 31, no. 2, pp. 145–157, 2001.

[58] K. Sunada, T. Watanabe, and K. Hashimoto, "Studies on photokilling of bacteria on TiO_2 thin film," *Journal of Photochemistry and Photobiology A: Chemistry*, vol. 156, no. 1-3, pp. 227–233, 2003.

[59] A. V. Emeline, V. Ryabchuk, and N. Serpone, "Factors affecting the efficiency of a photocatalyzed process in aqueous metal-oxide dispersions," *Journal of Photochemistry and Photobiology A: Chemistry*, vol. 133, no. 1-2, pp. 89–97, 2000.

[60] C. Gao, Z. Sun, K. Li, Y. Chen, Y. Cao, S. Zhang, and L. Feng, "Integrated oil separation and water purification by a double-layer TiO_2-based mesh," *Energy & Environmental Science*, vol. 6, p. 1147, 2013.

[61] X. Lin, Y. Chen, N. Liu, Y. Cao, L. Xu, W. Zhang, and L. Feng, "In situ ultrafast separation and purification of oil/water emulsions by superwetting TiO_2 nanocluster-based mesh," *Nanoscale*, vol. 8, no. 16, pp. 8525–8529, 2016.

[62] L. Li, Z. Liu, Q. Zhang, C. Meng, T. Zhang, and J. Zhai, "Underwater superoleophobic porous membrane based on hierarchical TiO_2 nanotubes: multifunctional integration of oil/water separation, flow-through photocatalysis and self-cleaning," *J. Mater. Chem. A*, vol. 3, pp. 1279–1286, 2015.

[63] N. C. Raut, T. Mathews, P. K. Ajikumar, R. P. George, S. Dash, and A. K. Tyagi, "Sunlight active antibacterial nanostructured n-doped TiO_2 thin films synthesized by an ultrasonic spray pyrolysis technique," *RSC Advances*, vol. 2, no. 28, p. 10639, 2012.

[64] D. F. Swinehart, "The Beer-Lambert Law," *Journal of Chemical Education*, vol. 39, no. 7, p. 333, 1962.

[65] B. Chakrabarty, A. Ghoshal, and M. Purkait, "Ultrafiltration of stable oil-in-water emulsion by polysulfone membrane," *Journal of Membrane Science*, vol. 325, no. 1, pp. 427–437, 2008.

[66] A. Cassie and S. Baxter, "Wettability of porous surfaces," *Transactions of the Faraday Society*, vol. 40, pp. 546–551, 1944.

[67] A. K. Kota, W. Choi, and A. Tuteja, "Superomniphobic surfaces: Design and durability," *MRS Bulletin*, vol. 38, pp. 383–390, 2013.

[68] H. Sawada, Y. Ikematsu, T. Kawase, and Y. Hayakawa, "Synthesis and surface properties of novel fluoroalkylated flip-flop-type silane coupling agents," *Langmuir*, vol. 12, no. 15, pp. 3529–3530, 1996.

[69] G. Kwon, *Smart methodologies for efficient separation of liquid mixtures*. PhD thesis, University of Michigan, 2014.

[70] J. Li, L. Yan, W. Hu, D. Li, F. Zha, and Z. Lei, "Facile fabrication of underwater superoleophobic TiO$_2$ coated mesh for highly efficient oil/water separation," *Colloids and Surfaces A: Physicochemical and Engineering Aspects*, vol. 489, pp. 441–446, 2016.

[71] Y. Cao, N. Liu, W. Zhang, L. Feng, and Y. Wei, "One-step coating toward multifunctional applications: Oil/water mixtures and emulsions separation and contaminants adsorption," *ACS Applied Materials and Interfaces*, vol. 8, no. 5, pp. 3333–3339, 2016.

[72] S. Sablani, M. Goosen, R. Al-Belushi, and M. Wilf, "Concentration polarization in ultrafiltration and reverse osmosis: A critical review," *Desalination*, vol. 141, no. 3, pp. 269–289, 2001.

[73] D. Panchanathan, G. Kwon, M. A. Gondal, K. K. Varanasi, and G. H. McKinley, "Kinetics of in-situ photoinduced wettability switch on nanoporous TiO$_2$ surfaces under oil," *In Preparation*, 2016.

[74] F.-R. Ahmadun, A. Pendashteh, L. C. Abdullah, D. R. A. Biak, S. S. Madaeni, and Z. Z. Abidin, "Review of technologies for oil and gas produced water treatment," *Journal of Hazardous Materials*, vol. 170, pp. 530–551, 2009.

[75] L. D. Banchik and J. H. Lienhard V, "Effect of oil-in-water emulsion surfactant charge on fouling of model produced water in dead-end and crossflow filtration," *In preparation*, 2017.

[76] S. Chen, L. Li, C. Zhao, and J. Zheng, "Surface hydration: Principles and applications toward low-fouling/nonfouling biomaterials," *Polymer*, vol. 51, no. 23, pp. 5283–5293, 2010.

[77] J. A. Howarter and J. P. Youngblood, "Self-cleaning and anti-fog surfaces via stimuli-responsive polymer brushes," *Advanced Materials*, vol. 19, pp. 3838–3843, 2007.

[78] R. N. Wenzel, "Resistance of solid surfaces to wetting by water.," *Journal of Industrial and Engineering Chemistry*, vol. 28, pp. 988–994, 1936.

[79] Z. Xue, Y. Cao, N. Liu, L. Feng, and L. Jiang, "Special wettable materials for oil/water separation," *Journal of Materials Chemistry A*, vol. 2, pp. 2445–2460, 2014.

[80] G. Kwon, E. Post, and A. Tuteja, "Membranes with selective wettability for the separation of oil-water mixtures," *MRS Communications*, vol. 5, pp. 475–494, 2015.

[81] J. Yang, H. Song, X. Yan, H. Tang, and C. Li, "Superhydrophilic and superoleophobic chitosan-based nanocomposite coatings for oil/water separation," *Cellulose*, vol. 21, no. 3, pp. 1851–1857, 2014.

[82] K. Honda, M. Morita, H. Otsuka, and A. Takahara, "Molecular aggregation structure and surface properties of poly(fluoroalkyl acrylate) thin films," *Macromolecules*, vol. 38, pp. 5699–5705, 2005.

[83] A. Horinouchi, H. Atarashi, Y. Fujii, and K. Tanaka, "Dynamics of water-induced surface reorganization in poly(methylmethacrylate) films," *Macromolecules*, vol. 45, pp. 4638–4642, 2012.

[84] L. Li, Y. Wang, C. Gallaschun, T. Risch, and J. Sun, "Why can a nanometer-thick polymer coated surface be more wettable to water than to oil?," *Journal of Materials Chemistry*, vol. 22, pp. 16719–16722, 2012.

[85] Y. Wang, M. Dugan, B. Urbaniak, and L. Li, "Fabricating nanometer-thick simultaneously oleophobic/hydrophilic polymer coatings via a photochemical approach," *Langmuir*, vol. 32, pp. 6723–6729, 2016.

[86] Z. Wang, D. Hou, and S. Lin, "Composite membrane with underwater-oleophobic surface for anti-oil-fouling membrane distillation," *Environmental Science and Technology*, vol. 50, pp. 3866–3874, 2016.

[87] A. Liu, E. Goktekin, and K. K. Gleason, "Cross-linking and ultrathin grafted gradation of fluorinated polymers synthesized via initiated chemical vapor deposition to prevent surface reconstruction," *Langmuir*, vol. 30, no. 47, pp. 14189–14194, 2014.

[88] R. Zhang, Y. Liu, M. He, Y. Su, X. Zhao, M. Elimelech, and Z. Jiang, "Antifouling membranes for sustainable water purification: Strategies and mechanisms," *Chemical Society Reviews*, vol. 45, pp. 5888–5924, 2016.

[89] S. H. Baxamusa and K. K. Gleason, "Random copolymer films with molecular-scale compositional heterogeneities that interfere with protein adsorption," *Advanced Functional Materials*, vol. 19, no. 21, pp. 3489–3496, 2009.

[90] N. Kim, D. H. Shin, and Y. T. Lee, "Effect of silane coupling agents on the performance of RO membranes," *Journal of Membrane Science*, vol. 300, no. 1-2, pp. 224–231, 2007.

[91] D. H. Shin, N. Kim, and Y. T. Lee, "Modification to the polyamide TFC RO membranes for improvement of chlorine-resistance," *Journal of Membrane Science*, vol. 376, no. 1-2, pp. 302–311, 2011.

[92] Y. Wang and B. Bhushan, "Wear-resistant and antismudge superoleophobic coating on polyethylene terephthalate substrate using SiO_2 nanoparticles," *ACS Applied Materials & Interfaces*, vol. 7, pp. 743–755, 2014.

[93] A. Tuteja, W. Choi, M. Ma, J. M. Mabry, S. A. Mazzella, G. C. Rutledge, G. H. McKinley, and R. E. Cohen, "Designing superoleophobic surfaces," *Science*, vol. 318, pp. 1618–1622, 2007.

[94] L. Zou, I. Vidalis, D. Steele, A. Michelmore, S. P. Low, and J. Q. J. C. Verberk, "Surface hydrophilic modification of RO membranes by plasma polymerization for low organic fouling," *Journal of Membrane Science*, vol. 369, pp. 420–428, 2011.

[95] E. W. Tow and J. H. Lienhard V, "Quantifying osmotic membrane fouling to enable comparisons across diverse processes," *Journal of Membrane Science*, vol. 511, pp. 92–107, 2016.

[96] Y. Huang, H. Li, L. Wang, Y. Qiao, C. Tang, C. Jung, Y. Yon, S. Li, and M. Yu, "Ultrafiltration membranes with structure-optimized graphene-oxide coatings for antifouling oil/water separation," *Advanced Materials Interfaces*, vol. 2, 2015.

123

[97] W. Chen, Y. Su, J. Peng, X. Zhao, Z. Jiang, Y. Dong, Y. Zhang, Y. Liang, and J. Liu, "Efficient wastewater treatment by membranes through constructing tubable antifouling membrane surfaces," *Environmental Science and Technology*, vol. 45, pp. 6546–6552, 2011.

[98] B. Arkles, "Hydrophobicity, hydrophilicity and silane surface modification," tech. rep., Gelest, 2011.

[99] W. Chen, Y. Su, J. Peng, Y. Dong, X. Zhao, and Z. Jiang, "Engineering a robust, versatile amphiphilic membrane surface through forced surface segregation for ultralow flux-decline," *Advanced Functional Materials*, vol. 21, pp. 191–198, 2011.

[100] H. S. Fogler, "Distributions of residence times for chemical reactors," *Elements of Chemical Reaction Engineering*, pp. 867–944, 2006.